Efficient computational methods in Magnetic Resonance Imaging

From optimal dielectric pad design to effective preconditioned imaging techniques

van Gemert, Jeroen

DOI
10.4233/uuid:9d22f175-0fc0-489e-83b7-30ffd9996b3b

Publication date
2019

Document Version
Final published version

Citation (APA)
van Gemert, J. (2019). *Efficient computational methods in Magnetic Resonance Imaging: From optimal dielectric pad design to effective preconditioned imaging techniques*. [Dissertation (TU Delft), Delft University of Technology]. https://doi.org/10.4233/uuid:9d22f175-0fc0-489e-83b7-30ffd9996b3b

Efficient computational methods in Magnetic Resonance Imaging
From optimal dielectric pad design to effective preconditioned imaging techniques

van Gemert, Jeroen

Publication date
2019

Document Version
Publisher's PDF, also known as Version of record

Efficient Computational Methods in Magnetic Resonance Imaging

From optimal dielectric pad design to effective preconditioned imaging techniques

J.H.F. van Gemert

Efficient Computational Methods in Magnetic Resonance Imaging

From Optimal Dielectric Pad Design to Effective Preconditioned Imaging Techniques

EFFICIENT COMPUTATIONAL METHODS IN MAGNETIC RESONANCE IMAGING

FROM OPTIMAL DIELECTRIC PAD DESIGN TO EFFECTIVE PRECONDITIONED IMAGING TECHNIQUES

PROEFSCHRIFT

ter verkrijging van de graad van doctor
aan de Technische Universiteit Delft,
op gezag van de Rector Magnificus prof. dr. ir. T.H.J.J. van der Hagen
voorzitter van het College voor Promoties,
in het openbaar te verdedigen op
donderdag 24 januari 2019 om 15:00 uur

door

JEROEN HENDRIKUS FRANCISCUS VAN GEMERT

Elektrotechnisch Ingenieur, Technische Universiteit Delft, Nederland
geboren te Nijmegen, Nederland

Dit proefschrift is goedgekeurd door de promotoren.

Samenstelling promotiecommissie bestaat uit:

Rector magnificus,	voorzitter
Dr. ir. R.F Remis	Technische Universiteit Delft, *promotor*
Prof. dr. A.G. Webb	Leiden Universitair Medisch Centrum, *promotor*

Onafhankelijke leden:

Prof. dr. A. Yarovoy	Technische Universiteit Delft
Prof. dr. C.M. Collins	New York University School of Medicine
Prof. dr. P. Börnert	Philips Research Hamburg
Dr. ir. C.A.T. van den Berg	Universitair Medisch Centrum Utrecht
Dr. ir. B.P. de Hon	Technische Universiteit Eindhoven
Prof. dr. ir. A.-J. van der Veen	Technische Universiteit Delft, *reservelid*

This work is part of the research programme "DIELECTRIC ENHANCED MRI" with project number 13375, which is (partly) financed by the Netherlands Organisation for Scientific Research (NWO).

Keywords: Maxwell Equations, Dielectric pad, High-permittivity, Reduced-Order Modeling, Magnetic Resonance Imaging, Preconditioning, Reconstruction

Printed by: Ipskamp printing

Front & Back: Hens & Janneke

ISBN 978-94-028-1334-0

An electronic version of this dissertation is available at
http://repository.tudelft.nl.

You can't put a limit on anything.
The more you dream, the farther you get.

- Michael F. Phelps II

CONTENTS

1

General introduction

1

MAGNETIC Resonance Imaging (MRI) is a popular non-invasive imaging technique that is frequently used in many hospitals for medical diagnosis, as it can provide high-resolution three-dimensional images of the anatomy of the body. One of the major challenges in MRI is to produce high-quality images within a short scanning time. High quality images improve the diagnostic value as tissue contrast is enhanced, and the short scan time improves the patients' comfort and it minimizes the risk of patient's movements that degrade the scan. This dissertation will address both challenges separately by focusing on improving the quality using dielectric pads in Part I, and reducing the image reconstruction time to obtain the scan using a preconditioner in Part II.

1.1. DIELECTRIC PAD DESIGN

MR images are acquired by placing the patient in a very strong static magnetic field, referred to as the B_0 field. Hereafter, a circular polarized magnetic field is transmitted (the B_1^+ field) in the form of a pulsed radio-frequency (RF) field that induces precessing magnetization in the human body. Subsequently, the precessing magnetization induces a voltage in the receiver coils that contains information about the tissue. Finally, this information is processed to obtain the final scan [1–3]. Systems with a magnetic field strength of 1.5 and 3 tesla are frequently used in the clinic, but there is great interest in 7 tesla systems as well. This is because the signal to noise ratio (SNR) increases with the B_0 field strength, and subsequently, the improved SNR can be traded for a higher spatial resolution, reduced scanning times, or a combination of both [4, 5].

Despite an improved SNR, there are also a number of image artifacts that are encountered which are not present on low-field systems ($B_0 \leq 1.5$T). The fundamental cause is the frequency of the transmitted RF field, referred to as the Larmor frequency, that increases linearly with the B_0 field strength. The reduced wavelength becomes comparable with the dimensions of the human body and may introduce interference effects. As a consequence, the B_1^+ distribution becomes less homogeneous, resulting in areas with a very low transmit efficiency, i.e. a very low B_1^+ per square root of input power [6]. These regions translate into signal voids in the final scan where the tissue contrast is reduced, and hence these voids decrease image quality, as is illustrated in Figure 1.1a.

The RF homogeneity and efficiency can be improved by active and passive shimming techniques that tailor the magnetic field, such that in a certain region of interest (ROI) the B_1^+ distribution becomes uniform and the transmit efficiency focused. Active shimming uses multiple coils in the form of transmit arrays and requires additional (expensive) hardware, i.e. coils and RF amplifiers. The field can then be tailored by driving each coil element with a specific current and phase such that RF interference patterns can be controlled [7]. Unfortunately, when the number of channels is large, these patterns cannot be predicted and controlled completely, and hence it leads to uncertainty in the power deposition in the human body which compromises safety [8, 9]. These arrays are therefore not used clinically, except when body coils with a limited number of channels (typically two) are used and this occurs only at 3T systems where almost all systems are dual transmit.

Alternatively, passive shimming can be applied in the form of dielectric pads, as depicted in Figures 1.1b and 1.1c [10, 11]. These pads are easy to use and have low pro-

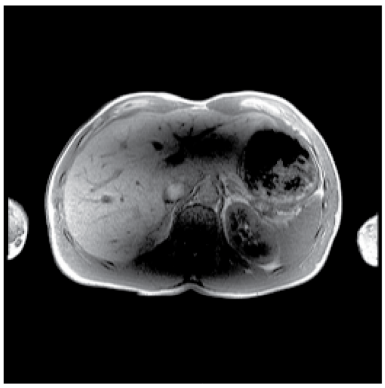

(a)

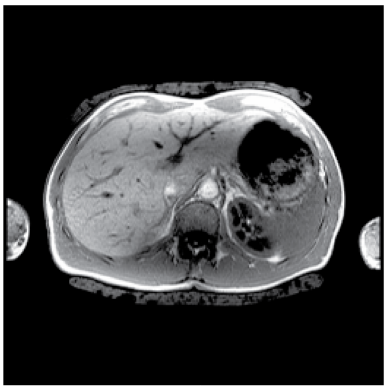

(b)

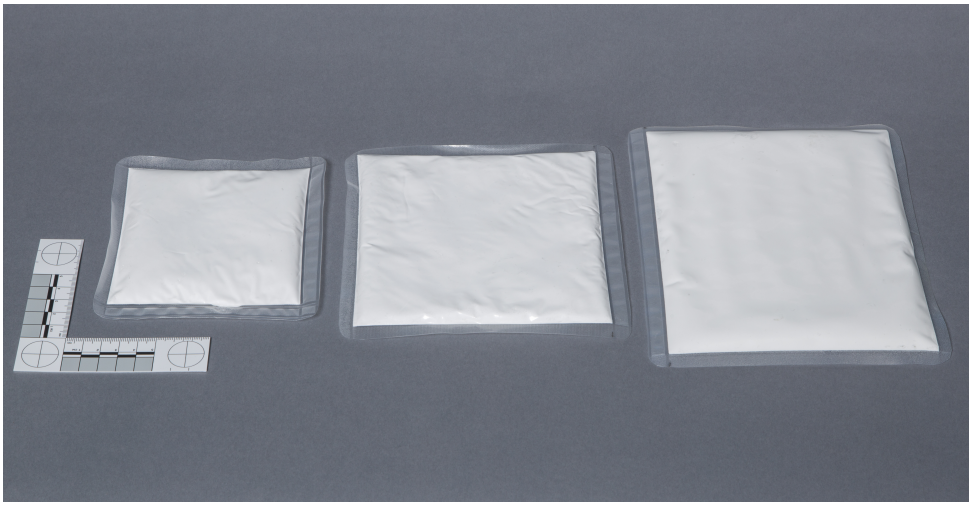

(c)

Figure 1.1: Abdomen scan obtained with a 3T system. Signal voids are encountered at the posterior and anterior of the body due to interference effects and the anatomy cannot be seen clearly anymore (a). The image quality can be restored by placing a dielectric pad on the posterior and the anterior of the body (b). Dielectric pads that are typically used in practice (c).

duction costs [12]. They have a very high relative permittivity (up to 300) and induce a secondary magnetic field that allows for tailoring the B_1^+ field. Typically, the dielectrics are placed in the vicinity of the ROI and as a result they change the RF distribution. Furthermore, because these pads do not increase the power deposition in the human body, they are safe to use [13–15].

Unfortunately, the design of a dielectric pad is not straightforward; it depends on the patient's dimensions and gender, but also on the antenna configuration, the B_0 field strength, and the region of interest to be imaged. For any given scenario, it is generally

not known what the optimal geometry and constitution of the pad are, nor is it always obvious where to place the dielectric. In addition, if it is not well designed, the image quality might even decrease because of a wrongly focused transmit efficiency outside the ROI or an inhomogeneous field distribution in the ROI.

Conventionally, a parametric design study is carried out using commercially available electromagnetic field solvers. The RF response is evaluated for a large number of pad realizations, i.e all pads have a different geometry, location, and constitution [15]. Afterwards, a suitable pad for a specific application can be selected. The simulations are time intensive, as they involve a very large computational domain encompassing a heterogeneous body model and a coil model. As the parameter space is very large and the simulations are time-consuming, it takes hours, days, or even weeks to find a pad for a single application. Furthermore, as the parameter space is too large to be covered completely, the resulting design is not necessarily the optimal one.

In contrast to the conventional trial-and-error method, a more elegant procedure would be to find the dielectric pad's properties and geometries by following an optimization methodology. Therefore, we need a forward model that offers more freedom than the currently available electromagnetic fields solvers, in terms of geometry design and available electromagnetic field data. In addition, the computations should be fast, because they form the building blocks of the design approach. Finally, this approach should allow us to optimize the B_1^+ field for different regions of interest and for different MR configurations to develop a flexible tool.

The aim for this first part of the thesis is to create a user-friendly tool that assists in finding the optimal dielectric pad that improves MR image quality for an arbitrary ROI. This tool should be easy to use and should also be flexible towards different body models and antenna configurations. In addition, the solution is to be computed within seconds on standard PC.

1.2. ACCELERATING RECONSTRUCTIONS

Clinical MR scans generally take about 30 to 60 minutes, which can be a tedious procedure for the patient; hence it is a matter of comfort and convenience for the patient to reduce these long scanning times. Furthermore, this reduction also minimizes the risk of patient movement, which corrupts the scan. During a scan, data is acquired that involves multiple measurements, where for each measurement a series of sample points is obtained. After a certain number of samples, determined by the Nyquist criterion, the signal (in our case related to the anatomy) can be reconstructed completely [16]. Therefore, the acquisition is complete when this criterion has been satisfied. At this stage, a k-space data matrix has been built that can easily be converted to an actual anatomic image by efficient Fourier transformations [17].

The scanning times can be reduced by parallel imaging (PI) techniques that exploit the spatial selectivity of the receiver coils. With PI the number of measurements can be structurally reduced, which implies that the data is undersampled and hence the Nyquist criterion is violated. This results in aliasing artifacts in the image, as is depicted in Figure 1.2a [18]. The true image can still be recovered, however, by using the spatial encoding information from the individual coil elements as is shown in Figure 1.2b. Using this

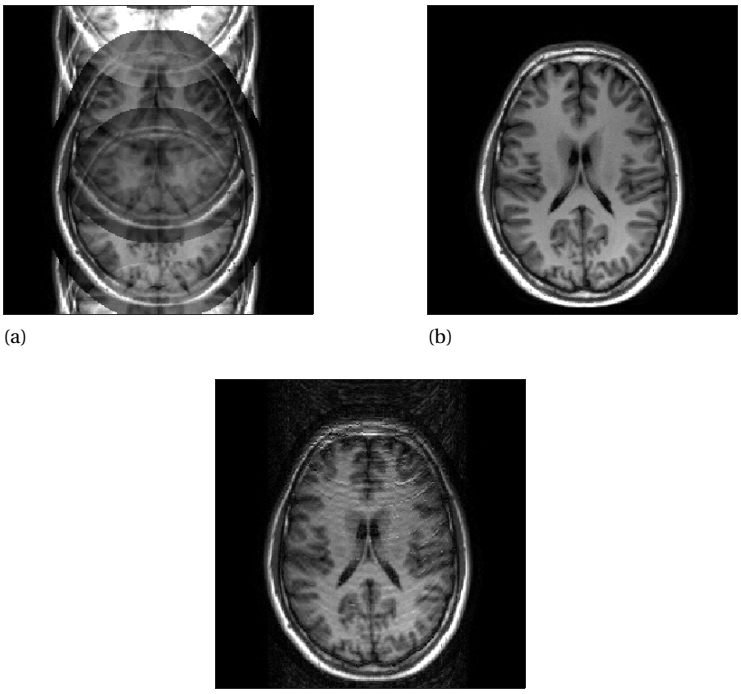

(a) (b)

(c)

Figure 1.2: Reconstruction results for different undersampling methods. The structured undersampling leads to aliasing as shown in (a), in contrast to the fully sampled reference image from (b). For random undersampling the artifacts behave like noise (c).

technique, the undersampling factor can theoretically be made as large as the number of coil channels [19].

Even higher undersampling factors are possible using compressed sensing (CS) techniques. With this method, the k-space is undersampled randomly and the resulting aliasing artifacts behave like noise, as is illustrated in Figure 1.2c. Subsequently, the missing information can be recovered by adding a priori information [20]. This additional information relies on the sparsity of the image in a certain transform domain. It is possible to combine PI and CS, both of which reduce scanning times [21].

Although the actual acquisition time is reduced, the efficient Fourier transformation cannot be used anymore as it introduces aliasing or noise-like artifacts. Therefore, more sophisticated reconstruction algorithms are required. Consequently, the reconstruction time increases considerably. Besides the inability to simply use efficient Fourier transformations, reconstructing the image is not straightforward as it is an ill-posed problem with a non-unique solution. Normally, this issue is resolved by converting it to a well-posed system first, which can be accomplished by regularization in the form of additional constraints that promote sparsity. This makes sense, as from a priori information we know that the image should be sparse in a certain domain. The degree of sparsity can

be set through regularization parameters, which are non-unique and have to be chosen properly to obtain satisfactory image quality and convergence [22, 23].

Many different methods can be used for reconstruction, each having its own strengths and weaknesses [24, 25]. On the whole, it is a trade-off among stability, image quality, and convergence. Stable methods are likely to be slow, and fast methods might experience unstable behavior for certain regularization parameter choices. For adoption in the clinic, unstable methods cannot be used obviously, as they might be unreliable [26]. Although many methods are promising, many of them are either unstable or not very fast.

The aim for the second part of the thesis is therefore to accelerate a frequently used stable PI and CS reconstruction method by designing an easy to construct and easy to implement preconditioner that reduces the reconstruction time considerably.

1.3. THESIS CONTRIBUTIONS AND OUTLINE

The key contributions of this dissertation are summarized as follows:

1. Efficient forward modeling of dielectric pads by setting up a scattering formalism for a pad-independent domain and a pad-dependent domain [Chapter 2].

2. Reduction of the complexity of the forward modeling formalism by using projection-based model order reduction [Chapter 3].

3. Implementation of a pad design tool that assists the user in finding a suitable dielectric pad for an arbitrary ROI [Chapter 4].

4. Development and implementation of a circulant preconditioner that accelerates MR reconstruction [Chapter 5].

The outline of the thesis is presented in Figure 1.3 and is divided into two parts: improving image quality and improving reconstruction times.

The first part will start by introducing the currently used methods for modeling dielectric pads in Chapter 2. In the same chapter, a new model is presented that will form the framework for the remainder of the thesis. The developed method is not yet suitable for effective pad design due to its complexity, and hence this complexity will be reduced using model order reduction techniques in Chapter 3. Furthermore, an optimization approach is proposed that will allow for practical and efficient pad design. Chapter 4 continues with this approach and introduces a design tool that can be used by the MR community.

The second part concentrates on the reconstruction aspects of MRI. In Chapter 5, a currently available stable method called the Split Bregman algorithm is described. This algorithm is accelerated with the proposed design of a preconditioner. Subsequently, its performance is tested on a number of MRI data sets.

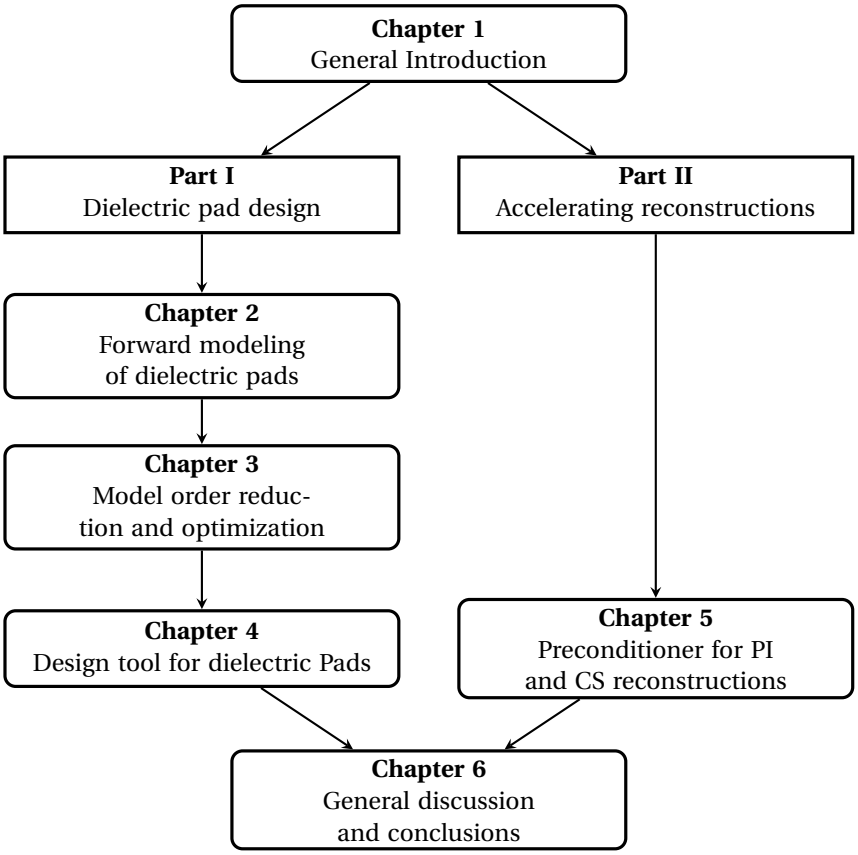

Figure 1.3: Visual outline of the thesis. The dissertation consists of two parts: dielectric pad design and accelerating ronstructions.

REFERENCES

[1] Z.-P. Liang, P. C. Lauterbur, and IEEE Engineering in Medicine and Biology Society., *Principles of magnetic resonance imaging : a signal processing perspective*. SPIE Optical Engineering Press, 2000.

[2] M. A. Bernstein, K. F. King, and X. J. Zhou, *Handbook of MRI pulse sequences*. Academic Press, 2004.

[3] R. W. Brown, Y.-C. N. Cheng, E. M. Haacke, M. R. Thompson, and R. Venkatesan, "Magnetic Resonance Imaging: Physical Principles and Sequence Design," in *Magnetic Resonance Imaging: Physical Principles and Sequence Design*, R. W. Brown, Y.-C. N. Cheng, E. M. Haacke, M. R. Thompson, and R. Venkatesan, Eds. Chichester, UK: John Wiley & Sons Ltd, 2014, ch. Magnetic R, p. 6.

[4] R. Stafford, "High Field MRI - Technology, Applications, Safety, and Limitations," *Medical Physics*, vol. 32, no. 6Part15, pp. 2077–2077, 2005.

[5] C. M. Collins, "Fundamentals of Signal-to-Noise Ratio (SNR)," in

Electromagnetics in Magnetic Resonance Imaging Physical Principles, Related Applications, and Ongoing Developments. IOP Publishing, 2016.

[6] M. Bernstein, J. Huston, and H. Ward, "Imaging artifacts at 3.0 T," *Journal of Magnetic Resonance Imaging*, vol. 24, no. 4, pp. 735–746, 2006.

[7] C. M. Collins, W. Liu, B. J. Swift, and M. B. Smith, "Combination of optimized transmit arrays and some receive array reconstruction methods can yield homogeneous images at very high frequencies," *Magnetic Resonance in Medicine*, vol. 54, no. 6, pp. 1327–1332, 2005.

[8] H. Homann, I. Graesslin, H. Eggers, K. Nehrke, P. Vernickel, U. Katscher, O. Dössel, and P. Börnert, "Local SAR management by RF Shimming: a simulation study with multiple human body models," *Magnetic Resonance Materials in Physics, Biology and Medicine*, vol. 25, no. 3, pp. 193–204, 2012.

[9] Ö. Ipek, A. J. Raaijmakers, J. J. Lagendijk, P. R. Luijten, and C. A. T. van den Berg, "Intersubject local SAR variation for 7T prostate MR imaging with an eight-channel single-side adapted dipole antenna array," *Magnetic Resonance in Medicine*, vol. 71, no. 4, pp. 1559–1567, 2014.

[10] A. Webb, "Dielectric materials in magnetic resonance," *Concepts in Magnetic Resonance Part A*, vol. 38A, no. 4, pp. 148–184, 2011.

[11] P. de Heer, W. M. Brink, B. J. Kooij, and A. G. Webb, "Increasing signal homogeneity and image quality in abdominal imaging at 3 T with very high permittivity materials," *Magnetic Resonance in Medicine*, vol. 68, no. 4, pp. 1317–1324, 2012.

[12] T. O'Reilly, A. Webb, and W. Brink, "Practical improvements in the design of high permittivity pads for dielectric shimming in neuroimaging at 7 T," *Journal of Magnetic Resonance*, vol. 270, pp. 108–114, 2016.

[13] Q. X. Yang, J. Wang, J. Wang, C. M. Collins, C. Wang, and M. B. Smith, "Reducing SAR and enhancing cerebral signal-to-noise ratio with high permittivity padding at 3 T," *Magnetic Resonance in Medicine*, vol. 65, no. 2, pp. 358–362, 2011.

[14] Q. X. Yang, S. Rupprecht, W. Luo, C. Sica, Z. Herse, J. Wang, Z. Cao, J. Vesek, M. T. Lanagan, G. Carluccio, Y.-C. Ryu, and C. M. Collins, "Radiofrequency field enhancement with high dielectric constant (HDC) pads in a receive array coil at 3.0T," *Journal of Magnetic Resonance Imaging*, vol. 38, no. 2, pp. 435–440, 2013.

[15] W. M. Brink and A. G. Webb, "High permittivity pads reduce specific absorption rate, improve B 1 homogeneity, and increase contrast-to-noise ratio for functional cardiac MRI at 3 T," *Magnetic Resonance in Medicine*, vol. 71, no. 4, pp. 1632–1640, 2014.

[16] A. Jerri, "The Shannon sampling theoremIts various extensions and applications: A tutorial review," *Proceedings of the IEEE*, vol. 65, no. 11, pp. 1565–1596, 1977.

[17] M. Bernstein, K. King, and X. Zhou, "Signal Acquisition and k-Space Sampling," in *Handbook of MRI Pulse Sequences*. Elsevier, 2004, pp. 367–442.

[18] M. Lustig, D. Donoho, J. Santos, and J. Pauly, "Compressed Sensing MRI," *IEEE Signal Processing Magazine*, vol. 25, no. 2, pp. 72–82, 2008.

[19] K. P. Pruessmann, M. Weiger, M. B. Scheidegger, and P. Boesiger, "SENSE: sensitivity encoding for fast MRI." *Magnetic resonance in medicine*, vol. 42, no. 5, pp. 952–62, 1999.

[20] D. Donoho, "Compressed sensing," *IEEE Transactions on Information Theory*, vol. 52, no. 4, pp. 1289–1306, 2006.

[21] D. Liang, B. Liu, J. Wang, and L. Ying, "Accelerating SENSE using compressed sensing," *Magnetic Resonance in Medicine*, vol. 62, no. 6, pp. 1574–1584, 2009.

[22] A. Maleki and D. Donoho, "Optimally Tuned Iterative Reconstruction Algorithms for Compressed Sensing," *IEEE Journal of Selected Topics in Signal Processing*, vol. 4, no. 2, pp. 330–341, 2010.

[23] T. Akasaka, K. Fujimoto, T. Yamamoto, T. Okada, Y. Fushumi, A. Yamamoto, T. Tanaka, and K. Togashi, "Optimization of Regularization Parameters in Compressed Sensing of Magnetic Resonance Angiography: Can Statistical Image Metrics Mimic Radiologists' Perception?" *PLOS ONE*, vol. 11, no. 1, p. e0146548, 2016.

[24] L. Feng, T. Benkert, K. T. Block, D. K. Sodickson, R. Otazo, and H. Chandarana, "Compressed sensing for body MRI," *Journal of Magnetic Resonance Imaging*, vol. 45, no. 4, pp. 966–987, 2017.

[25] A. C. Yang, M. Kretzler, S. Sudarski, V. Gulani, and N. Seiberlich, "Sparse Reconstruction Techniques in Magnetic Resonance Imaging: Methods, Applications, and Challenges to Clinical Adoption." *Investigative radiology*, vol. 51, no. 6, pp. 349–64, 2016.

[26] O. N. Jaspan, R. Fleysher, and M. L. Lipton, "Compressed sensing MRI: a review of the clinical literature," *The British Journal of Radiology*, vol. 88, no. 1056, p. 20150487, 2015.

I

PART ONE
DIELECTRIC PAD DESIGN

2

FORWARD MODELING OF DIELECTRIC PADS

In this chapter we present a methodology that aims for fast electromagnetic field computations to model a wide range of dielectric pads in a typical MRI configuration. This is accomplished by using the Sherman-Morrison-Woodbury formula that allows us to model a dielectric pad as a small perturbation of a large static computational background domain, encompassing the human body model and the RF coil. The solution methodology, simulations, and measurements that validate our approach are presented.

This chapter has been published in IEEE Transactions in Medical Imaging.
(Volume: 36, Issue: 2, 2017)

2.1. INTRODUCTION

CLINICAL Magnetic Resonance Imaging (MRI) is a well known noninvasive imaging modality to create detailed images of the human body. The generation of a high quality image can be extremely challenging, however, especially when imaging body parts that are large compared with the wavelength of the Radio-Frequency (RF) field. Constructive and destructive interference effects of the RF field can severely degrade the quality of an MR image reducing its use for interpretation and diagnostics [1, 2]. Interference effects may be particularly predominant for abdominal and cardiac imaging at 3T and neurological, abdominal, and cardiac imaging at 7T [3–6]. The corresponding RF frequencies for 3T and 7T are 128 MHz and 298 MHz, respectively. As an illustration, Figure 2.1a shows the effects of interference in an head scan of a patient obtained with a 7T MRI system. Dark signal drop-outs or signal voids are clearly visible and certain parts of the anatomy can simply not be distinguished. Furthermore, the increased spatial variations in the RF excitation field may also lead to an increase of the local Specific Absorption Rate (SAR).

The RF excitation field is characterized by the forward circular polarized B_1^+ field, defined as

$$B_1^+ = \frac{B_x + jB_y}{2},$$

where j is the imaginary unit, and B_x and B_y are the transverse x- and y-components of the frequency-domain magnetic flux density [7]. As is well known, this field flips the

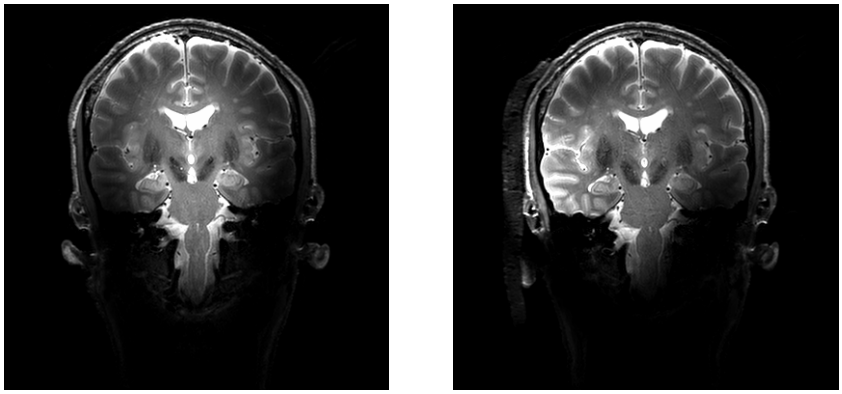

(a) (b)

Figure 2.1: Head scan of a patient in a 7T (298 MHz) MRI system. (a) Signal drop-outs due to wavelength effects in a scan made without any dielectric pad. (b) Scan made with a dielectric pad on the right side of the head. The pad clearly resolves the signal-drop out problem in the right hemisphere of the brain. The pad that is used has a relative permittivity of about 300 with dimensions $18 \times 18 \times 1$ cm^3. The scans have been acquired using a 7T Philips Achieva, where the head coil has been used for transmission and a 32-channel receive coil for reception. For this scan a T2-weighted turbo spin echo sequence has been used with an echo time of 44.8 ms, a pulse repetition time of 6300 ms, and a 120° refocusing pulse. 17 slices were acquired with a field-of-view of $107 \times 240 \times 198$ mm^3. A parallel imaging acceleration factor of 1.5 has been used leading to a total scan time of 164 s.

spins of the protons during an MRI experiment. Spatial inhomogeneities in the B_1^+ magnitude will therefore directly translate into spatial variations in the nutation of spins, and corresponding signal intensity in the final image.

RF shimming is a technique to tailor the RF field interference effects with the use of a transmit array or pTx (active shimming) or by using dielectric materials (passive shimming). Active shimming may require advanced coil designs and additional hardware. Dielectric shimming, on the other hand, makes use of high-permittivity dielectric pads which are relatively cheap to fabricate and can be readily integrated into the existing system architecture without any additional hardware [8].

The materials that are used for these pads typically have relative permittivity values of 80 and higher. In particular, calcium titanate powder mixed with deuterated water can be used if pads with a relative permittivity of about 110 are needed, while barium titanate powder mixed with water with a relative permittivity 300 is used if higher dielectric permittivities are required [9].

In practice, dielectric pads are placed in the vicinity of that part of the body to be imaged and a properly designed pad induces a secondary magnetic field that increases the signal in the regions of interest [10–16]. An example of the impact of a dielectric pad on the resulting MR image is illustrated in Figure 2.1b, where a dielectric pad has been placed on the right side of the head. The signal drop-outs have been eliminated and detailed structures within the right hemisphere of the brain are now clearly visible. An additional advantage of dielectric shimming is that the RF power required for excitation of the spins can be significantly reduced. In [17] for example, it is shown that by including dielectric pads in the MRI measurement setup, the RF power can be reduced by 50% while increasing the Signal-to-Noise ratio. Furthermore, dielectric pads do not influence the B_0 field distribution noticeably [13].

Designing optimal pads is a nontrivial task, however, since the homogeneity of the B_1^+ field is strongly dependent upon its parameters (location, constitution, and geometry). Pads are also patient specific and strongly depend upon the particular body part that is being imaged [18]. Furthermore, a straightforward design approach in which the B_1^+ field is determined for a range of pad parameters (so-called parameter sweeps) is far from practical, since for each realization the B_1^+ field inside the ROI needs to be computed using three-dimensional electromagnetic field solvers resulting in huge computational costs and computations that can even take days to complete.

In this paper, we propose a solution to this problem by computing the B_1^+ field in an efficient manner. This efficiency can be achieved by exploiting the fact that the dimensions of a dielectric pad are small compared with the dimensions of the background model (the body, RF shield, and RF coil). Specifically, since the body, the RF shield, and the RF coil remain fixed during pad design, we show that different pad realizations form low-rank perturbations of the background model. By computing and storing RF field responses in this background model during an offline stage, the RF fields resulting from a wide range of different pads (pads with different locations, sizes, and constitution) can be evaluated very efficiently during an online or design stage using the Sherman-Morrison-Woodbury formula [19]. By following this approach, significant speed-up factors can be achieved. In particular, for a realistic three-dimensional MRI imaging experiment of the human head, we show that speed-up factors ranging from 35 (for “large"

pads) to 2000 (for “small" pads) can be achieved if we compare the computation times of our method with the time that is required to compute the RF field for each realization separately using FDTD. Furthermore, we also show that the Sherman-Morrison-Woodbury formula allows us to efficiently carry out a sensitivity analysis in which variations in the B_1^+ field due to variations in a pad (permittivity, geometry, etc.) can be determined. Finally, we validate our solution methodology by comparing computed B_1^+ fields with measured B_1^+ data *in vivo*.

2.2. MODELING PROCEDURE FOR DIELECTRIC PADS

As an illustrative example, we consider a typical MRI measurement setup in which the objective is to image an ROI in the right hemisphere of the brain at 7T. The configuration of interest is illustrated in Figure 2.2 and consists of an RF shield, an RF coil, and a human body model. To compute the RF field in this configuration, we need to solve Maxwell's equations

$$-\nabla \times \mathbf{H} + \sigma \mathbf{E} + \mathrm{j}\omega\varepsilon\mathbf{E} = -\mathbf{J}^{\mathrm{ext}}$$

and

$$\nabla \times \mathbf{E} + \mathrm{j}\omega\mu\mathbf{H} = \mathbf{0},$$

where $\mathbf{E}$ and $\mathbf{H}$ are the desired electric and magnetic field strengths and $\mathbf{J}^{\mathrm{ext}}$ is the external electric-current density describing the impressed current within an RF coil [20]. The conductivity, permittivity, and permeability within the domain of interest are given by σ, ε, and $\mu = \mu_0$, respectively, where μ_0 is the permeability of vacuum.

Given the complexity of this configuration, we can use a three-dimensional numerical solver to determine the RF fields. In practice, this amounts to solving the spatially discretized Maxwell system

$$(\mathsf{D} + \mathsf{N})\,\mathsf{f} = -\mathsf{q} \tag{2.1}$$

at a particular Larmor frequency ω [21]. In the above equation, D is the spatial differential operator containing the discretized curl operators occurring in Maxwell's equations and

$$\mathsf{N} = \mathsf{C} + \mathrm{j}\omega\mathsf{M}$$

is the medium matrix with C a medium matrix containing the conductivity values within the configuration and M a medium matrix containing the permittivity and permeability values within the computational domain. Furthermore, f is the field vector containing the components of the electric and magnetic field strength and q is a source vector containing the components of the external electric current densities as its elements. Finally, the order N of the discretized Maxwell system is equal to the total number of primary and dual grid edges in the computational domain [22]. We note that this order is typically very large especially for realistic three-dimensional configurations as considered here, usually it is in the order of 10^{6-7}. Directly solving the discretized Maxwell system for different medium matrices as is required when pads of different sizes and constitution are included can therefore be prohibitively expensive.

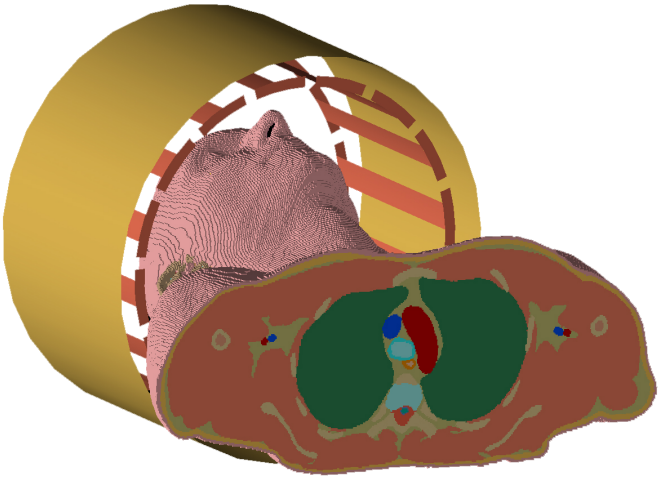

Figure 2.2: The three-dimensional simulation setup used for 7T MRI imaging of the brain. The configuration consists of an RF shield, an RF coil, and a human body model.

Dielectric pads are small compared to the dimensions of the computational domain, however, and inclusion of a dielectric pad therefore forms a small rank perturbation of the discretized Maxwell system of Eq. (2.1), since the position of the human body and the RF coil remain fixed. We take this observation into account by introducing the pad matrix

$$\mathsf{N}_{\text{pad}} = \sum_{k \in \mathscr{P}} \left[\sigma_{\text{pad}}(\mathbf{r}_k) + \mathrm{j}\omega\varepsilon_{\text{pad}}(\mathbf{r}_k) \right] \mathsf{e}_k \mathsf{e}_k^T,$$

where $\mathscr{P} = \{k_1, k_2, ..., k_P\}$ is the index set of the pad, e_k is the kth canonical basis vector, $\mathbf{r}_k$ is the position vector of the kth grid edge that is occupied by the pad, and $\sigma_{\text{pad}}(\mathbf{r}_k)$ and $\varepsilon_{\text{pad}}(\mathbf{r}_k)$ are the conductivity and permittivity of the pad on the kth grid edge. The discretized Maxwell system for a configuration including a pad then becomes

$$\left(\mathsf{D} + \mathsf{N} + \mathsf{N}_{\text{pad}}\right) \mathsf{f} = -\mathsf{q}.$$

We exploit the fact that the number of grid edges occupied by the pad P is much smaller than N to efficiently compute only the small rank perturbation of the system due to a dielectric pad by using the Sherman-Morrison-Woodbury formula (see [19], for example). To make this explicit, let us introduce the N-by-P pad support matrix S as

$$\mathsf{S} = \left[\mathsf{e}_{k_1}, \mathsf{e}_{k_2}, ..., \mathsf{e}_{k_p} \right]$$

and the reduced P-by-P pad matrix $\tilde{\mathsf{N}}_{\text{pad}} = \text{diag}(\mathsf{n})$ with its argument being a P-by-1 vector given by

$$\mathsf{n} = \left[\sigma_{\text{pad}}(\mathbf{r}_{k_1}) + \mathrm{j}\omega\varepsilon_{\text{pad}}(\mathbf{r}_{k_1}), ..., \sigma_{\text{pad}}(\mathbf{r}_{k_P}) + \mathrm{j}\omega\varepsilon_{\text{pad}}(\mathbf{r}_{k_P}) \right]^T.$$

Here, the operation diag(n) constructs a square diagonal matrix with the elements of the vector n on its main diagonal. Using these definitions, we can also write $\mathsf{N}_{\text{pad}} = \mathsf{S}\tilde{\mathsf{N}}_{\text{pad}}\mathsf{S}^T$ and the discretized Maxwell system with pad included becomes

$$\left(\mathsf{A} + \mathsf{S}\tilde{\mathsf{N}}_{\text{pad}}\mathsf{S}^T\right)\mathsf{f} = -\mathsf{q}, \tag{2.2}$$

where we have introduced the discretized Maxwell operator for a configuration without any pad as $\mathsf{A} = \mathsf{D} + \mathsf{N}$. Clearly, computing $\mathsf{f}^{\text{no pad}} = -\mathsf{A}^{-1}\mathsf{q}$ amounts to determining the RF field in the case that no pad is present.

To find the RF field when a pad is present, we now formally solve Eq. (2.2) and apply the Sherman-Morrison-Woodbury formula. We obtain

$$\begin{aligned}\mathsf{f} &= -\left(\mathsf{A} + \mathsf{S}\tilde{\mathsf{N}}_{\text{pad}}\mathsf{S}^T\right)^{-1}\mathsf{q} \\ &= \mathsf{f}^{\text{no pad}} + \mathsf{Z}(\mathsf{I}_P - \tilde{\mathsf{N}}_{\text{pad}}\mathsf{S}^T\mathsf{Z})^{-1}\tilde{\mathsf{N}}_{\text{pad}}\mathsf{S}^T\mathsf{f}^{\text{no pad}},\end{aligned} \tag{2.3}$$

where I_P is the identity matrix of order P and where we have introduced the so-called library matrix $\mathsf{Z} = -\mathsf{A}^{-1}\mathsf{S}$, which is a tall N-by-P matrix. Every column of S represents a unitary current forced on one edge of the pad domain, note that the birdcage does not act as a primary source in this case. The resulting fields in the domain of interest and the pad domain are stored in one column of matrix Z. We refer to this matrix as a library matrix, since it can be computed offline before any actual pad inclusion. The formula we presented here does not involve any approximations. However, the inverse in the formula should be non-singular, which is normally satisfied.

Equation (2.3) provides us with an explicit expression for all electric and magnetic field components on the entire domain of computation. To obtain the B_1^+ field values inside the head, we need to extract the relevant components from the field vector f. Suppose, for example, that the jth entry of the field vector f is equal to the x-component of the magnetic field strength at a particular location in a region of interest inside the head, while the kth entry of the field vector contains the y-component of the magnetic field strength at the same location. The B_1^+ field at this particular location of interest is then given by $B_1^+ = \mathsf{r}^T\mathsf{f}$, where r is the recorder vector for the location of interest given by

$$\mathsf{r} = \frac{\mu_0}{2}(\mathsf{e}_j + \mathsf{j}\mathsf{e}_k).$$

The B_1^+ field inside an entire region of interest can be obtained from the field vector by introducing a recorder vector for each location. Storing these recorder vectors as columns in the N-by-N_{r} recorder matrix R, where N_{r} is the total number of locations inside the region of interest, the B_1^+ field inside this region is obtained as

$$\mathsf{b}_1^+ = \mathsf{R}^T\mathsf{f}.$$

Substituting Eq. (2.3) into the above equation, we arrive at

$$\mathsf{b}_1^+ = \mathsf{b}_1^{+;\text{no pad}} + \mathsf{R}^T\mathsf{Z}(\mathsf{I}_P - \tilde{\mathsf{N}}_{\text{pad}}\mathsf{S}^T\mathsf{Z})^{-1}\tilde{\mathsf{N}}_{\text{pad}}\mathsf{S}^T\mathsf{f}^{\text{no pad}}, \tag{2.4}$$

where $\mathsf{b}_1^{+;\text{no pad}} = \mathsf{R}^T\mathsf{f}^{\text{no pad}}$ is the B_1^+ field inside the region of interest in the case that there is no pad present.

The main advantage of using the above formulation is that as soon as the library matrix Z is available, the B_1^+ field response to a wide variety of dielectric pads can be computed very efficiently, since for each particular pad only the second term in Eq. (2.4) needs to be evaluated. In fact, Eq. (2.4) suggests that we can split the design procedure for dielectric pads into an offline stage and online design stage. During the offline stage, we first identify a pad design domain that surrounds the particular part of the body to be imaged. This domain consists of all grid edges that can be occupied by a pad and we subsequently construct the library matrix Z for the selected pad design domain. As soon as the library matrix is available, we start the online design stage by computing the B_1^+ field using Eq. (2.4). We note that when the dimensions of the evaluated pad are smaller than that of the pad design space, we can further reduce the order of our system by including only the relevant columns of the support matrix S and library matrix Z. Therefore, the evaluation of the second term amounts to solving a system of at most order P and, as pointed out above, this order is much smaller than the order N of the total system. Consequently, we can very efficiently evaluate different RF fields due to a wide variety of pads with different shapes and constitution. Moreover, since $P \ll N$ direct solvers can often even be used and this has the additional advantage that the computation time required to determine the scattered fields due to the presence of a pad becomes independent of the contrast of a pad.

To summarize, we propose the following RF field modeling procedure to compute electromagnetic fields in dielectric shimming:

1. **Offline stage**

    - For a given part of the human body in which the electromagnetic field is required, first compute the $\mathsf{b}_1^{+;\text{no pad}}$ field and the field $\mathsf{f}^{\text{no pad}}$, which are the fields in absence of any dielectric pad.
    - Identify a pad design domain where a pad can be positioned.
    - Construct the library matrix Z by filling its columns one by one, that is, compute $\mathsf{Z}(:,k) = -\mathsf{A}^{-1}\mathsf{e}_{k_p}$ for all $k_p \in \mathscr{P}$. Here e_{k_p} is one of the columns of our support matrix S. In our case we solve this system using a commercial FDTD solver since this is known to solve electromagnetic problems efficiently, although other methods are possible as well. If $\mathsf{Z}(:,k)$ is computed using an iterative solver, then $\mathsf{Z}(:,k-1)$ may serve as an initial guess.

2. **Online stage**

    - Compute the B_1^+ field for a pad of any desired shape or constitution using Eq. (2.4). For a pad covering P grid edges, only a small P-by-P system needs to be solved. A particular pad should be located within the preallocated pad domain, of course, since this domain determines the columns of matrix S.

In Section 2.4 we illustrate the performance of this solution procedure and compare the computed B_1^+ fields with measurements as well.

2.3. SENSITIVITY ANALYSIS

The RF field changes at a particular location within the human body when a pad is included in the background configuration, or when the shape, location, or constitution of the dielectric pad changes. To investigate these effects, we carry out a sensitivity analysis using the Sherman-Morison-Woodbury expression for the RF field as given by Eq. (2.3). This expression allows us to explicitly compute the Jacobian of the field with respect to changes in the shape, location, and contrast of the pad. In particular, writing $\mathsf{b}_1^+ = \mathsf{b}_1^+(\mathsf{n})$ for the field as given by Eq. (2.4), we have

$$\mathsf{b}_1^+(\mathsf{n}+\delta\mathsf{n}) \approx \mathsf{b}_1^+(\mathsf{n}) + \mathsf{J}(\mathsf{n})\,\delta\mathsf{n}$$

for a sufficiently small contrast perturbation vector $\delta\mathsf{n}$, where J is the Jacobian given by

$$\mathsf{J}(\mathsf{n}) = \mathsf{R}^T\mathsf{Z}(\mathsf{I}_P - \tilde{\mathsf{N}}_{\text{pad}}\mathsf{S}^T\mathsf{Z})^{-1}\,\text{diag}(w_1, w_2, ..., w_m) \tag{2.5}$$

with $w_m = \mathsf{e}_{k_m}^T\,\mathsf{f}(\mathsf{n})$ for $m = 1, 2, ..., P$. The perturbation vector $\delta\mathsf{n}$ allows us to change the properties of the pad. We observe that with the library matrix Z at our disposal, again only a small system of order P has to be solved to determine the first-order variations in the field due to changes in contrast function values of the pad. This allows us to efficiently carry out a pad sensitivity analysis.

Moreover, the availability of the Jacobian also enables us to carry out full nonlinear Gauss-Newton-type minimization schemes for optimal dielectric pad design, see e.g. [23]. Although this will be something for future work, a first step towards pad design could be to describe a desired B_1^+ field and define a cost function as

$$C(\mathbf{n}) = \|\mathsf{b}_1^+(\mathsf{n}) - \mathsf{b}_1^{+;\text{desired}}\|_2^2.$$

This cost function can be minimized for a particular pad (n) in an iterative fashion by linearizing $\mathsf{b}_1^+(\mathsf{n})$ and solving the normal equations to find an update direction. Specifically, having a current reconstruction n_i available, a new reconstruction is computed via the update direction $\mathsf{n}_{i+1} = \mathsf{n}_i + \delta\mathsf{n}$, where

$$\delta\mathsf{n} = \left[\mathsf{J}^H(\mathsf{n}_i)\mathsf{J}(\mathsf{n}_i)\right]^{-1}\mathsf{J}^H(\mathsf{n}_i)\epsilon(\mathsf{n}_i).$$

Here $\epsilon(\mathsf{n}_i) = \mathsf{b}_1^+(\mathsf{n}_i) - \mathsf{b}_1^{+;\text{desired}}$ denotes the error of the desired field with respect to the field obtained with a pad for iteration i.

2.4. SIMULATIONS AND MEASUREMENTS

We illustrate the performance of our dielectric shimming procedure by evaluating the design of dielectric pads for 7T MR imaging of a local ROI in the right hemisphere of the brain. The simulated configuration is depicted in Figure 2.2 and consists of the head and shoulders of the male body model "Duke" from the Virtual Family dataset [24], a 7T 16-rung high-pass birdcage coil with a radius of 15 cm operating in quadrature mode at 298 MHz, and an RF shield with a radius of 18 cm. The configuration has a 5 mm^3 resolution. The coronal and transverse slices used to depict the B_1^+ fields inside the head are shown in Figure 2.3.

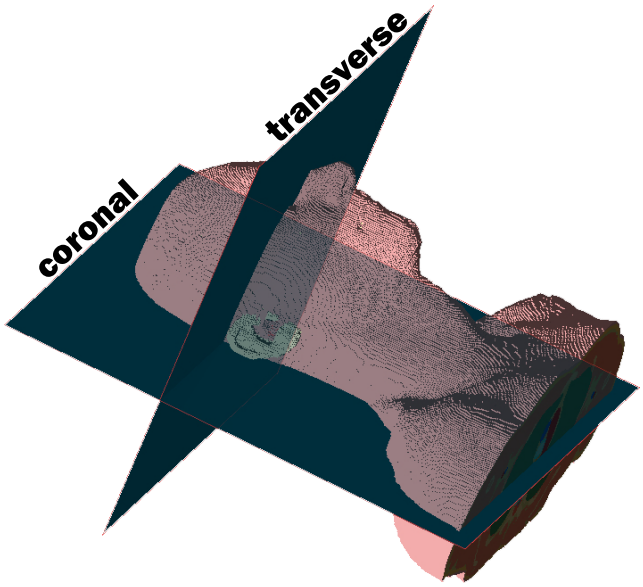

Figure 2.3: Coronal and transverse slices through the head used to depict the B_1^+ fields.

In the offline stage of our solution procedure, we first compute the fields $\mathsf{b}_1^{+;\text{no pad}}$ and $\mathsf{f}^{\text{no pad}}$. Figure 2.7 (left column) shows the magnitude of this B_1^+ field within the transverse and coronal slices. Interference effects of the 298 MHz RF field at 7T are responsible for the signal drops on the left and right-hand side of the head. The fields are computed by Remcom XFdtd software (v.7.5.0.3, State College, PA, USA). The computational domain in XFdtd consists of nearly 10^6 grid edges and we have set the stopping criteria of the simulations to -40 dB convergence.

Having the background field available, we now have to identify a pad design domain. Since the objective of the MRI experiment is to image an ROI in the right hemisphere of the brain, we define a pad design domain of $18 \times 18 \times 1$ cm^3 on the right side of the head as indicated by the outer square area in Figure 2.4. The thickness of the design domain is taken to be 1 cm to comply with typical thicknesses of pads used to image parts of the human head. Subsequently, the library matrix Z is constructed using Remcom's XFdtd software. To investigate in which areas the B_1^+ field can be affected by a dielectric pad, we now first carry out a sensitivity analysis using the Jacobian of Eq. (2.5). Specifically, we select a particular grid edge in the pad domain (the pth grid edge, say) and determine the normalized sensitivity of the B_1^+ field inside the head by computing the pth column of the Jacobian and normalizing this column with respect to the entry with the largest absolute value. Figure 2.5 shows the magnitude of the sensitivity of the B_1^+ field with respect to changes in the indicated pad grid edge. This result clearly shows that the B_1^+ field can indeed be affected by placing a dielectric pad on the right-hand side of the head. Sensitivity analyses for other pad grid edges can be carried out in a similar manner.

To illustrate the efficiency of the proposed method, and to illustrate that the degree of efficiency depends on the dimensions of the pads, we compute the B_1^+ fields for a series

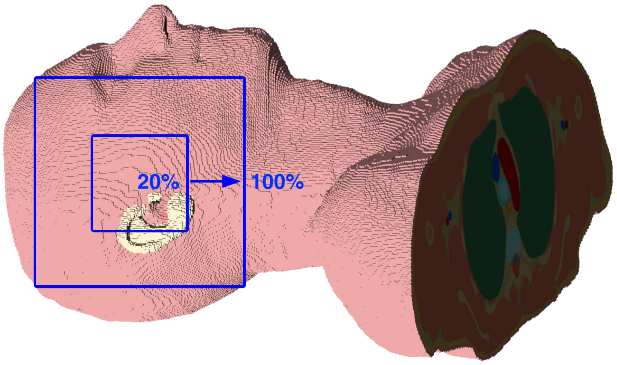

Figure 2.4: Pad design domain of $18 \times 18 \times 1$ cm^3 located on the right-hand side of the human head. The domain has a thickness of 1 cm. Pad sizes range from 100% (the pad design domain is completely filled) to 20%. All pads are centered around the midpoint of the pad design domain.

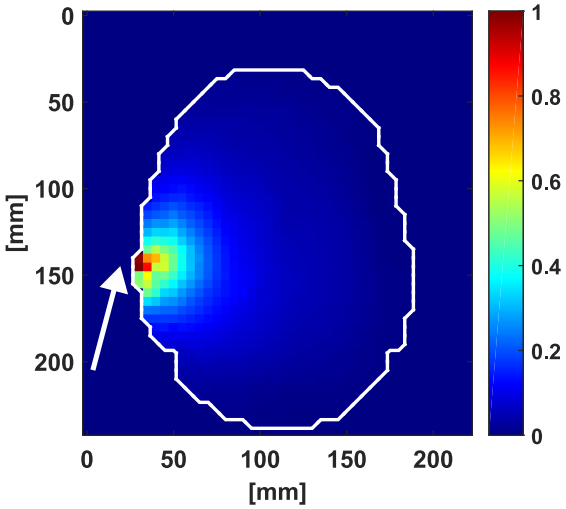

Figure 2.5: Normalized sensitivity of the B_1^+ field inside the head with respect to changes in a single grid edge located within the pad domain. This grid edge has been indicated with the arrow.

of pads with different sizes. Specifically, we start with a pad that completely occupies the pad design domain and subsequently reduce its size down to 20% of the volume of the original full-sized pad (see Figure 2.4). For simplicity, we consider homogeneous pads only and fix the dielectric properties of the pad ($\varepsilon_{\text{pad}} = 285\varepsilon_0$ F/m, $\sigma_{\text{pad}} = 0.25$ S/m), but we stress that our formulation allows for inhomogeneous pads with varying medium parameters as well (see Section 2.2).

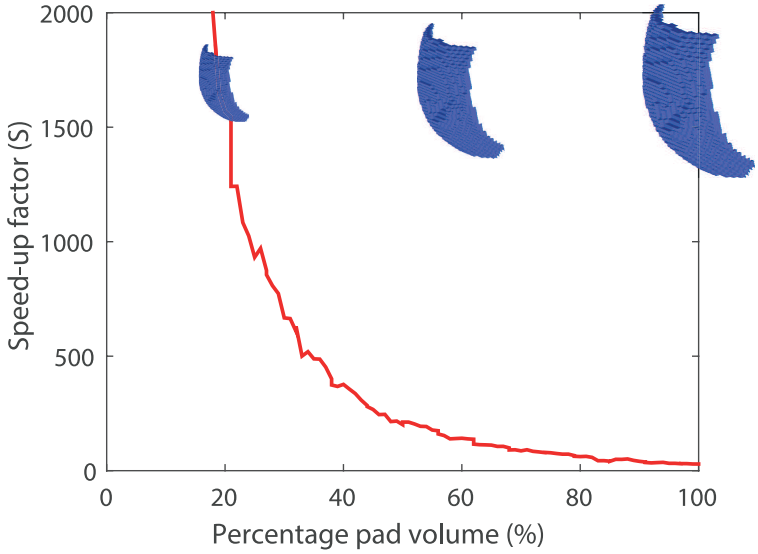

Figure 2.6: Speed-up factors for concentric square pads with increasing volumes. The pad volume ranges from 20% of the volume of the preassigned pad domain to 100% of the pad domain (pad domain is completely filled).

To indicate what speed up factors can be achieved with our approach, we compare the CPU time t_1 required by Remcom's XFdtd package to compute the B_1^+ field for a particular pad with the CPU time t_2 needed by the online stage of the design procedure as proposed in this paper. Specifically, for a particular pad the speed up factor is defined as $S = t_1/t_2$. All CPU times are measured on a Windows 64-bit machine with an Intel Xeon CPU X5660 @ 2.80 GHz (dual core) with 48 GB internal memory and two NVIDIA Tesla K40c GPU's.

Figure 2.6 shows the speed up factor for a series of concentric dielectric pads with increasing volumes. For the smallest pad with a volume of 20% of the volume of the total preassigned pad domain, the proposed method is approximately 2000 times faster than XFdtd. The speed up factor clearly decreases as the volume of the pad increases and we end up with a speed up factor of 35 for a pad that completely fills the pad domain (CPU times $t_1 = 300$ s and $t_2 = 8.5$ s). To illustrate the effectiveness in similar configurations, the work presented in [25] where two pads with dimensions $10 \times 14 \times 1$ cm^3 are used would have been computed in 6 s ($S = 50$). And the work presented in [26] where three pads with dimensions $7 \times 7 \times 0.5$ cm^3 are used would have been computed in 0.3 s ($S = 1000$). These large speed up factors can be achieved since we computed the library matrix Z beforehand during the offline stage of our solution procedure. For the realistic 3D background model considered in this experiment (see Fig 2.2), we constructed almost 6000 library vectors stored as columns in matrix Z, where each vector results from one column of our support matrix S (see Section 2.2). This process takes approximately 26 hours on the above mentioned machine when computed using the GPU, but as soon as it is available for a fixed background consisting of the human body, RF coil, and RF shield,

it allows for very efficient pad design and B_1^+ fields corresponding to a wide variety of pads of different sizes and constitution can be determined in a very efficient manner.

Finally, we validate our design procedure by comparing the simulated B_1^+ field with direct XFdtd computations and measurements. The second and third column of Figure 2.7 show the magnitude of the B_1^+ field in the coronal and transverse plane as computed by XFdtd and the proposed solution procedure for a pad that completely occupies the pad design domain ($\varepsilon_{\text{pad}} = 285\varepsilon_0$ F/m, $\sigma_{\text{pad}} = 0.25$ S/m). The exact location of the pad has been indicated in Figure 2.7. The right column of Figure 2.7 shows the relative error map in percent. The field computed directly by XFdtd and the field computed using Eq. (2.4) essentially coincide, since Eq. (2.4) is an identity. However, we do see some small errors in the error map, most of them are located in the low field areas in the vicinity of the dielectric pad. This is for some part expected, since the relative error is depicted. Remaining differences between the methods may arise from the finite convergence time used to construct the library matrix Z, which then causes small errors to accumulate globally. Nevertheless, the differences remain very small (at most 1%). Furthermore, Figure 2.9 shows the measured B_1^+ map obtained *in vivo* for the dielectric pad used in the simulations. The map was obtained using a DREAM B_1^+ mapping sequence with a 2.5 mm^2 resolution [27], a 5 mm slice thickness and preparation and imaging flip angles of 50° and 10°, respectively. The measured B_1^+ maps are clearly in good agreement with the simulated B_1^+ maps and the destructive interference effect at the right-hand side of the head has been reduced significantly due to the application of the dielectric pad. Discrepancies between the measured data and simulated data arise from modeling errors that are common in both simulation methods (different body model, position of the body model, pad position, etc.) and are not related to the proposed solution method.

To show that our method holds for other constitutions of the pad as well, we take some unusual high values for the conductivity and permittivity, i.e. $\sigma_{\text{pad}} = 2.5$ S/m and $\varepsilon_{\text{pad}} = 1000\varepsilon_0$ F/m. In Figure 2.8 the magnitude of the electric fields are shown for a transverse slice of the head when computed with FDTD (second column) and with our proposed method (third column). The relative error map is shown in the right column where we see that the introduced errors are still very small.

2.5. CONCLUSION AND DISCUSSION

In this paper, we have presented an efficient forward modeling methodology for the efficient design of dielectric pads in MRI. During the design procedure, the background consisting of the RF shield, coil, and human body do not change, while the dimensions of the dielectric pads are small compared to the dimensions of the background model. Consequently, the pads form a small rank perturbation of the computational domain and the resulting RF fields can be efficiently determined by exploiting the well-known Sherman-Morrison-Woodbury formula. We stress that this formula is an identity and hence does not involve any approximations, provided that the inverse that we need to compute does exist. Our numerical experiments show that by following this approach, significant speed-up factors can be achieved compared with straightforwardly computing the RF field for each pad realization. Obviously, when the pad becomes excessively large the method might be less efficient since this would not yield a small rank perturbation with respect to the computational domain. However, such configurations are not

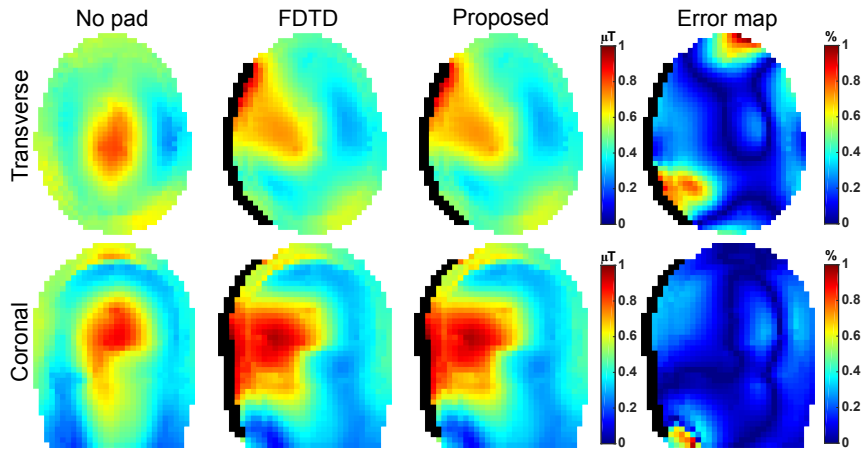

Figure 2.7: Magnitude and error map of the B_1^+ field in the coronal and transverse slices through the head. Left column: magnitude of the B_1^+ field without any pad, second column: B_1^+ field as computed by Remcom's XFdtd, third column: magnitude of the B_1^+ field as computed by the proposed solution procedure, right column: relative error map of the B_1^+ field in percent. The dielectric pad is indicated in black and has a permittivity of $285\varepsilon_0$ F/m and a conductivity of 0.25 S/m.

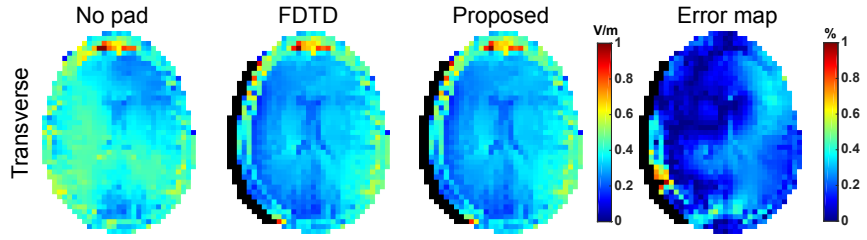

Figure 2.8: Magnitude and error map of the electric field in the transverse slice through the head. Left column: magnitude of electric field without any pad, second column: magnitude of the electric field as computed by Remcom's XFdtd in V/m, third column: magnitude of the electric field as computed by the proposed solution procedure in V/m, right column: relative error map of the electric field in percent. The dielectric pad is indicated in black and has a permittivity of $1000\varepsilon_0$ F/m and a conductivity of 2.5 S/m.

realistic since dielectric pads are typically small compared to the human subject. Furthermore, we have validated our methodology by comparing predicted B_1^+ fields with full FDTD solutions and measurements carried out on a male human head. The simulated and measured field responses are in good agreement with each other, illustrating that the proposed solution methodology allows for effective pad analysis in dielectric shimming.

In our present implementation, the background model is subject dependent and different libraries have to be used for different subjects (male, female, etc.). In practice, a quick survey scan of the patient will allow us to select a library that fits best with the posture of the patient. In future work, we will investigate to what extent it is possible to

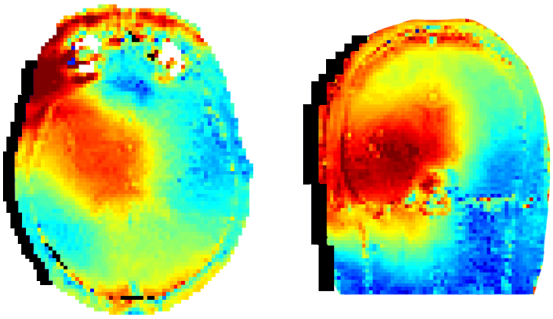

Figure 2.9: Magnitude of the measured B_1^+ field (*in vivo*) for a dielectric pad (indicated in black) with a permittivity of $285\varepsilon_0$ F/m and a conductivity of 0.25 S/m. Left column depicts the field for the transverse slice and the right column depicts the field for the coronal slice.

construct patient independent body models (or models that are suitable for a particular class of patients) by applying homogenization or more general model-order reduction techniques to the body models [28]. These techniques can reduce the number of libraries, thereby reducing the computational costs of the offline stage of our solution procedure. These computational costs can also be reduced by relaxing the convergence settings of the FDTD solver used for calculating these libraries, which in this work has been chosen conservatively.

Additionally, we are planning to combine our proposed solution methodology with fully nonlinear optimization schemes (Newton- or Gauss-Newton schemes, for example) to find optimal dielectric pads that minimize a differentiable objective function that measures the discrepancy between a desired and a modeled B_1^+ field as described briefly in Section 2.3.

Finally, our method not only determines the magnetic field strength but also the electric field strength, the SAR within the body can be efficiently computed for a complete range of different pad designs of interest as well. More generally, the method can be fruitfully applied in any MRI setting in which electrically small materials or devices are included. The possible appearance of hotspots around implants such as deep brain stimulators, for example, could effectively be studied using our approach. With our proposed solution methodology, RF fields and derived quantities such as the SAR can be computed very efficiently for a wide range of devices or pads so long as these devices are electrically small and form a low rank perturbation of a fixed and large-scale background model.

REFERENCES

[1] M. Bernstein, J. Huston, and H. Ward, "Imaging artifacts at 3.0 T," *Journal of Magnetic Resonance Imaging*, vol. 24, no. 4, pp. 735–746, 2006.

[2] K. Chang and I. Kamel, "Abdominal imaging at 3T: Challenges and solutions," *Applied Radiology*, vol. 39, no. 10, p. 22, 2010.

[3] O. Dietrich, M. Reiser, and S. Schoenberg, "Artifacts in 3-T MRI: physical background and reduction strategies." *European Journal of Radiology*, vol. 65, no. 1, pp. 29–35, 2008.

[4] K. Sung and K. Nayak, "Measurement and characterization of RF nonuniformity over the heart at 3T using body coil transmission," *Journal of Magnetic Resonance Imaging*, vol. 27, no. 3, pp. 643–648, 2008.

[5] J. T. Vaughan, M. Garwood, C. M. Collins, W. Liu, L. DelaBarre, G. Adriany, P. Andersen, H. Merkle, R. Goebel, M. B. Smith, and K. Ugurbil, "7T vs. 4T: RF power, homogeneity, and signal-to-noise comparison in head images." *Magnetic Resonance in Medicine*, vol. 46, no. 1, pp. 24–30, 2001.

[6] P.-F. Van de Moortele, C. Akgun, G. Adriany, S. Moeller, J. Ritter, C. M. Collins, M. B. Smith, J. T. Vaughan, and K. Uurbil, "B1 destructive interferences and spatial phase patterns at 7 T with a head transceiver array coil," *Magnetic Resonance in Medicine*, vol. 54, no. 6, pp. 1503–1518, 2005.

[7] D. I. Hoult, "The principle of reciprocity in signal strength calculations. A mathematical guide," *Concepts in Magnetic Resonance*, vol. 12, no. 4, pp. 173–187, 2000.

[8] S. A. Winkler and B. K. Rutt, "Practical methods for improving B1+ homogeneity in 3 tesla breast imaging," *Journal of Magnetic Resonance Imaging*, vol. 41, no. 4, pp. 992–999, 2015.

[9] W. M. Teeuwisse, W. M. Brink, K. N. Haines, and A. G. Webb, "Simulations of high permittivity materials for 7 T neuroimaging and evaluation of a new barium titanate-based dielectric," *Magnetic Resonance in Medicine*, vol. 67, no. 4, pp. 912–918, 2012.

[10] W. M. Brink and A. G. Webb, "A forward model analysis of dielectric shimming in magnetic resonance imaging," in *2013 International Conference on Electromagnetics in Advanced Applications (ICEAA)*. IEEE, 2013, pp. 528–531.

[11] W. M. Brink, A. M. van der Jagt, M. J. Versluis, B. M. Verbist, and A. G. Webb, "High Permittivity Dielectric Pads Improve High Spatial Resolution Magnetic Resonance Imaging of the Inner Ear at 7 T," *Investigative Radiology*, vol. 49, no. 5, pp. 271–277, 2014.

[12] W. M. Brink, R. F. Remis, and A. G. Webb, "A theoretical approach based on electromagnetic scattering for analysing dielectric shimming in high-field MRI," *Magnetic Resonance in Medicine*, vol. 75, no. 5, pp. 2185–2194, 2016.

[13] W. M. Teeuwisse, W. M. Brink, and A. G. Webb, "Quantitative assessment of the effects of high-permittivity pads in 7 Tesla MRI of the brain," *Magnetic Resonance in Medicine*, vol. 67, no. 5, pp. 1285–1293, 2012.

[14] P. de Heer, W. M. Brink, B. J. Kooij, and A. G. Webb, "Increasing signal homogeneity and image quality in abdominal imaging at 3 T with very high permittivity materials," *Magnetic Resonance in Medicine*, vol. 68, no. 4, pp. 1317–1324, 2012.

[15] P. de Heer, M. B. Bizino, M. J. Versluis, A. G. Webb, and H. J. Lamb, "Improved Cardiac Proton Magnetic Resonance Spectroscopy at 3 T Using High Permittivity Pads," *Investigative Radiology*, vol. 51, no. 2, pp. 134–138, 2016.

[16] Q. X. Yang, W. Mao, J. Wang, M. B. Smith, H. Lei, X. Zhang, K. Ugurbil, and W. Chen, "Manipulation of image intensity distribution at 7.0 T: Passive RF shimming and focusing with dielectric materials," *Journal of Magnetic Resonance Imaging*, vol. 24, no. 1, pp. 197–202, 2006.

[17] Q. X. Yang, J. Wang, J. Wang, C. M. Collins, C. Wang, and M. B. Smith, "Reducing SAR and enhancing cerebral signal-to-noise ratio with high permittivity padding at 3 T," *Magnetic Resonance in Medicine*, vol. 65, no. 2, pp. 358–362, 2011.

[18] W. M. Brink and A. G. Webb, "High permittivity pads reduce specific absorption rate, improve B 1 homogeneity, and increase contrast-to-noise ratio for functional cardiac MRI at 3 T," *Magnetic Resonance in Medicine*, vol. 71, no. 4, pp. 1632–1640, 2014.

[19] C. Golub, G.H.; van Loan, "Matrix Computations," in *Matrix Computations*. Baltimore: Johns Hopkins University Press, 2012, p. 65.

[20] A. De Hoop, *Handbook of radiation and scattering of waves: Acoustic waves in fluids, elastic waves in solids, electromagnetic waves: with corrections*. London: Academic Press, 1995.

[21] U. S. Inan and R. A. Marshall, *Numerical electromagnetics : the FDTD method*. Cambridge University Press, 2011.

[22] A. Taflove and K. R. Umashankar, "The Finite-Difference Time-Domain Method for Numerical Modeling of Electromagnetic Wave Interactions," *Electromagnetics*, vol. 10, no. 1-2, pp. 105–126, 1990.

[23] S. P. Boyd and L. Vandenberghe, "Convex optimization," in *Convex optimization*. Cambridge: Cambridge University Press, 2004, ch. 9, p. 716.

[24] A. Christ, W. Kainz, E. G. Hahn, K. Honegger, M. Zefferer, E. Neufeld, W. Rascher, R. Janka, W. Bautz, J. Chen, B. Kiefer, P. Schmitt, H.-P. Hollenbach, J. Shen, M. Oberle, D. Szczerba, A. Kam, J. W. Guag, and N. Kuster, "The Virtual Family-development of surface-based anatomical models of two adults and two children for dosimetric simulations," *Physics in Medicine and Biology*, vol. 55, no. 2, pp. N23–N38, 2010.

[25] J. Snaar, W. Teeuwisse, M. Versluis, M. van Buchem, H. Kan, N. Smith, and A. Webb, "Improvements in high-field localized MRS of the medial temporal lobe in humans using new deformable high-dielectric materials," *NMR in Biomedicine*, vol. 24, no. 7, pp. 873–879, 2011.

[26] K. R. O'Brien, A. W. Magill, J. Delacoste, J. P. Marques, T. Kober, H.-P. Fautz, F. Lazeyras, and G. Krueger,

"Dielectric pads and low- B1+ adiabatic pulses: Complementary techniques to optimize structural T1w whole-brain MP2RAGE scans at 7 tesla," *Journal of Magnetic Resonance Imaging*, vol. 40, no. 4, pp. 804–812, 2014.

[27] K. Nehrke and P. Börnert, "DREAM-a novel approach for robust, ultra-fast, multislice B1 mapping," *Magnetic Resonance in Medicine*, vol. 68, no. 5, pp. 1517–1526, 2012.

[28] A. C. Antoulas, *Approximation of large-scale dynamical systems*. Society for Industrial and Applied Mathematics (SIAM, 3600 Market Street, Floor 6, Philadelphia, PA 19104), 2005.

3

MODEL ORDER REDUCTION AND OPTIMIZATION

In the previous chapter, a forward modeling method was presented which enabled us to efficiently compute the RF responses of dielectric pads. The method becomes less efficient, however, when the dimension of the pad increases. In this chapter, the developed model is reduced in complexity to achieve even lower computation times, and the model is transformed into one that is suitable for optimization-based techniques. To this end, it is parameterized in terms of the pad's dimensions, location, and constitution. Subsequently, a projection-based model reduction technique is used to decrease the problem size to a great extent, after which it is incorporated into a Gauss-Newton nonlinear optimization scheme. Optimal dielectric pads are designed for cerebellum imaging and measurements validate the effectiveness of these pads.

This chapter has been published in IEEE Transactions in Medical Imaging.
(Volume: 37, Issue: 4, 2018)

3.1. INTRODUCTION

MAGNETIC Resonance Imaging (MRI) is a non-invasive technique that can be used to create detailed images of the anatomy of the human body. The signal-to-noise ratio (SNR) of these images can be significantly improved by using higher static magnetic fields, which in turn enables reduced scan times and MR images with a higher spatial resolution [1]. The frequency of the radiofrequency (RF) excitation field that is used for MR imaging is linearly related to the magnitude of the static magnetic field, explicitly

$$f = \gamma B_0,$$

where γ [Hz/T] is the gyromagnetic ratio and B_0 the magnitude of the static field. For ^{1}H the gyromagnetic ratio is $\gamma = 42.576 \cdot 10^6$ Hz/T and consequently the frequency of the RF field is approximately 64 MHz, 128 MHz, and 298 MHz for MR systems with a field strength of 1.5T, 3T, and 7T, respectively.

To acquire high quality MR images the magnitude of the forward circularly polarized component of the RF magnetic field should be strong and uniform. In terms of the Cartesian components of the magnetic flux density phasor, this component is given by

$$B_1^+ = \frac{B_x + \mathrm{j}B_y}{2},$$

where j is the imaginary unit. A high efficiency with respect to input power is desired, defined as $|B_1^+|/\sqrt{P_{in}}$, to ensure minimal energy to be deposited in the subject and to enable a wider range of sequences to be ran within the peak power limitations of the system. However, the increase in RF frequency for higher field strengths leads to a shortening of the RF wavelength in tissue, leading to interference effects that reduce the uniformity of the $|B_1^+|$ distribution. Resulting areas of low transmit sensitivity translate into areas of low signal intensity and reduced contrast in the resulting MR images, limiting the image quality [2–6].

The RF uniformity can be improved by active or passive RF shimming techniques that tailor the B_1^+ field distribution. The active method uses transmit arrays and involves advanced additional hardware [7, 8]. Although many studies have been published on active RF shimming, complex issues of calculating the power deposited in the patient with variable transmit phases from the individual elements of the array have meant that this approach has not yet been used clinically, except for two-channel body coil shimming for clinical 3T systems. The alternative approach using passive RF shimming in the form of dielectric pads, on the other hand, is relatively cheap and easy to use. Typically, these dielectric pads are placed in the vicinity of the region of interest (ROI) and have a high relative permittivity up to 300 [9]. A properly designed pad, that is, a pad with the correct dimensions, constitution, and appropriate position, will generate a B_1^+ field perturbation that adds constructively to the total B_1^+ distribution and consequently on the acquired image [10–18].

Obtaining an optimal pad design is not straightforward, however, and the correct positioning of such a pad is in general not known. Therefore, it involves a multitude of design parameters that need to be optimized. To obtain the optimal pad design for a specific case it is common practice to perform a parametric design study by evaluating the

RF response of a large number of pad realizations with different dimensions, locations, and constitution. As the parameter space is very large, and it involves a very large computational domain encompassing a heterogeneous body model and coil model, such trial-and-error approaches are in general very time consuming, involve many human interactions, can only address a limited set of parameters, and often are not guided by any enforced optimality principle. Furthermore, the optimal design may vary with variations in the size and shape of the subject's anatomy. In addition, when the transmit antennas in a certain configuration differ from another configuration, or when the magnitude of the B_0 differs, a new pad should be designed. As each application requires a dedicated pad, it is beneficial to have a fast, structured, and efficient method for designing dielectric pads.

In our previous work [13, 19], we proposed a scattering formalism to significantly reduce the computation time for B_1^+ field evaluations of dielectric pads. The general idea in this approach is to first identify a spatial domain outside the body where the dielectric pad could be located, referred to as the "design domain." The design domain is typically very small compared with the total computational domain, which allows efficient evaluation of the B_1^+ field distribution from a specific pad that is confined within this domain. Although this method is efficient for evaluating single pad realizations, it does not yield sufficient acceleration to address the design problem efficiently and systematically.

In this paper, we extend our previous work by reducing the dimensionality of the model and subsequently using this reduced model in an optimization method to design dielectric pads. First, we exploit the fact that the constitution of practical pads does not vary on a voxel-by-voxel scale and it is therefore not necessary to allow for voxelwise variation in the constitution and size of a pad. The design domain is therefore subdivided into large nonoverlapping subdomains. Hereafter, we describe a pad in terms of parameters that control its dimensions, position, and constitution Subsequently, this parametric field representation is reduced via a projection based model order reduction technique [20] which decreases the computation time for single pad evaluations further. We can now design pads very efficiently by minimizing a cost functional that measures the discrepancy between the reduced-order field representations and a desired B_1^+ field distribution. Finally, we demonstrate the effectiveness of our approach by designing a dielectric pad for imaging the cerebellum at 7T, which is a difficult region to scan with commonly available RF head coils [21–32]. A parametric pad design study of the cerebellum has not been shown before, and therefore we use such a study here to demonstrate the method.

3.2. METHODS

Spatially discretizing Maxwell's equations on a standard staggered finite-difference grid (Yee grid, [33]) and applying the above mentioned scattering formalism, the discretized B_1^+ field can be written as [19]

$$\mathsf{B}_1^+(\mathsf{c}) = \mathsf{B}_1^{+;\text{no pad}} + \mathsf{G}^{B_1^+\mathrm{J}}\left[\mathsf{I}_P - \mathsf{X}_{\text{pad}}(\mathsf{c})\mathsf{G}^{\mathrm{EJ}}\right]^{-1}\mathsf{X}_{\text{pad}}(\mathsf{c})\mathsf{E}^{\text{no pad}}, \tag{3.1}$$

where $\mathsf{B}_1^{+;\text{no pad}}$ represents the simulated and discretized B_1^+ field without a dielectric pad, whereas the second term on the right-hand side is the scattered B_1^+ field due to a

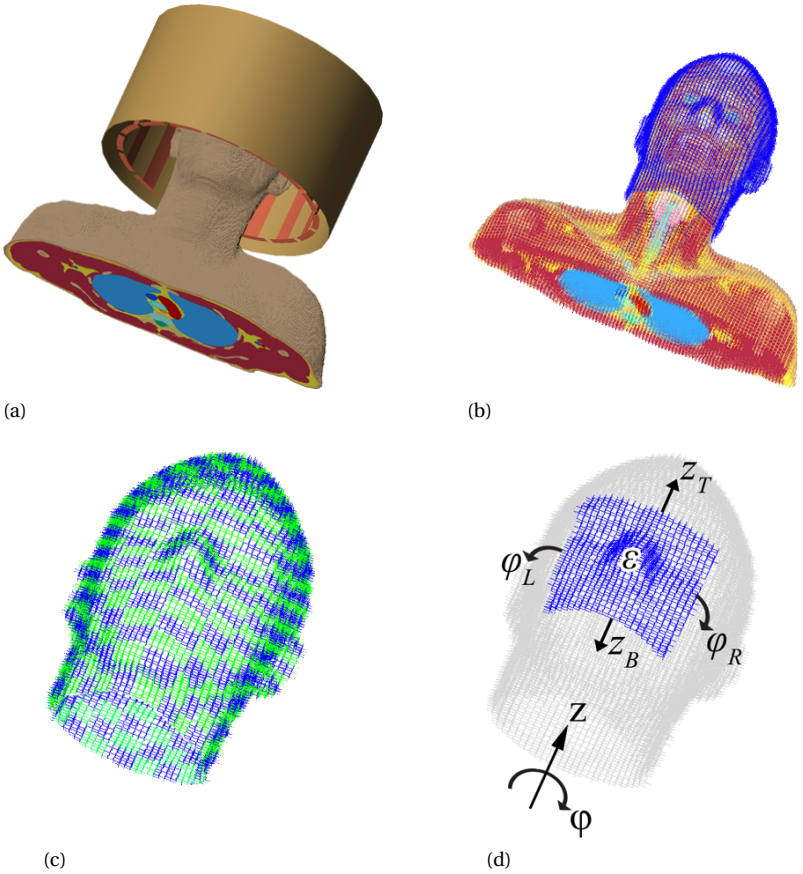

Figure 3.1: Head and shoulders of the male body model Duke, head coil, and shield used for enhanced imaging of the cerebellum (a). The pad design domain defined all around the head model (b). Pad design domain subdivided into subdomains (c). Illustration of the pad design parameters (d).

dielectric pad, $\mathsf{E}^{\text{no pad}}$ is the simulated and discretized background electric field strength in the pad design domain when no pad is present and, finally, $\mathsf{X}_{\text{pad}} = \text{diag}(\mathsf{c})$ is a diagonal contrast matrix that is used to define the dielectric pad (dimensions, location, and constitution) within the pad design domain. Its diagonal elements are defined by the P-by-1 vector $\mathsf{c} = [c_1, c_2, ..., c_P]^T$ with

$$c_p = \sigma(\mathbf{r}_{k_p}) + \mathrm{j}\omega\varepsilon_0[\varepsilon_\mathrm{r}(\mathbf{r}_{k_p}) - 1]$$

for $p = 1, 2, ..., P$ and where $\sigma(\mathbf{r}_k)$ and $\varepsilon_\mathrm{r}(\mathbf{r}_k)$ are the conductivity and relative permittivity at grid edge location $\mathbf{r}_k$ with $k \in \mathscr{P} = \{k_1, k_2, \ldots, k_P\}$. Here, $\mathscr{P}$ is the index set of the pad design domain and P the total number of grid edges belonging to this domain. G^{EJ} and $\mathsf{G}^{B_1^+\text{J}}$ are the discretized Green's tensors of the inhomogeneous background that map electric currents to the electric field strength and B_1^+ field, respectively. The former is used to compute the electric current distribution in the pad design domain, whereas the

latter maps this electric current distribution to the B_1^+ field in the ROI. These discretized tensors are constructed one column at a time by computing the field responses due to Hertzian dipoles located at primary edges that belong to the pad design domain. Since these tensors are independent of the dielectric pad, we only have to compute them once and we store the computed field responses in what we call the Full Order Library (FOL). Having this library available, the scattered field due to any dielectric pad located within the pad design domain can now be efficiently computed, since for each realization only a system of order $P \ll N$ has to be solved, with N being the number of grid edges in the total computational domain.

CONSTRUCTING DIELECTRIC SUBDOMAINS

In the above scattering formalism, the conductivity and relative permittivity can vary on a voxel-by-voxel scale within the pad design domain. Allowing for this many degrees of freedom is not needed, however, since pads that vary in their constitution on a voxel scale are never realized in practice. We therefore reduce the number of unknowns by first subdividing the design domain into subdomains with constant material parameters, and then describing the dielectric pad as a collection of these subdomains. Taking the diagonal matrix representation $\mathsf{X}_{\text{pad}} = \text{diag}(\mathsf{c})$ as a starting point, we form dielectric subdomains by specifying the same material properties at grid edges that belong to a certain subdomain. Consequently, with a pad domain that is subdivided into D nonoverlapping homogeneous subdomains, the contrast matrix can be written as

$$\mathsf{X}_{\text{pad}} = \sum_{i=1}^{D} c_i \mathsf{X}_{\text{pad};i}, \tag{3.2}$$

where c_i is the contrast of the ith subdomain and $\mathsf{X}_{\text{pad};i}$ is its diagonal P-by-P support matrix. Substitution of this decomposition in Eq. (3.1) gives

$$\mathsf{B}_1^+ = \mathsf{B}_1^{+;\text{no pad}} + \mathsf{G}^{B_1^+\text{J}} \left[\mathsf{I}_P - \sum_{i=1}^{D} c_i \mathsf{G}_i^{\text{EJ}} \right]^{-1} \sum_{i=1}^{D} c_i \mathsf{X}_{\text{pad};i} \mathsf{E}^{\text{no pad}}, \tag{3.3}$$

where we have introduced the P-by-P Greens tensor matrix that corresponds to the ith subdomain as $\mathsf{G}_i^{\text{EJ}} = \mathsf{X}_{\text{pad};i}\mathsf{G}^{\text{EJ}}$ for $i = 1, 2, \ldots, D$. Figure 3.1c shows a subdivision of the pad design domain of Figure 3.1b into subdomains. The contrast within each subdomain is constant.

PAD PARAMETRIZATION

The majority of dielectric pads that are realized in practice have a rectangular shape and are homogeneous. To take this into account in our subdomain formalism, we introduce a set of pad design parameters that fully describe such practical pads. Specifically, in cylindrical coordinates (with the z-axis parallel to the bore of the MRI scanner), the z-coordinate of the bottom and top edge of a pad are denoted by z_{B} and z_{T}, respectively, while the edges of the pad in the azimuthal direction have φ_{L} and φ_{R} as angular coordinates (see Figure 3.1d). Furthermore, since the pads are typically homogeneous, the conductivity σ and relative permittivity ε_{r} of the pad are constant. In our implementation, we fix the conductivity of the pad, since the B_1^+ field is generally much more sensi-

tive to variations in the permittivity. For simplicity, we do not vary the thickness of the pad either, but we stress that, if desired, thickness variations can be included as well.

To summarize, the parameters that we use to describe a pad within the pad design domain are the coordinates z_B, z_T, φ_L, φ_R, and the relative permittivity ε_r of the pad as shown in Figure 3.1d. To indicate that the B_1^+ field depends on these parameters, we write $\mathsf{B}_1^+ = \mathsf{B}_1^+(\mathsf{p})$, where p is the parameter vector

$$\mathsf{p} = \left[z_\mathrm{B}, z_\mathrm{T}, \phi_\mathrm{L}, \phi_\mathrm{R}, \varepsilon_\mathrm{r}\right]^T. \tag{3.4}$$

Finally, to enforce a rectangular shape for a dielectric pad, we use an approximation of the Heaviside step function given by

$$\tilde{u}(x,k) = \frac{1}{1+\exp(-2kx)},$$

where k determines the smoothness (i.e. $k \to \infty$ gives the true Heaviside function) and x is a normalized coordinate. By using these approximate step functions for each of the cylindrical coordinates z and φ separately, we are able to impose a rectangular shape for the pads into our subdomain formalism. In particular, the pad parametrization can be included through the parameter dependent contrast functions

$$\begin{aligned}
&\mathsf{f}_i(\mathsf{p}) = \left[\sigma + \mathrm{j}\omega\varepsilon_0(\varepsilon_\mathrm{r}-1)\right]\cdot \\
&\left\{\tilde{u}\left[\frac{1}{z_\ell}(z_i - z_\mathrm{T}), k\right] - \tilde{u}\left[\frac{1}{z_\ell}(z_i - z_\mathrm{B}), k\right]\right\}\cdot \\
&\left\{\tilde{u}\left[\frac{1}{2\pi}(\varphi_i - \varphi_\mathrm{L}), k\right] - \tilde{u}\left[\frac{1}{2\pi}(\varphi_i - \varphi_\mathrm{R}), k\right] + \right. \\
&\tilde{u}\left[\frac{1}{2\pi}(\varphi_i - \varphi_\mathrm{L} + 2\pi), k\right] - \tilde{u}\left[\frac{1}{2\pi}(\varphi_i - \varphi_\mathrm{R} + 2\pi), k\right] + \\
&\left.\tilde{u}\left[\frac{1}{2\pi}(\varphi_i - \varphi_\mathrm{L} - 2\pi), k\right] - \tilde{u}\left[\frac{1}{2\pi}(\varphi_i - \varphi_\mathrm{R} - 2\pi), k\right]\right\}.
\end{aligned} \tag{3.5}$$

where z_i and φ_i are the coordinates of the midpoint of the ith subdomain and z_ℓ is the length of the pad design domain, as illustrated in Fig. 3.2. The first term on the right-hand side of Eq. (3.5) determines the shape in the z-direction, whereas the other three terms determine the shape in the φ-direction. The third and fourth term are two shifted versions of the second term (over 2π and -2π, respectively) to enforce continuity. Finally, the arguments of the approximated Heaviside functions are normalized such that the smoothness parameter k has the same influence on all normalized coordinates.

With the introduction of the contrast functions of Eq. (3.5), the parameter dependent expression for the B_1^+ field is given by

$$\mathsf{B}_1^+(\mathsf{p}) = \mathsf{B}_1^{+;\text{no pad}} + \mathsf{G}^{B_1^+\mathrm{J}}\left[\mathsf{I}_P - \sum_{i=1}^{D}\mathsf{f}_i(\mathsf{p})\mathsf{G}_i^{\mathrm{EJ}}\right]^{-1}\sum_{i=1}^{D}\mathsf{f}_i(\mathsf{p})\mathsf{X}_{\text{pad};i}\mathsf{E}^{\text{no pad}}. \tag{3.6}$$

This parameterized field expression serves as a starting point in the projection based model reduction technique discussed in the next section.

PROJECTION BASED MODEL REDUCTION

By introducing the electric current state vector as

$$\mathsf{j}(\mathsf{p}) = \left[\mathsf{I}_P - \sum_{i=1}^{D} \mathsf{f}_i(\mathsf{p})\mathsf{G}_i^{\mathrm{EJ}}\right]^{-1} \sum_{i=1}^{D} \mathsf{f}_i(\mathsf{p})\mathsf{X}_{\mathrm{pad};i}\mathsf{E}^{\mathrm{no\ pad}}, \tag{3.7}$$

representing the conduction currents and the displacements currents in the pad design domain, the B_1^+ field of Eq. (3.6) can be written as

$$\mathsf{B}_1^+(\mathsf{p}) = \mathsf{B}_1^{+;\mathrm{no\ pad}} + \mathsf{G}^{B_1^+\mathrm{J}}\mathsf{j}(\mathsf{p}). \tag{3.8}$$

This equation provides a direct relationship between the B_1^+ field within the region of interest and induced electric currents with their support in the pad design domain. Obviously, different pad realizations produce different induced currents densities resulting in different B_1^+ field patterns within a region of interest. According to Eq. (3.7), to obtain the current vector $\mathsf{j}(\mathsf{p})$ for a certain pad relatization as described by the parameter vector p, a system of order P has to be solved. Even though this order is much smaller than the total order N of the system, a further reduction may be achieved by representing a general current vector $\mathsf{j}(\mathsf{p})$ in terms of a reduced basis consisting of $r \ll P$ basis vectors. If such a reduced basis can be found, then evaluating specific pad realizations would involve solving a system of order r instead of order P. This is particularly beneficial in a pad optimization framework (see Section 3.2), since it allows us to efficiently compute B_1^+ fields due to pads with different pad design parameters.

To find a reduced order basis for the induced current densities, we follow a Projection Based Model Reduction approach as outlined in [20], for example. Specifically, for a given set of different pad design vectors $\mathsf{p}_1, \mathsf{p}_2, ..., \mathsf{p}_S$, we first compute the corresponding

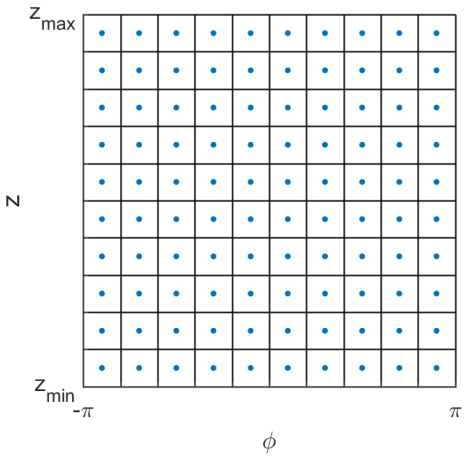

Figure 3.2: Subdomains of the the pad design domain. The coordinates of the subdomain $\{\varphi_i, z_i\}$ refer to the midpoint of each subdomain indicated by the dot. The length of the pad design domain is z_ℓ, i.e. $z_\ell = |z_{\max} - z_{\min}|$.

induced current densities $\mathsf{j}(\mathsf{p}_1)$, $\mathsf{j}(\mathsf{p}_2)$, ...,$\mathsf{j}(\mathsf{p}_S)$ and store these distributions as columns in a snapshot matrix S, i.e.

$$\mathsf{S} = [\mathsf{j}_1(\mathsf{p}_1)\ldots\mathsf{j}_S(\mathsf{p}_S)] \tag{3.9}$$

where $S \geq 1$ is the number of snapshots. Subsequently, we compute the thin singular value decomposition of the snapshot matrix. This decomposition is given by

$$\mathsf{S} = \mathsf{U}\Sigma\mathsf{V}^H,$$

where the columns of U and V are the left and right singular vectors of the snapshot matrix, while Σ is a diagonal matrix with positive decreasing singular values on its diagonal, i.e. $\sigma_i \geq \sigma_{i+1}$. To remove possible redundancy among the computed currents $\mathsf{j}(\mathsf{p}_i)$, we now take the r most significant left-singular vectors corresponding to the r largest singular values as basis vectors to describe an arbitrary current distribution $\mathsf{j}(\mathsf{p})$. In other words, we approximate the current distribution by the reduced-order model

$$\mathsf{j}_r(\mathsf{p}) = \alpha_1(\mathsf{p})\mathsf{u}_1 + \alpha_2(\mathsf{p})\mathsf{u}_2 + \ldots + \alpha_r(\mathsf{p})\mathsf{u}_r = \mathsf{U}_r\mathsf{a}_r(\mathsf{p}),$$

where the basis matrix U_r has the column partitioning $\mathsf{U}_r = [\mathsf{u}_1, \mathsf{u}_2, ..., \mathsf{u}_r]$ and $\mathsf{a}_r(\mathsf{p}) = [\alpha_1(\mathsf{p}), ..., \alpha_r(\mathsf{p})]^T$ is the vector of expansion coefficients. To find these coefficients, we require that the residual of the reduced-order model

$$\mathsf{r} = \sum_{i=1}^{D} \mathsf{f}_i(\mathsf{p})\mathsf{X}_{\mathrm{pad};i}\mathsf{e}^{\mathrm{no\ pad}} - \left[\mathsf{I}_P - \sum_{i=1}^{D} \mathsf{f}_i(\mathsf{p})\mathsf{G}_i^{\mathrm{EJ}}\right]\mathsf{U}_r\mathsf{a}_r(\mathsf{p})$$

is orthogonal to the basis vectors u_i, $i = 1, 2, ..., r$, that is, the expansion coefficients are found from the Galerkin condition $\mathsf{U}_r^H\mathsf{r} = 0$ as

$$\mathsf{a}_r(\mathsf{p}) = \left[\mathsf{I}_r - \sum_{i=1}^{D} \mathsf{f}_i(\mathsf{p})\mathsf{G}_i^{\mathrm{EJ};r}\right]^{-1} \sum_{i=1}^{D} \mathsf{f}_i(\mathsf{p})\mathsf{X}_{\mathrm{pad};i}^{r}\mathsf{E}^{\mathrm{no\ pad}}, \tag{3.10}$$

where I_r is the identity matrix of order r and where we have introduced the reduced matrices $\mathsf{G}_i^{\mathrm{EJ};r} = \mathsf{U}_r^H\mathsf{G}_i^{\mathrm{EJ}}\mathsf{U}_r$ and $\mathsf{X}_{\mathrm{pad};i}^{r} = \mathsf{U}_r^H\mathsf{X}_{\mathrm{pad};i}$. It should be noted that, in order to compute the expansion coefficients, a system of order r needs to be solved instead of a system of order P as in Eq. (3.6). Finally, substituting the reduced-order model for the currents in Eq. (3.8), we arrive at the reduced-order model for the B_1^+ field as

$$\mathsf{B}_1^{+;r}(\mathsf{p}) = \mathsf{B}_1^{+;\mathrm{no\ pad}} + \mathsf{G}^{B_1^+\mathrm{J};r}\mathsf{a}_r(\mathsf{p}), \tag{3.11}$$

where $\mathsf{G}^{B_1^+\mathrm{J};r} = \mathsf{G}^{B_1^+\mathrm{J}}\mathsf{U}_r$ maps the expansion vector of the currents as given by Eq. (3.10) to the B_1^+ field. The reduced matrices $\mathsf{G}_i^{\mathrm{EJ};r}$, $\mathsf{X}_{\mathrm{pad};i}^{r}$, and $\mathsf{G}^{B_1^+\mathrm{J};r}$ constitute the reduced order library (ROL).

PAD DESIGN FOR CEREBELLUM IMAGING

Having the parametrized reduced-order model for the B_1^+ field as given by Eq. (3.11), allows the design of an optimal pad for a certain ROI within the human body. As an

illustrative example, we focus on imaging of the cerebellum at 7T, but we stress that the approach can equally be applied to other parts of the human body as well.

To find a pad design for which the amplitude of the B_1^+ field is as uniform as possible within the ROI, we minimize the cost function

$$C(\mathsf{p}) = \frac{1}{2} \frac{\|\mathsf{B}_1^{+;r}(\mathsf{p}) - \mathsf{B}_1^{+;\text{desired}}\|_2^2}{\|\mathsf{B}_1^{+;\text{desired}}\|_2^2}, \tag{3.12}$$

over all feasible pad parameter vectors p, where $\mathsf{B}_1^{+;r}(\mathsf{p})$ and $\mathsf{B}_1^{+;\text{desired}}$ are the modeled and desired B_1^+ fields within the ROI, respectively. Since we only prescribe the amplitude of the desired B_1^+ field throughout the ROI (1 μT, for example) we follow [34] and take

$$\mathsf{B}_1^{+;\text{desired}} = b \exp\left[\mathrm{j} \angle \mathsf{B}_1^{+;r}(\mathsf{p})\right], \tag{3.13}$$

for the desired complex B_1^+ field, where b is the prescribed amplitude. In other words, the phase of the desired field is set equal to the phase of the current B_1^+ field.

Since the cost functional of Eq. (3.12) defines a nonlinear least squares problem, we minimize $C(\mathsf{p})$ using the standard Levenberg-Marquardt algorithm [35]. This minimization procedure should take place over feasible pad parameter vectors, i.e. describing physically realizable dielectric pads. We include this requirement by imposing the constraints $\varepsilon_\mathrm{r} \geq 1$, $|\varphi_\mathrm{R} - \varphi_\mathrm{L}| \geq \ell$, $|z_\mathrm{T} - z_\mathrm{B}| \geq w$, and $z_\mathrm{T} \leq d$. The first constraint is implemented by writing the relative permittivity as $\varepsilon_\mathrm{r} = 1 + \epsilon^2$ and taking ϵ as an optimization parameter. The second and third constraint are implemented by setting the length and width of the pad to the minimum length ℓ and minimum width w, respectively, whenever a length or width is found that is smaller than these prescribed minima. The last constraint is included so that no pads will be positioned at the top of the head, since the contrast functions $f_i(\mathsf{p})$ degenerate into triangles in this region. The triangles result since all subdomains in this region are bend to the same center point on top of the head. We implement this constraint by setting z_T equal to its permitted value d whenever we encounter a z_T for which the fourth constraint is not satisfied. Finally, we note that since the reduced-order model for the B_1^+ field is used to describe the B_1^+ field, only systems of order r need to be solved to determine the elements of the Jacobian, since the pad parameters occur in the r expansion coefficients $\alpha_i(\mathsf{p})$ only.

3.3. IMPLEMENTATION AND RESULTS

To illustrate the performance of our dielectric pad design procedure, we have divided this section into three parts. First, we construct an FOL without any model reduction using the technique proposed in our previous work [19]. We subsequently reduce this library using the parametric reduced-order modeling techniques described in Section 3.2. These reduction techniques produce an ROL and we demonstrate the accuracy of the ROL by comparing B_1^+ field maps computed with the FOL with B_1^+ maps computed using the ROL. Finally, in the third part, we design a dielectric pad for cerebellum imaging, after which we validate our design using an MR measurement.

CREATING THE FULL ORDER LIBRARY

The configuration that is used for simulations is depicted in Fig. 3.1a and consists of the head and shoulders of the male body model "Duke" from the Virtual Family dataset [36], and a shielded 16-rung high-pass birdcage coil. The coil has an inner radius of 15 cm and outer radius of 18 cm and operates in quadrature mode at a frequency of 298 MHz which corresponds to the ^{1}H Larmor frequency at 7T. The birdcage is tuned using 6.7 pF capacitors and driven by two current sources. The resulting electromagnetic fields from this loaded coil have been normalized to 1 W input power. These fields are computed using XFdtd software (v.7.5.0.3,Remcom State College, PA, USA) with a voxel size of 5 mm^3. Computations are performed on a Windows 64-bit machine with an Intel Xeon CPU X5660 @ 2.80 GHz (dual core) with 48 GB internal memory and two NVIDIA Tesla K40c GPU's.

The pad design domain is defined as a continuous layer covering the head with a thickness of 1 cm (to fit inside the close-fitting 32-channel receive array) as depicted in Fig. 3.1b. This domain consists of about $P = 27,000$ FDTD primal grid edges, i.e. edges where the material of a dielectric pad can be defined. As outlined above, for each grid edge in the pad design domain we perform a single simulation, after which the FOL is constructed. Constructing this library took approximately 48 hrs and results in 30 GB of data. We note that, once it is generated, any pad within the pad domain can be modeled using this library.

CREATING THE REDUCED ORDER LIBRARY

To compress the library, we now divide the pad design domain into $D = 400$ subdomains with 20 subdivisions in the z-direction and 20 subdivisions in the φ-direction as illustrated in Fig. 3.1d. The average resolution of one subdomain is about $3 \times 1.2 \times 1$ cm^3 ($\varphi \times z \times$ thickness).

Subsequently, the snapshot matrix S of Eq. (3.9) is constructed by performing $S = 2000$ simulations in Remcom XFdtd for different pad realizations described by the parameters of Eq. (3.4). For each pad, the pad parameters are chosen randomly (using the function *rand* in Matlab) and such that the pads have a minimum width of $w = 3$ cm, a minimum length of $\ell = \pi/5$, and a top edge z-coordinate that satisfies $z_T < 5$ cm. These

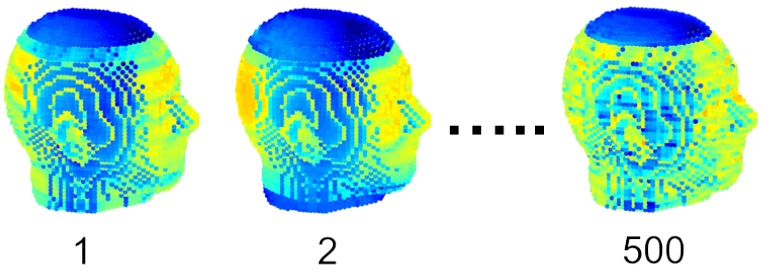

Figure 3.3: Illustration of the first, second, and 500$^{\text{th}}$ left singular vector of the snapshot matrix are shown. These vectors represent electric currents in the pad design domain.

parameters constraints were also used in the Levenberg-Marquardt algorithm during the pad design stage (see below). Moreover, all randomly generated pads have a relative permittivity smaller than 500, since pads with a higher relative permittivity are difficult to realize in practice. In each simulation, the electric current density in the pad design domain is computed and stored as a column in the snapshot matrix S.

Having the snapshot matrix available, we compute its SVD. We select the first $r = 500$ left singular vectors as expansion vectors in our reduced-order model ($\sigma_{500} = 0.0044$). As a rule, we generally include all left singular vectors in our reduced order basis for which the corresponding normalized singular values are larger than 0.004. Three of these singular vectors are shown in Fig. 3.3, which physically represent electric currents in the pad design domain.

With the 500 most dominant singular vectors at our disposal, we now form the reduced matrices $\mathsf{G}_i^{\mathrm{EJ};r} = \mathsf{U}_r^H \mathsf{G}_i^{\mathrm{EJ}} \mathsf{U}_r$, $\mathsf{X}_{\mathrm{pad};i}^r = \mathsf{U}_r^H \mathsf{X}_{\mathrm{pad};i}$, and $\mathsf{G}^{B_1^+\mathrm{J};r} = \mathsf{G}^{B_1^+\mathrm{J}} \mathsf{U}_r$. As mentioned above, these matrices constitute the ROL and this library requires significantly less memory than the FOL. To be specific, for the problem considered here, disk storage for the ROL is approximately 1 GB, which amounts to a storage reduction factor of 30 compared with the FOL storage requirement. Moreover, to compute the B_1^+ field for different pad realizations, systems of order $P = 27{,}000$ need to be solved when using the FOL, while reduced systems of order $r = 500$ need to be solved when using the ROL. In particular, for the cerebellum imaging problem considered here, a B_1^+ field evaluation for a single pad realization takes about 90 seconds on the computer system system mentioned above (using the GMRES iterative solver [37] with a tolerance of 10^{-6}) when the FOL is used, while the computation time for evaluating the reduced-order model is approximately 0.35 seconds, which amounts to a speed up factor of 260. Finally, in Fig. 3.5 we show the absolute error for three different pad realizations of the reduced-order models at cross-sections where this error is maximum (the maximum being defined over the complete head and shoulder model). We observe that the reduced-order models are in good overall agreement with the B_1^+ field computed using XFdtd and maxima in the absolute error essentially occur only at the outer periphery very close to the dielectric pads. The reduced-order fields can therefore safely be used in the pad optimization stage to efficiently design a dielectric pad for cerebellum imaging.

DESIGNING PADS

Imaging the cerebellum at 7T has its difficulties due to the reduced RF homogeneity. At this particular ROI, there is a substantial drop-off in the sensitivity of the volume transmit coil that leads to poor image quality (see Fig. 3.7a and Fig. 3.7b). The simulated background B_1^+ field (i.e. without any pad) is shown in the left column of Fig. 3.6 for a coronal and transverse slice through the cerebellum. Clearly, we can see the reduced transmit sensitivity in the cerebellum ROI, which is outlined by the black line. Explicitly, the mean B_1^+ field in the ROI is 0.29 $\mu\mathrm{T}/\sqrt{\mathrm{W}}$ and the coefficient of variation $\mathrm{C_v}$ is 34%, i.e. the ratio of the standard deviation to the mean. Our aim is to optimize the B_1^+ field within this ROI using a dielectric pad, i.e. we aim at increasing the transmit sensitivity by designing a pad that yields a homogeneous high-intensity field.

Minimizing the cost functional from Eq. (3.12) results in optimizing both transmit efficiency and homogeneity of the B_1^+ field, but it does not address the balance between

Table 3.1: Sensitivity analysis of the optimal pad. The optimal parameters are disturbed slightly to show the effect on the C_v and the transmit efficiency.

Pad	**C_v** (%)	**Transmit efficiency** ($\mu T\sqrt{W}$)
None	34	0.29
Optimal	14	0.48
Optimal ε_r increased by 10% to 325	13	0.50
Optimal ε_r decreased by 10% to 266	16	0.46
Optimal shifted vertically by 1.2 cm	20	0.44
Optimal shifted horizontally by 3 cm	17	0.47
Optimal width changed by ±3 cm	17	0.47
Optimal length changed by ±1.2 cm	20	0.44

the two. Furthermore, the permittivity of the optimized pad is not restricted to a set a values, but can take any permittivity value. In practice, a wide range of relative permittivities can be fabricated, but only up to a maximum of 300 [9]. Therefore, to find the optimal pad that increases both transmit efficiency and homogeneity, and can be fabricated, we run the optimization algorithm multiple times for different desired field strengths, which can be done since our optimization algorithm is very efficient. To this end, the $B_1^{+;\text{desired}}$ field in the cost functional is initially set to the B_1^+ field per square root of input power that is produced by the birdcage transmit coil with no dielectric present. Repeatedly, we increase the desired field strength and optimize for the pad parameters after which we list the relative permittivity and the coefficient of variation C_v of the B_1^+ field in the cerebellum. The results are depicted in the graph of Fig. 3.4. Subsequently, the dielectric is selected that gave the best performance in terms of transmit efficiency and homogeneity, and leads to a flexible pad that can be fabricated. This corresponds to the optimization where the $B_1^{+;\text{desired}}$ field has been set to 0.48 $\mu T/\sqrt{W}$. We stress, that the trends of these curves are not known beforehand and a permittivity value that is too high can decrease both transmit efficiency and C_v.

For this particular optimization, the optimal pad has been found within 10 iterations, which takes about 30 seconds on the above mentioned computer system. The resulting pad has a relative permittivity of $\varepsilon_r = 295$ and dimensions $32 \times 9.5 \times 1$ cm^3. The transmit efficiency has increased by 66% from 0.29 $\mu T/\sqrt{W}$ to 0.48 $\mu T/\sqrt{W}$ and the coefficient of variation of the B_1^+ in the cerebellum has decreased from 34% to 14%. We subsequently fabricated this pad using a mixture of barium titanate and deuterated water [9]. For the optimum dielectric pad we carry out a sensitivity analysis to investigate the possible decrease in optimality for near-optimal parameters, as this might occur when fabricating and positioning the pad in practice. The optimal parameters are perturbed and the resulting change in the coefficient of variation and the transmit efficiency are listed, as shown in Table 3.1. This table is acquired in 3.5 seconds as forward simulations are evaluated quickly. In the worst-case scenario the C_v increases to 20% and the transmit ef-

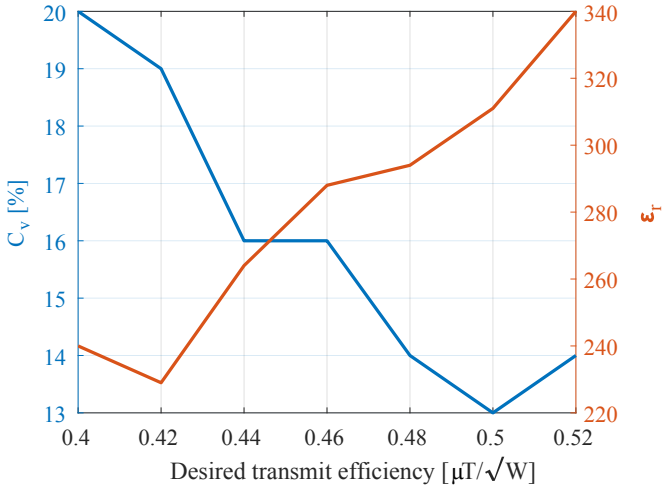

Figure 3.4: The cost functional from Eq. (3.12) is optimized for different desired transmit efficiency's. The resulting coefficient of variation is shown on the left axis and the required permittivity on the right axis.

ficiency reduces to 0.44 μT/$\sqrt{\text{W}}$ implying that the designed pad is not very sensitive to small changes.

Additionally, we investigate how this specific dielectric pad performs for a smaller female head model. To this end we replace the body model Duke in Remcom XFdtd by the female version Ella and run a simulation without dielectric pad and one with the previously-determined optimal dielectric pad. Similar performance metrics were obtained as compared to those of the male head model. Specifically, a transmit efficiency gain of 64%, from 0.32 μT/$\sqrt{\text{W}}$ to 0.53 μT/$\sqrt{\text{W}}$, and the C_v decreases from 27% to 17%.

To confirm our findings with actual measurements T1-weighted and T2-weighted scans were acquired with and without the dielectric pad, as shown in Fig. 3.7c and Fig. 3.7d, respectively. The T1-weighted scans are obtained with a 3D Turbo Field Echo sequence with a FOV of 256 × 256 × 174.4 mm^3 and an isometric resolution of 0.8 mm^3. The T2-weighted scans are acquired with a turbo spin echo sequence where a FOV is used of 107 × 240 × 198 mm^3 and an in-plane resolution of 0.8 × 0.66 mm^2. The effect of the dielectric pad is clearly visible and increases the contrast and signal intensity in the cerebellum, improving the visibility of structural details, thereby confirming that the pad designed with our optimization technique is able to significantly improve the quality of MR images.

3.4. DISCUSSION AND CONCLUSIONS

In this work we have presented a fast and efficient method for designing dielectric pads. The scattered field model presented in [19] was taken as a starting point, and we showed that the order of this model can be reduced to a great extent by employing a projection based model order reduction technique, which can subsequently be used in an optimization method. The scattered field models of [19] with an order of approximately

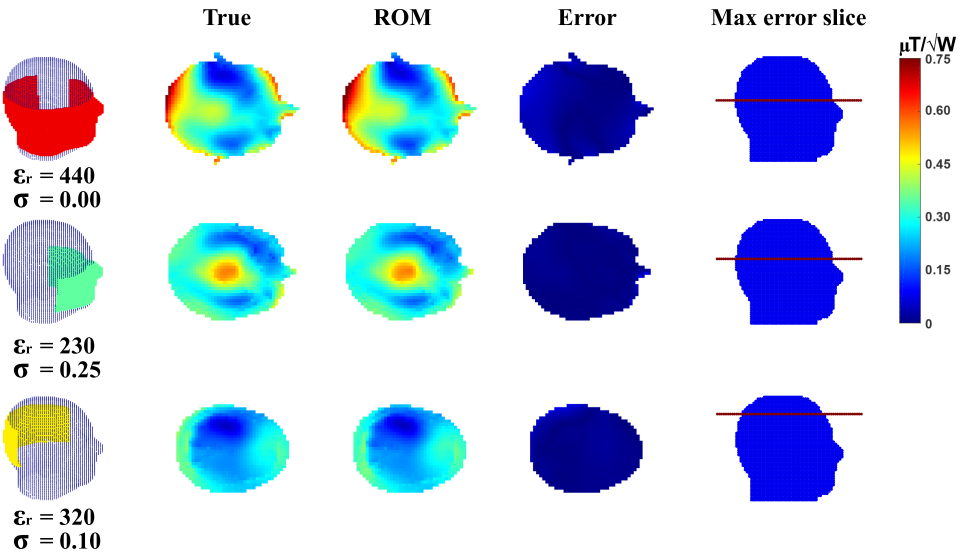

Figure 3.5: Comparison of the transmit fields for three pad realizations with different material properties. The transverse slices where the maximum absolute B_1^+ errors occur are depicted. The absolute error in the third column is shown in the same color scale.

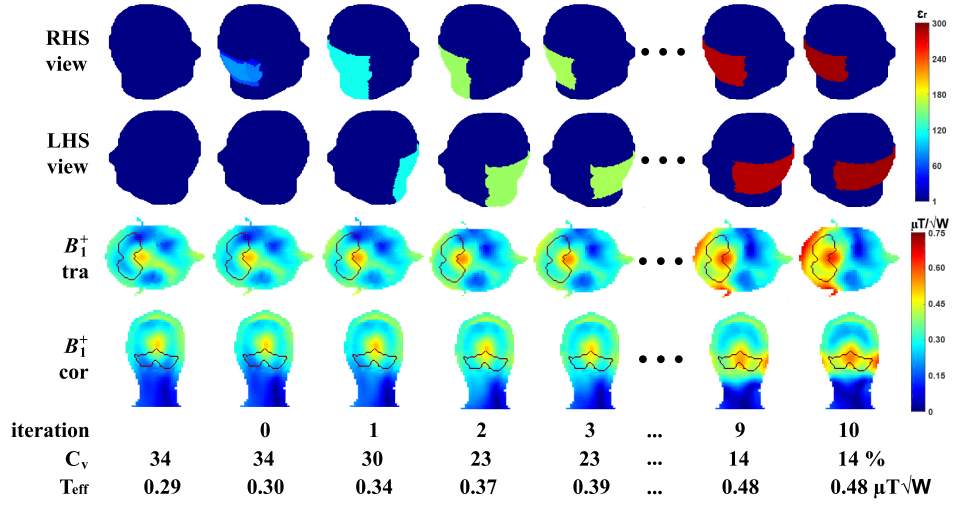

Figure 3.6: Intermediate optimization results are shown. The first and second row illustrate the right and left hand side view of the head where the pad is formed. The third and fourth row depict the B_1^+ transmit fields for the transverse and coronal slice, respectively. The cerebellum is outlined, and in this ROI the signal intensity is low. The columns show a few of the iterations of the optimization method. After 10 iterations it has converged to an optimal dielectric pad. The figures shown at the bottom of the figure depict the intermediate coefficient of variation and transmit efficiency.

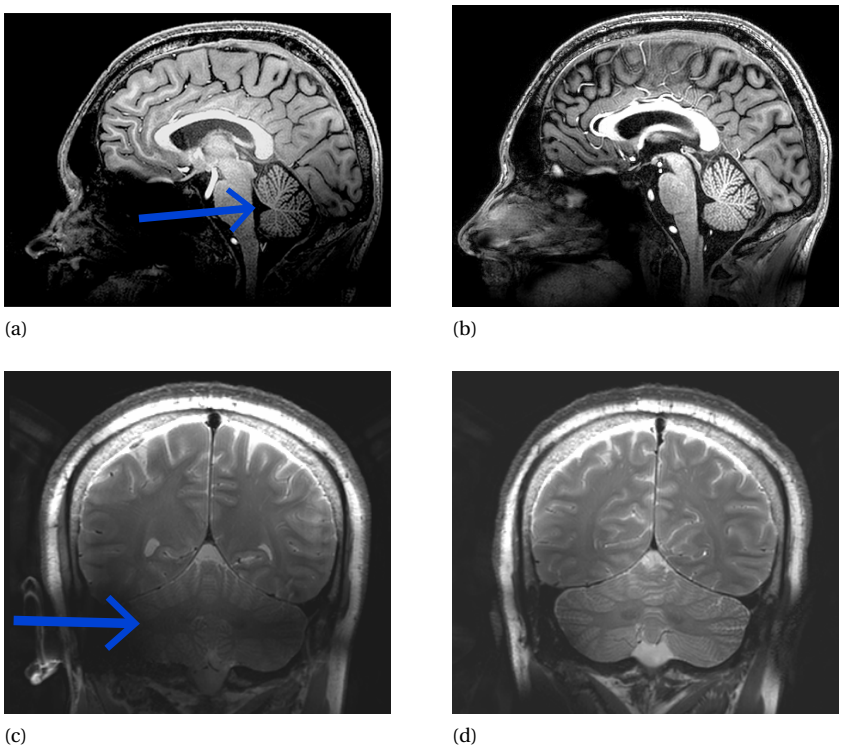

(a) (b)

(c) (d)

Figure 3.7: T1 and T2 weighted head scans of the brain at 7T (298 MHz). Low contrast is encountered in the cerebellum due to non-uniformity in the B_1^+ transmit field indicated with the arrows. Scans have been obtained on a 7T Philips Achieva, where a quadrature head coil is used for transmission and a 32 channel receive array for reception. (a) A T1-weighted turbo field echo sequence was used with a TR of 5.5 ms. 218 slices were acquired with an isometric resolution of 0.8 mm^3 and a field-of-view of $256 \times 256 \times 174$ mm^3. The total scan time was 6 minutes. (b) A T2-weighted turbo spin echo sequence was used with a field-of-view of $107 \times 240 \times 198$ mm^3 and an in-plane resolution of 0.8×0.66 mm^2. The total scan time was 1.5 minutes for 17 slices. The left column shows the results without a dielectric pad, and the right column for an optimized dielectric pad. The pad has a relative permittivity of $\varepsilon_r = 295$, a conductivity of $\sigma = 0.2$ S/m, and dimensions $32 \times 9.5 \times 1$ cm^3. The optimized pad resolves the low signal intensities at the cerebellum.

27,000 were successfully reduced to a system of order 500, thereby reducing the model order by a factor of 54. Having the reduced-order models available, B_1^+ field responses can be computed in a fraction of a second for each pad realization at the price of a negligible loss in accuracy.

The design of dielectric pads has been posed as an optimization problem in which a cost functional that measures the discrepancy between the modeled and desired B_1^+ field distribution is minimized over feasible pad parameters values, i.e. dimensions, location, and constitution. This optimization problem can be solved very efficiently, since the modeled field approximations in the cost function are of reduced-order. The optimization has been successfully applied to MR cerebellum imaging reducing the coefficient of variation by a factor 2.4. The resulting optimal pad has been fabricated and its

performance was verified in an MR imaging experiment.

The optimization results from Fig. 3.6 show that the C_v and the transmit efficiency improve for every iteration. The dielectric from the third iteration, for example, improved the transmit efficiency already by 35%, but is still far from the optimal dielectric. This enforces the need for a rigorous optimization approach as shown in this work.

The dielectric pad might couple to the birdcage coil when the permittivity value is high and/or the distance from the coil is small. This coupling is taken into account in the current work since the library is constructed with a tuned birdcage coil present in the background. However, in the rare case that the birdcage should be retuned, a new library should be constructed. In future work, we investigate whether we could combine the method with co-simulation techniques to retune the coil without constructing a new library [38].

In the design process of this work, single dielectric pads have been considered that are homogeneous and have a simple geometry. A second dielectric pad can be included in the model as well, as this is often required in practical applications [10, 14, 15, 18, 39, 40]. However, the design could be much more sophisticated. For example, more complicated dielectric structures such as pre-fractal pads add several degrees of freedom to the design process [41], hence, increasing the complexity of the design problem. The design problem becomes even more computationally challenging when optimizing multi-element dielectric pads for multi-element RF transmit and receive coil arrays, in which increasingly dielectric materials are incorporated [42]. As the coupling between the dielectric and the coils is taken into account, one could think of optimizing for SNR, the g-factor for parallel imaging, or the receive sensitivities of the individual coil elements. Therefore, an efficient way of designing these pads as presented here becomes even more relevant.

In this current work, we created the snapshot matrix by simulating a large number of random pad realizations confined to the pad design domain. Since we used the method to optimize a pad for the cerebellum specifically, it would have also sufficed to reduce the random pad realizations to a domain that is more closely related to the extent of the ROI, hence reducing the size of the ROL even further. We stress, however, that by considering the entire design domain we have obtained a reduced-order model that is more generic and application independent. The method may still benefit from a more structured approach, nonetheless, e.g. by using a greedy algorithm that determines the next snapshot on the basis of maximum error reduction [20]. However, this requires an explicit expression for the projection error which needs further investigation.

Finally, two-sided reduction techniques can further speed up the design procedure. In the present work, reduced-order models for the induced currents in the pad design domain have been constructed and the resulting B_1^+ fields are computed using the discretized electric current to B_1^+ Green's tensor (see Eq.(3.1)). Two-sided reduction techniques can also reduce the size of this operator, further reducing the complexity of the optimization potentially allowing for an even faster pad design procedure for any body part of interest.

REFERENCES

[1] R. W. Brown, Y.-C. N. Cheng, E. M. Haacke, M. R. Thompson, and R. Venkatesan, "Magnetic Resonance Imaging: Physical Principles and Sequence Design," in *Magnetic Resonance Imaging: Physical Principles and Sequence Design*, R. W. Brown, Y.-C. N. Cheng, E. M. Haacke, M. R. Thompson, and R. Venkatesan, Eds. Chichester, UK: John Wiley & Sons Ltd, 2014, ch. Magnetic R, p. 6.

[2] O. Dietrich, M. Reiser, and S. Schoenberg, "Artifacts in 3-T MRI: physical background and reduction strategies." *European Journal of Radiology*, vol. 65, no. 1, pp. 29–35, 2008.

[3] M. Bernstein, J. Huston, and H. Ward, "Imaging artifacts at 3.0 T," *Journal of Magnetic Resonance Imaging*, vol. 24, no. 4, pp. 735–746, 2006.

[4] K. Chang and I. Kamel, "Abdominal imaging at 3T: Challenges and solutions," *Applied Radiology*, vol. 39, no. 10, p. 22, 2010.

[5] K. Sung and K. Nayak, "Measurement and characterization of RF nonuniformity over the heart at 3T using body coil transmission," *Journal of Magnetic Resonance Imaging*, vol. 27, no. 3, pp. 643–648, 2008.

[6] J. T. Vaughan, M. Garwood, C. M. Collins, W. Liu, L. DelaBarre, G. Adriany, P. Andersen, H. Merkle, R. Goebel, M. B. Smith, and K. Ugurbil, "7T vs. 4T: RF power, homogeneity, and signal-to-noise comparison in head images." *Magnetic Resonance in Medicine*, vol. 46, no. 1, pp. 24–30, 2001.

[7] P.-F. Van de Moortele, C. Akgun, G. Adriany, S. Moeller, J. Ritter, C. M. Collins, M. B. Smith, J. T. Vaughan, and K. Uurbil, "B1 destructive interferences and spatial phase patterns at 7 T with a head transceiver array coil," *Magnetic Resonance in Medicine*, vol. 54, no. 6, pp. 1503–1518, 2005.

[8] C. A. T. Van den Berg, B. van den Bergen, J. B. Van de Kamer, B. W. Raaymakers, H. Kroeze, L. W. Bartels, and J. J. W. Lagendijk, "Simultaneous B1+ homogenization and specific absorption rate hotspot suppression using a magnetic resonance phased array transmit coil," *Magnetic Resonance in Medicine*, vol. 57, no. 3, pp. 577–586, 2007.

[9] T. O'Reilly, A. Webb, and W. Brink, "Practical improvements in the design of high permittivity pads for dielectric shimming in neuroimaging at 7 T," *Journal of Magnetic Resonance*, vol. 270, pp. 108–114, 2016.

[10] S. A. Winkler and B. K. Rutt, "Practical methods for improving B1+ homogeneity in 3 tesla breast imaging," *Journal of Magnetic Resonance Imaging*, vol. 41, no. 4, pp. 992–999, 2015.

[11] W. M. Teeuwisse, W. M. Brink, K. N. Haines, and A. G. Webb, "Simulations of high permittivity materials for 7 T neuroimaging and evaluation of a new barium titanate-based dielectric," *Magnetic Resonance in Medicine*, vol. 67, no. 4, pp. 912–918, 2012.

[12] W. M. Brink and A. G. Webb, "A forward model analysis of dielectric shimming in magnetic resonance imaging," in *2013 International Conference on Electromagnetics in Advanced Applications (ICEAA)*. IEEE, 2013, pp. 528–531.

[13] W. M. Brink, R. F. Remis, and A. G. Webb, "A theoretical approach based on electromagnetic scattering for analysing dielectric shimming in high-field MRI," *Magnetic Resonance in Medicine*, vol. 75, no. 5, pp. 2185–2194, 2016.

[14] W. M. Teeuwisse, W. M. Brink, and A. G. Webb, "Quantitative assessment of the effects of high-permittivity pads in 7 Tesla MRI of the brain," *Magnetic Resonance in Medicine*, vol. 67, no. 5, pp. 1285–1293, 2012.

[15] P. de Heer, W. M. Brink, B. J. Kooij, and A. G. Webb, "Increasing signal homogeneity and image quality in abdominal imaging at 3 T with very high permittivity materials," *Magnetic Resonance in Medicine*, vol. 68, no. 4, pp. 1317–1324, 2012.

[16] P. de Heer, M. B. Bizino, M. J. Versluis, A. G. Webb, and H. J. Lamb, "Improved Cardiac Proton Magnetic Resonance Spectroscopy at 3 T Using High Permittivity Pads," *Investigative Radiology*, vol. 51, no. 2, pp. 134–138, 2016.

[17] Q. X. Yang, W. Mao, J. Wang, M. B. Smith, H. Lei, X. Zhang, K. Ugurbil, and W. Chen, "Manipulation of image intensity distribution at 7.0 T: Passive RF shimming and focusing with dielectric materials," *Journal of Magnetic Resonance Imaging*, vol. 24, no. 1, pp. 197–202, 2006.

[18] W. M. Brink, A. M. van der Jagt, M. J. Versluis, B. M. Verbist, and A. G. Webb, "High Permittivity Dielectric Pads Improve High Spatial Resolution Magnetic Resonance Imaging of the Inner Ear at 7 T," *Investigative Radiology*, vol. 49, no. 5, pp. 271–277, 2014.

[19] J. H. F. Van Gemert, W. Brink, A. Webb, and R. Remis, "An Efficient Methodology for the Analysis of Dielectric Shimming Materials in Magnetic Resonance Imaging," *IEEE Transactions on Medical Imaging*, vol. 36, no. 2, pp. 666–673, 2017.

[20] A. Quarteroni and G. Rozza, *Reduced Order Methods for Modeling and Computational Reduction*, A. Quarteroni and G. Rozza, Eds. Cham: Springer International Publishing, 2014.

[21] M. A. Batson, N. Petridou, D. W. J. Klomp, M. A. Frens, and S. F. W. Neggers, "Single Session Imaging of Cerebellum at 7 Tesla: Obtaining Structure and Function of Multiple Motor Subsystems in Individual Subjects," *PLOS ONE*, vol. 10, no. 8, p. e0134933, 2015.

[22] K. R. O'Brien, T. Kober, P. Hagmann, P. Maeder, J. Marques, F. Lazeyras, G. Krueger, and A. Roche, "Robust T1-Weighted Structural Brain Imaging and Morphometry at 7T Using MP2RAGE," *PLoS ONE*, vol. 9, no. 6, p. e99676, 2014.

[23] T. Singer, B. Seymour, J. O'Doherty, H. Kaube, R. J. Dolan, and C. D. Frith, "Empathy for Pain Involves the Affective but not Sensory Components of Pain," *Science*, vol. 303, no. 5661, pp. 1157–1162, 2004.

[24] A. Favaretto, A. Lazzarotto, D. Poggiali, G. Rolma, F. Causin, F. Rinaldi, P. Perini, and P. Gallo, "MRI-detectable cortical lesions in the cerebellum and their clinical relevance in multiple sclerosis," *Multiple Sclerosis Journal*, vol. 22, no. 4, pp. 494–501, 2016.

[25] K. R. O'Brien, A. W. Magill, J. Delacoste, J. P. Marques, T. Kober, H.-P. Fautz, F. Lazeyras, and G. Krueger, "Dielectric pads and low- B1+ adiabatic pulses: Complementary techniques to optimize structural T1w whole-brain MP2RAGE scans at 7 tesla," *Journal of Magnetic Resonance Imaging*, vol. 40, no. 4, pp. 804–812, 2014.

[26] C. J. Stoodley and J. D. Schmahmann, "Functional topography in the human cerebellum: A meta-analysis of neuroimaging studies," *NeuroImage*, vol. 44, no. 2, pp. 489–501, 2009.

[27] C. Stoodley and J. Schmahmann, "Evidence for topographic organization in the cerebellum of motor control versus cognitive and affective processing," *Cortex*, vol. 46, no. 7, pp. 831–844, 2010.

[28] R. Cabeza and L. Nyberg, "Imaging cognition II: An empirical review of 275 PET and fMRI studies." *Journal of cognitive neuroscience*, vol. 12, no. 1, pp. 1–47, 2000.

[29] H. Ito, K. Mori, M. Harada, S. Hisaoka, Y. Toda, T. Mori, A. Goji, Y. Abe, M. Miyazaki, and S. Kagami, "A Proton Magnetic Resonance Spectroscopic Study in Autism Spectrum Disorder Using a 3-Tesla Clinical Magnetic Resonance Imaging (MRI) System: The Anterior Cingulate Cortex and the Left Cerebellum," *Journal of Child Neurology*, vol. 32, no. 8, pp. 731–739, 2017.

[30] Z. Yu-Feng, H. Yong, Z. Chao-Zhe, C. Qing-Jiu, S. Man-Qiu, L. Meng, T. Li-Xia, J. Tian-Zi, and W. Yu-Feng, "Altered baseline brain activity in children with ADHD revealed by resting-state functional MRI," *Brain and Development*, vol. 29, no. 2, pp. 83–91, 2007.

[31] C. J. Stoodley, E. M. Valera, and J. D. Schmahmann, "Functional topography of the cerebellum for motor and cognitive tasks: An fMRI study," *NeuroImage*, vol. 59, no. 2, pp. 1560–1570, 2012.

[32] K. K. Hui, J. Liu, O. Marina, V. Napadow, C. Haselgrove, K. K. Kwong, D. N. Kennedy, and N. Makris, "The integrated response of the human cerebro-cerebellar and limbic systems to acupuncture stimulation at ST 36 as evidenced by fMRI," *NeuroImage*, vol. 27, no. 3, pp. 479–496, 2005.

[33] U. S. Inan and R. A. Marshall, *Numerical electromagnetics : the FDTD method*. Cambridge University Press, 2011.

[34] K. Setsompop, L. Wald, V. Alagappan, B. Gagoski, and E. Adalsteinsson, "Magnitude least squares optimization for parallel radio frequency excitation design demonstrated at 7 Tesla with eight channels," *Magnetic Resonance in Medicine*, vol. 59, no. 4, pp. 908–915, 2008.

[35] J. Pujol, "The solution of nonlinear inverse problems and the Levenberg-Marquardt method," *Geophysics*, vol. 72, no. 4, pp. W1–W16, 2007.

[36] A. Christ, W. Kainz, E. G. Hahn, K. Honegger, M. Zefferer, E. Neufeld, W. Rascher, R. Janka, W. Bautz, J. Chen, B. Kiefer, P. Schmitt, H.-P. Hollenbach, J. Shen, M. Oberle, D. Szczerba, A. Kam, J. W. Guag, and N. Kuster, "The Virtual Familydevelopment of surface-based anatomical

models of two adults and two children for dosimetric simulations," *Physics in Medicine and Biology*, vol. 55, no. 2, pp. N23–N38, 2010.

[37] Y. Saad, *Iterative methods for sparse linear systems*. Society for Industrial and Applied Mathematics (SIAM, 3600 Market Street, Floor 6, Philadelphia, PA 19104), 2003.

[38] R. A. Lemdiasov, A. A. Obi, and R. Ludwig, "A numerical postprocessing procedure for analyzing radio frequency MRI coils," *Concepts in Magnetic Resonance Part A*, vol. 38A, no. 4, pp. 133–147, 2011.

[39] W. M. Brink and A. G. Webb, "High permittivity pads reduce specific absorption rate, improve B 1 homogeneity, and increase contrast-to-noise ratio for functional cardiac MRI at 3 T," *Magnetic Resonance in Medicine*, vol. 71, no. 4, pp. 1632–1640, 2014.

[40] W. M. Brink, M. J. Versluis, J. M. Peeters, P. Börnert, and A. G. Webb, "Passive radiofrequency shimming in the thighs at 3 Tesla using high permittivity materials and body coil receive uniformity correction," *Magnetic Resonance in Medicine*, vol. 76, no. 6, pp. 1951–1956, 2016.

[41] R. Schmidt and A. G. Webb, "Improvements in RF Shimming in High Field MRI Using High Permittivity Materials With Low Order Pre-Fractal Geometries," *IEEE Transactions on Medical Imaging*, vol. 35, no. 8, pp. 1837–1844, 2016.

[42] A. J. E. Raaijmakers, O. Ipek, D. W. J. Klomp, C. Possanzini, P. R. Harvey, J. J. W. Lagendijk, and C. A. T. van den Berg, "Design of a radiative surface coil array element at 7 T: The single-side adapted dipole antenna," *Magnetic Resonance in Medicine*, vol. 66, no. 5, pp. 1488–1497, 2011.

4

DESIGN TOOL FOR DIELECTRIC PADS

The framework for designing dielectric pads was developed in the previous chapters. It enabled us to find the optimal pad for a region of interest within half a minute, instead of hours or even days. The methodology cannot be used effortlessly by the MR community, however, due to a lack of software, resources, or knowledge in this specific field. Therefore, in this chapter, a graphical design tool is developed that is easy to use and which makes it possible to find the optimum pad(s) for an arbitrary region of interest in any 3T body imaging and 7T neuroimaging application.

This chapter is submitted to Magnetic Resonance in Medicine (in press).
(DOI: 10.1002/mrm.27629, November, 2018)

4.1. INTRODUCTION

OBTAINING MR images with spatially-invariant tissue contrast becomes more challenging at higher static magnetic field strengths. The fundamental reason for this is the increase in Larmor frequency, which leads to a shortened wavelength of the RF field in tissue. For static fields strengths of 3T and higher, this wavelength becomes comparable to the dimensions of the body, or shorter. As a consequence, wave-interference effects that reduce the homogeneity and strength of the transmit RF magnetic field, referred to as the B_1^+ field become apparent [1, 2]. The homogeneity of this field is of crucial importance in obtaining a uniform contrast in MRI.

Over the last decade, many RF shimming studies have been devoted to improving the B_1^+ field distribution and efficiency. Active shimming techniques use multiple separate transmit coils: the amplitudes and phases are configured for each element individually, such that the B_1^+ field is tailored in a certain region of interest (ROI) [3–6]. Alternatively, dielectric materials can be used to tailor the B_1^+ field, as a passive shimming approach. These materials typically have a high relative permittivity on the order of 80-300, and they induce a strong secondary magnetic field in their vicinity [7–15]. These materials can be produced easily via aqueous suspensions of calcium titanate and/or barium titanate to obtain the appropriate permittivity [16–18]. Subsequently, the mixture is sealed in a polypropylene bag with appropriate dimensions to form flexible pads. Typically, these dielectric pads are placed in close vicinity to the imaging ROI tangent to the body.

Despite the ease of constructing such dielectric pads, their design is not trivial as it depends on many aspects; the optimal design varies with ROI, application requirements (e.g. transmit efficiency or homogeneity), and MR configuration (e.g. static field strength and transmit antenna). Therefore, the pads dimensions, location, and constitution need be optimized in an application-specific manner. One common approach is to perform a parametric optimization using general-purpose electromagnetic field solvers, based on a systematic trial-and-error approach and guided by user intuition, and then to choose the best pad-properties afterwards. As each of these simulations involve a large computational domain with an RF coil and heterogeneous body model, such procedures typically take multiple days for a single application [8, 19–21]. Some applications also benefit from having more than one dielectric pad, which further complicates the design procedure. This limits the exploitation of this practical shimming approach.

In previous work [22], we have developed advanced reduced order modeling techniques to accelerate pad evaluations by characterizing stationary components such as the RF coil and body model in an offline-stage, and compressing the resulting model. This yielded up to four orders of magnitude of acceleration when compared to using commercial software and enabled the automated design of a single dielectric pad in under a minute. Although these methods have been demonstrated, the offline procedures can present a challenging task for any MR user planning to use dielectric pads due to either lack of software, resources, or expertise in this specific field. The approach up to now did not allow for designing two dielectric pads at once, which can be beneficial in many applications.

In this work, we aim to extend our modeling approach to include 3T body imaging as well as 7T neuroimaging and bridge the gap between these advanced design methods and practical application by the MR community. We address this gap by integrating

the automated design procedure into a stand-alone software tool which is available for download. This tool can be run on a standard PC, is fast, and can be used to design multiple dielectric pads to optimize either the homogeneity or the efficiency of the B_1^+ field, or a combination of both, in any arbitrary ROI in the head at 7T or the body at 3T. Furthermore, for 3T, the imaging landmark can be shifted throughout the torso to enable different imaging targets to be centered in the body coil.

4.2. METHODS

CONFIGURATION

The 7T neuroimaging configuration was simulated using a shielded and tuned high-pass birdcage head coil with a radius of 15 cm operating at 298 MHz (7T). The body model "Duke" from the Virtual Family dataset was used [23], and the computational domain was discretized on a uniform and isotropic grid with a spatial resolution of 5 mm. The pad-design domain was taken as a 1 cm thick layer around the head model, which is constrained in practice by the tight-fitting receive arrays used in neuroimaging.

The 3T body-imaging configuration was simulated using a generic wide-bore high-pass birdcage body coil with a radius of 35 cm operating at 128 MHz, in which the "Duke" body model is situated. The computational domain was discretized on a uniform and isotropic grid with a spatial resolution of 7.5 mm and the pad-design domain was defined as a 1.5 cm thick layer around the torso extending from just below the top of the shoulders down to the hips. Whereas the position of the head with respect to the head coil is fixed in the 7T neuroimaging setting, this is not the case for 3T body imaging. Therefore, additional field simulations were performed for a 1.5 cm spaced range of imaging landmarks within the torso to enable shifting of the body coil for different body imaging applications.

All field quantities were normalized to 1 W input power.

MODELING DIELECTRICS

The backbone of the design tool is a modeling approach which stems from the work established in [24, 25], where an efficient forward model was presented for evaluating the effect of a dielectric pad. The basic idea is to split the computational domain into two parts as illustrated in Figure 4.1a and 4.1b for 7T neuroimaging and 3T body-imaging, respectively. The first domain is stationary and consists of the heterogeneous body model and RF transmit coil. These components remain unaffected throughout the pad-simulations and can therefore be characterized in advance. The second domain is dynamic and confines the pad-design domain where any desired dielectric pad can be positioned during the design process, i.e. with arbitrary geometry, location, and material properties. This formulation allows us to compute a pad-independent background field and field response library in an offline-stage, such that only the pad-specific secondary field needs to be computed in the online-stage. As this latter domain is much smaller than the original full computational domain, computations are accelerated without compromising accuracy.

The complexity of the calculations can be reduced further through the application of reduced order modeling techniques as has been shown in [22]. In this procedure the

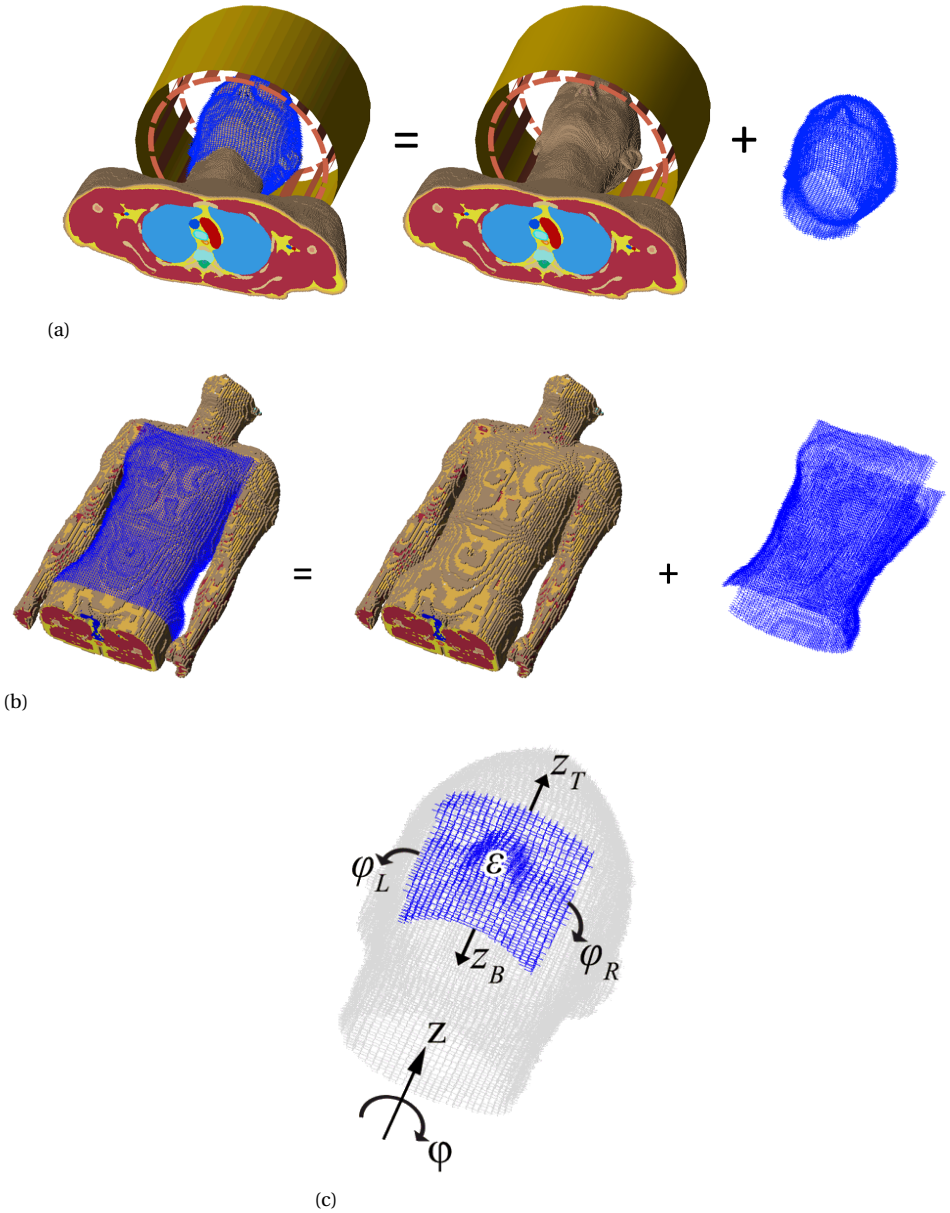

Figure 4.1: Splitting of computational domains and the parameterization of the dielectric pad. In (a) the 7T neuroimaging configuration is divided into a static part, consisting of a heterogeneous body model, RF coils, and an RF shield, and a dynamic part to which the dielectric is confined. In (b) the 3T body-imaging configuration is shown, here the wide-bore birdcage is omitted for visualization purposes of the pad design domain. As only the pads that can be easily fabricated are of interest, the model is parameterized in the pad's characteristics as is shown in (c).

practical degrees-of-freedom of the pad design problem (i.e. many fewer than allowed by the computational grid) are exploited to further compress the model. To this end, the pad design is parametrized in terms of its width, height, location, and constitution, through the parameter vector

$$\mathsf{p} = \left[z_\mathrm{B}, z_\mathrm{T}, \phi_\mathrm{L}, \phi_\mathrm{R}, \varepsilon_\mathrm{r}\right]^T,$$

as illustrated in Figure 4.1c. Subsequently, the model is compressed by projecting onto a reduced order basis obtained from randomized pad simulations, to further accelerate B_1^+ field computations to under one second of computation time for any arbitrary dielectric pad.

In the 3T configuration, each landmark position of the body coil requires specific background fields to be generated in advance. Due to the close vicinity of the pad-design domain to the body model, however, we argue that the field response library can be reused as coupling is dominated by the body model and is not significantly influenced by the body coil.

OPTIMIZATION METHODS

The pad optimization procedure can be used in two different approaches. The first approach allows the user to find the optimal position for an existing pad, i.e. the user can define the dimensions and the material properties of the pad (which they may already have prepared), and the routine optimizes the placement of this pad. The second approach forms a full parametric design which optimizes the pads dimensions, material properties, and position simultaneously by iteratively minimizing a cost functional. In both cases, we measure the characteristics of the resulting B_1^+ field within the ROI in terms of its average magnitude as a measure of transmit efficiency, and its coefficient of variation $\mathrm{C_v}$ as measure of homogeneity. The latter is defined as the ratio of standard deviation to mean value.

The first approach employs a parameter sweep over all possible positions within the pad design domain for a given pad geometry and constitution. This sweep can be carried out quite rapidly, as the simulations are fast and the number of possible solutions is rather small, in contrast to the full parametric design. Subsequently, the optimum pad positioning is found by selecting the maximum of the following objective function:

$$O(\mathsf{p}) = \gamma \mathrm{G}_\mathrm{efficiency}(\mathsf{p}) + (1-\gamma)\left[1 - \mathrm{C_v}(\mathsf{p})\right]$$

where the first term on the right hand side is the gain in average transmit efficiency ($\mathrm{G}_\mathrm{efficiency}$) due to the dielectric pad and the second term is a measure of field homogeneity. The weight γ is used to give a preference to either efficiency or homogeneity.

In the second approach, the pad optimization problem is formulated using a target field approach in which we aim to achieve a certain desired B_1^+ field magnitude in a defined ROI. This is achieved by minimizing a cost functional C as a function of the pad-parameter vector p. This functional is defined as

$$C(\mathsf{p}) = \frac{1}{2}\frac{\|\mathsf{B}_1^+(\mathsf{p}) - \mathsf{B}_1^{+;\mathrm{desired}}\|_{2;\mathrm{ROI}}^2}{\|\mathsf{B}_1^{+;\mathrm{desired}}\|_{2;\mathrm{ROI}}^2}, \tag{4.1}$$

where $\mathsf{B}_1^{+;\text{desired}}$ is the desired B_1^+ magnitude in the ROI, $\mathsf{B}_1^+(\mathsf{p})$ is the field due to a pad with model parameters p, and $\|\cdot\|_{2;\text{ROI}}^2$ denotes the ℓ_2 norm over the ROI. The cost function in Eq. (4.1) aims to minimize the discrepancy between the prescribed B_1^+ field and the B_1^+ field generated by the model, integrated over the ROI.

To minimize this nonlinear function, we use a gradient descent method combined with a line search to determine the step-size, as the gradient of the function can be computed analytically [24, 26]. Other methods can also be used, but we found that this is the most efficient and stable method in the context of this application. To ensure smooth convergence, we adopted the following rules for the update steps:

Algorithm 4.1 Update rules

For iteration j compute gradient as $\mathsf{g}^j = \nabla_{\mathsf{p}} C$
Set update direction as
$\mathsf{u}_1^j = -\text{sign}\left\{\mathsf{g}_1^j\right\} \times w_1 \times 0.75 \text{ cm}$ % z_B update
$\mathsf{u}_2^j = -\text{sign}\left\{\mathsf{g}_2^j\right\} \times \frac{1}{w_1} \times 0.75 \text{ cm}$ % z_T update
$\mathsf{u}_3^j = -\text{sign}\left\{\mathsf{g}_3^j\right\} \times w_2 \times \frac{\pi}{8} \text{ cm}$ % ϕ_L update
$\mathsf{u}_4^j = -\text{sign}\left\{\mathsf{g}_4^j\right\} \times \frac{1}{w_2} \times \frac{\pi}{8} \text{ cm}$ % ϕ_R update
$\mathsf{u}_5^j = -\text{sign}\left\{\mathsf{g}_5^j\right\} \times 20$ % ε_r update
With the weights defined as
$w_1 = \frac{|\mathsf{g}_1^j|}{|\mathsf{g}_2^j|}$ and $w_2 = \frac{|\mathsf{g}_3^j|}{|\mathsf{g}_4^j|}$
and restricted to
$\frac{1}{1.5} \le w_1 \le 1.5$ and $\frac{1}{1.5} \le w_2 \le 1.5$
Update pad parameters p as
$\mathsf{p}^{j+1} = \mathsf{p}^j + \alpha \mathsf{u}$ with an optimum step-size $0 \le \alpha \le 1$ found by line search

The weights w_1 and w_2 control the weight between related variables and serve to include gradient sensitive information in the update steps.

DESIGN TOOL

The tool is implemented in MATLAB (R2015a, The MathWorks, Inc., Natick, Massachusetts, USA). It allows for computations on a GPU when available to speed up computations and requires approximately 3 GB of working memory for 7T neuroimaging and 7 GB for 3T body imaging. When the GPU is being used, it requires approximately 0.8 GB and 2.5 GB video memory on the GPU for 7T neuroimaging and 3T body imaging, respectively. The tool is available for download as an executable file https://paddesigntool.sourceforge.io.

The graphical user interface of the design tool is shown in Figure 4.2. The top row depicts the tissue map of the head for the transverse, coronal, and sagittal slice, as well as a 3D view of the slices. If desired, the B_1^+ fields without dielectrics can be displayed here instead. The bottom row shows the B_1^+ field with pads, as well as a 3D view of the current pad design, which is updated throughout the optimization process. The contrast

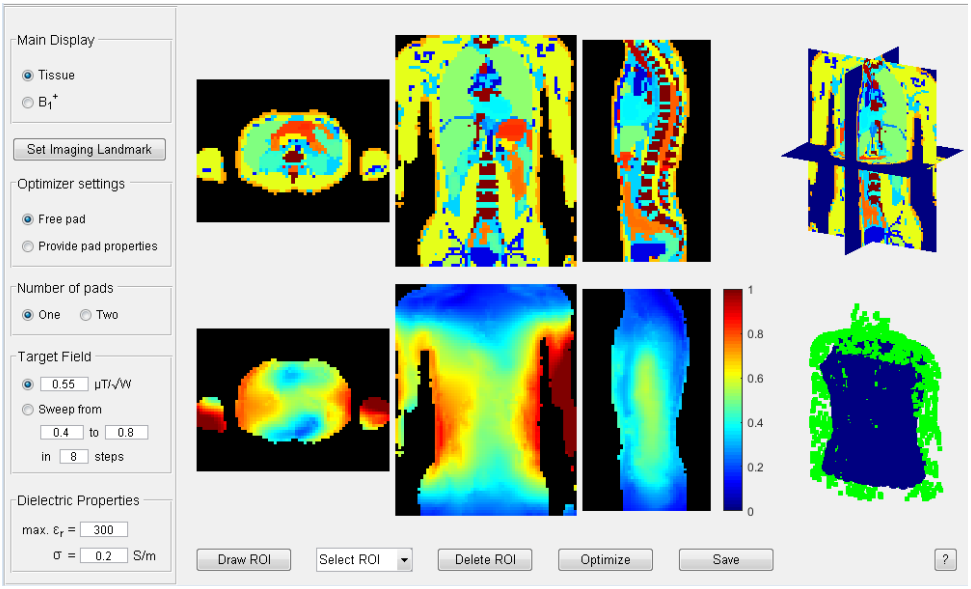

Figure 4.2: Graphical user interface of the pad design tool. Tissue profiles are shown in the top row, whereas B_1^+ fields are depicted in the bottom row. After a ROI is drawn, the user can start the optimization with the selected options.

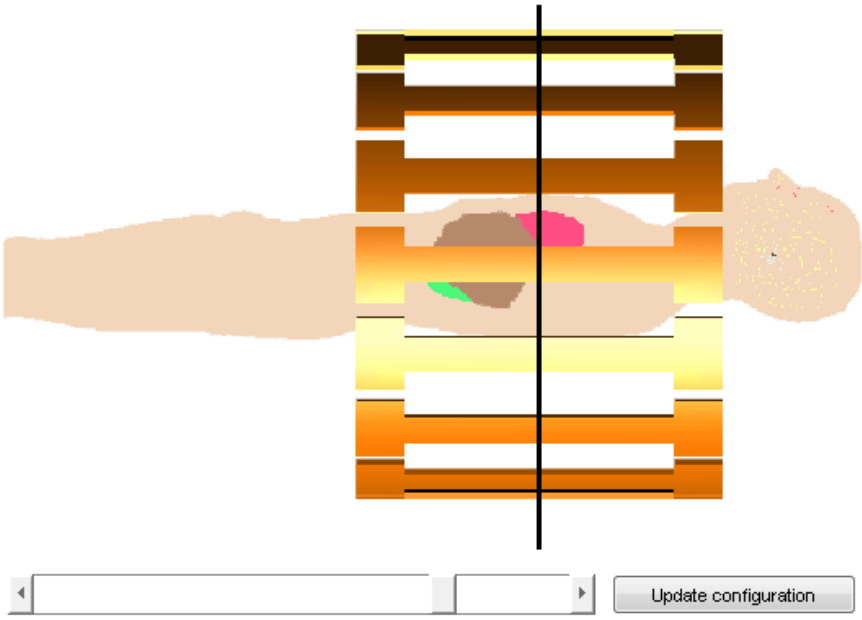

Figure 4.3: The center of the birdcage can be selected, after which the corresponding electromagnetic fields are updated.

and brightness of all displays can be manually adjusted. The imaging landmark of the 3T body coil can be shifted manually as is illustrated in Figure 4.3.

The tool allows optimization of the B_1^+ field using either one or two dielectric pads. In view of the implementation of the resulting pad design, we can limit the maximum allowed relative permittivity ε_r and incorporate a realistic conductivity throughout the iterations. Furthermore, the desired B_1^+ field efficiency for the ROI can be entered, or alternatively a sweep can be executed over a discrete set of predefined target fields to enable a trade-off analysis between transmit efficiency and homogeneity.

The user can specify a custom ROI by drawing a two-dimensional ellipsoid in each of the three isometric views. The three-dimensional ROI is then generated by their cross-section. Alternatively, for example purposes, a predefined ROI can be selected from a list. Subsequently, the optimization can be carried out, during which the design of the dielectric pad is continuously updated and illustrated in the bottom-right corner.

After the optimization is complete, the obtained results are summarized in a separate window. The results display the dimensions (width, height, and thickness) and the dielectric properties of the optimized dielectric pad. Furthermore, the resulting average transmit efficiency and coefficient of variation are listed for the scenarios with and without dielectric pad. All results can be stored for later reference.

4.3. RESULTS

For demonstration purposes, we show two application examples in which the B_1^+ field is optimized in terms of transmit efficiency and homogeneity: first in cardiac imaging at 3T using a single dielectric pad, and then in imaging the inner ear at 7T using two dielectric pads. All computations have been executed on an Intel Xeon CPU X5660 @ 2.80 GHz (dual core) equipped with a NVIDIA Tesla K40c GPU.

For the 3T example the body coil was first shifted to be centered at the heart, which was then assigned as the ROI. A sweep over a set of eight target fields was carried out using the sweep-option, which took 2 minutes to compute on the GPU or under 8 minutes on the CPU. The maximum relative permittivity was set to 300 and the electrical conductivity of the pad was fixed at 0.2 S/m. The results for this sweep are shown in Figure 4.4a and the lookup table for the individual simulations is given in Supporting Information Table S1. From the trade-off analysis we chose iteration number 5 to be the optimum, yielding a dielectric pad with dimensions $22.5 \times 35 \times 1.5$ cm^3 and a relative permittivity of 206. This design corresponded to a target field equal to 0.5271 $\frac{\mu T}{\sqrt{W}}$, and improved the transmit efficiency by 28% and reduced the C_v from 13.3% to 6.0%. The optimization results are illustrated in Figure 4.4a and the results correspond with findings from [19]. Higher efficiencies can be obtained as well, e.g. iteration number 7, but as the dimensions of the dielectric pad become larger, its implementation becomes less practical.

For the 7T inner ear example an ROI was drawn that covered both inner ears, and the B_1^+ field was optimized with two dielectric pads. The optimal pad design was found using the sweep-option in under 3 minutes on the GPU or in about 10 minutes on the CPU, which increased the transmit efficiency by 46% and reduced the C_v from 38% to 13%. The corresponding B_1^+ field and design summary are shown in Figure 4.5, which suggested one pad with dimensions $11 \times 16 \times 1$ cm^3 and a relative permittivity of 269,

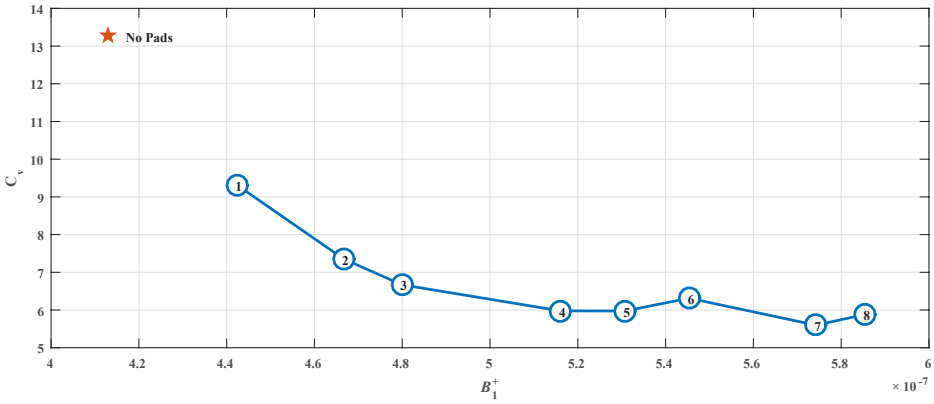

(a)

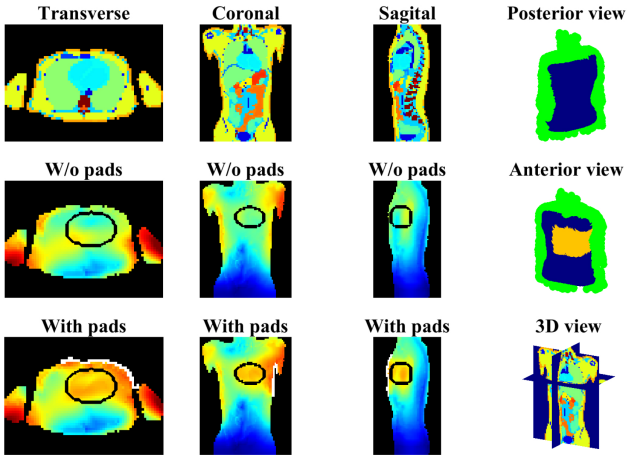

	Without pad	With pad
Transmit efficiency [T/√W]	4.1291e-07	5.3072e-07
Coeff. variation [%]	13.2666	5.9731
Height [cm]		22.4948
Azimuthal width [cm]		35.0873
Thickness [cm]		1.5000
Relative permittivity []		206.1207
Conductivity [S\m]		0.2000

(b)

Figure 4.4: Design procedure for imaging the heart at 3T. In (a) the result is shown for a parameter sweep over a predefined set of target fields, after which a desired design can be selected based on the efficiency-homogeneity plot. For the selected design (here, number 5), a single optimization is performed to obtain the results as shown in (b) for later reference. Design number 7 is not chosen here, as the dimensions of the dielectric pad are not practical. The lookup table for the individual simulations can be found in Supporting Information Table S1.

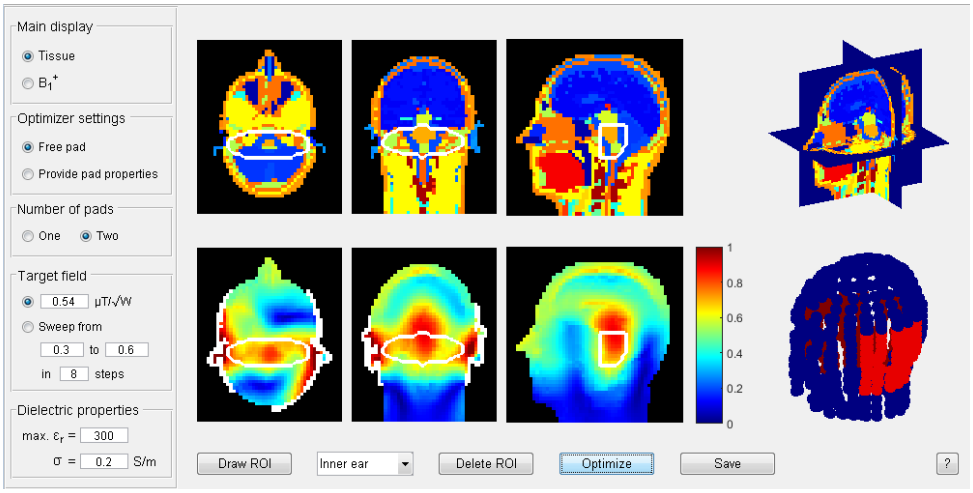

(a)

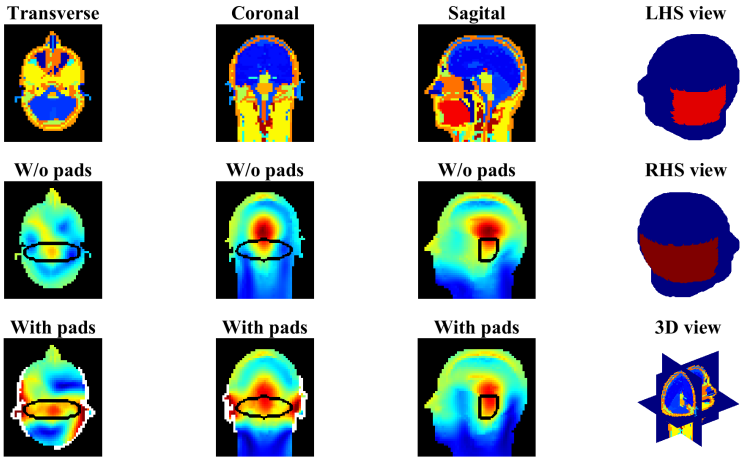

	Without pad	With pads	Pad 1	Pad 2
Transmit efficiency [μT/√W]	3.1066e-07	4.5234e-07		
Coeff. variation [%]	37.9751	12.9134		
Height [cm]			10.9941	11.9972
Azimuthal width [cm]			15.0858	21.7579
Thickness [cm]			1	1
Relative permittivity []			269.2024	299.9231
Conductivity [S\m]			0.2000	0.2000

(b)

Figure 4.5: Pad design results for the inner ear using two dielectric pads. The improved field and the location and dimension of the two dielectric pads are shown in (a). The details on the improvement and the pad's parameters can be found in (b).

Table 4.1: Lookup table for the individual optimizations of the design procedure for imaging the heart at 3T. The result is shown for a parameter sweep over a predefined set of target fields, after which a desired design can be selected based on the efficiency-homogeneity plot from Figure 4.4 and the table shown here. For all results, the pad's conductivity is 0.2 S/m and the thickness 1.5 cm.

Sweep ID	**Desired field** ($\mu T\sqrt{W}$)	**Transmit eff.** ($\mu T\sqrt{W}$)	$\mathbf{C_v}$ (%)	$\boldsymbol{\varepsilon_r}$	**Height** (cm)	**Azimuthal width** (cm)
no pad		0.413	13.4			
1	0.430	0.442	9.32	119	12.0	17.4
2	0.454	0.467	7.35	150	15.0	21.9
3	0.479	0.480	6.68	168	18.0	21.9
4	0.503	0.516	5.98	195	19.5	31.6
5	0.527	0.531	5.97	206	22.5	35.1
6	0.551	0.545	6.31	271	22.5	60.7
7	0.576	0.574	5.60	283	25.5	70.2
8	0.600	0.585	5.88	278	30.1	73.6

and a second one with dimensions $22 \times 12 \times 1$ cm^3 and a relative permittivity of 300, which agrees with previous findings [21].

4.4. DISCUSSION AND CONCLUSION

In this work we have presented a software tool that allows for designing dielectric pads for any arbitrary ROI in 3T body imaging and 7T neuroimaging applications. Computations are fast due to the underlying reduced order model, which enables MR operators to identify the optimal design and/or position in a matter of minutes. Aided by an optimization scheme, optimal design parameters can be determined which improve either the B_1^+ field magnitude or homogeneity within the ROI, or a combination of both.

The optimization method used in the tool has been chosen in view of its stability. Other methods may be considered as well, such as Gauss-Newton methods which incorporate an approximant of the Hessian in the gradient direction. In our case, the Hessian is rank deficient and hence would need to be regularized in an application-specific manner, so this approach was not pursued here. In addition, we truncated the update steps to ensure smooth convergence. Without these limitations, the algorithm had the tendency to converge to very large dielectrics with a low permittivity, which is not very practical to use. Using the truncated update steps, we avoided this undesired behavior. Alternatively, penalty terms can also be considered to discourage pad designs with large volumes or cross-sectional areas.

The reduced order model that was used for 3T body imaging was created using snapshot datasets obtained in one single birdcage landmark, centered at the liver. We showed that the same field response library can be used in other landmarks as well, without the need to compute this time-intensive part again. This exploits the fact that the electro-

magnetic interactions within the pad domain are dominated by the body, and therefore allows us to decouple the transmit coil from this response. We found that the errors that are introduced by this approximation are minimal and do not affect the solution quality. This suggests that a library may be efficiently re-used for other applications as well, e.g. in case of using a local transmit coil or transmit array. We do note that such translation still requires generating the corresponding background fields, i.e. corresponding with the body model and grid employed in the reduced order model, to ensure compatibility.

REFERENCES

[1] M. Bernstein, J. Huston, and H. Ward, "Imaging artifacts at 3.0 T," *Journal of Magnetic Resonance Imaging*, vol. 24, no. 4, pp. 735–746, 2006.

[2] Q. X. Yang, J. Wang, X. Zhang, C. M. Collins, M. B. Smith, H. Liu, X.-H. Zhu, J. T. Vaughan, K. Ugurbil, and W. Chen, "Analysis of wave behavior in lossy dielectric samples at high field," *Magnetic Resonance in Medicine*, vol. 47, no. 5, pp. 982–989, 2002.

[3] X. Wu, S. Schmitter, E. J. Auerbach, S. Moeller, K. Uurbil, and P.-F. Van de Moortele, "Simultaneous multislice multiband parallel radiofrequency excitation with independent slice-specific transmit B1 homogenization," *Magnetic Resonance in Medicine*, vol. 70, no. 3, pp. 630–638, 2013.

[4] P.-F. Van de Moortele, C. Akgun, G. Adriany, S. Moeller, J. Ritter, C. M. Collins, M. B. Smith, J. T. Vaughan, and K. Uurbil, "B1 destructive interferences and spatial phase patterns at 7 T with a head transceiver array coil," *Magnetic Resonance in Medicine*, vol. 54, no. 6, pp. 1503–1518, 2005.

[5] F. Padormo, A. Beqiri, J. V. Hajnal, and S. J. Malik, "Parallel transmission for ultrahigh-field imaging," *NMR in Biomedicine*, vol. 29, no. 9, pp. 1145–1161, 2016.

[6] U. Katscher, P. Börnert, C. Leussler, and J. S. van den Brink, "Transmit SENSE," *Magnetic Resonance in Medicine*, vol. 49, no. 1, pp. 144–150, 2003.

[7] W. M. Brink, M. J. Versluis, J. M. Peeters, P. Börnert, and A. G. Webb, "Passive radiofrequency shimming in the thighs at 3 Tesla using high permittivity materials and body coil receive uniformity correction," *Magnetic Resonance in Medicine*, vol. 76, no. 6, pp. 1951–1956, 2016.

[8] P. de Heer, W. M. Brink, B. J. Kooij, and A. G. Webb, "Increasing signal homogeneity and image quality in abdominal imaging at 3 T with very high permittivity materials," *Magnetic Resonance in Medicine*, vol. 68, no. 4, pp. 1317–1324, 2012.

[9] M. D. Lindley, D. Kim, G. Morrell, M. E. Heilbrun, P. Storey, C. J. Hanrahan, and V. S. Lee, "High-permittivity thin dielectric padding improves Fresh blood imaging of femoral arteries at 3 T," *Investigative Radiology*, vol. 50, no. 2, pp. 101–107, 2015.

[10] K. R. O'Brien, A. W. Magill, J. Delacoste, J. P. Marques, T. Kober, H. P. Fautz, F. Lazeyras, and G. Krueger, "Dielectric Pads and Low-B1+ Adiabatic Pulses: Complementary Techniques to Optimize Structural T1w Whole-Brain MP2RAGE Scans at 7 Tesla," *Journal of Magnetic Resonance Imaging*, vol. 40, no. 4, pp. 804–812, 2013.

[11] W. M. Teeuwisse, W. M. Brink, and A. G. Webb, "Quantitative assessment of the effects of high-permittivity pads in 7 Tesla MRI of the brain," *Magnetic Resonance in Medicine*, vol. 67, no. 5, pp. 1285–1293, 2012.

[12] Q. X. Yang, J. Wang, J. Wang, C. M. Collins, C. Wang, and M. B. Smith, "Reducing SAR and enhancing cerebral signal-to-noise ratio with high

permittivity padding at 3 T," *Magnetic Resonance in Medicine*, vol. 65, no. 2, pp. 358–362, 2011.

[13] G. Haemer, M. Vaidya, C. Collins, D. Sodickson, and G. Wiggins, "Evaluation of a High Permittivity Helmet for Use as a Coil Former for an 8ch Transmit/Receive Array with Dodecahedral Symmetry," in *Proceedings of the 25th Annual Scientific Meeting of the International Society for Magnetic Resonance in Medicine (ISMRM)*, Honolulu, HI, USA, 2017.

[14] M. V. Vaidya, M. Lazar, C. M. Deniz, G. G. Haemer, G. Chen, M. Bruno, D. K. Sodickson, R. Lattanzi, and C. M. Collins, "Improved detection of fMRI activation in the cerebellum at 7T with dielectric pads extending the imaging region of a commercial head coil," *Journal of Magnetic Resonance Imaging*, pp. 1–10, 2018.

[15] Q. X. Yang, S. Rupprecht, W. Luo, C. Sica, Z. Herse, J. Wang, Z. Cao, J. Vesek, M. T. Lanagan, G. Carluccio, Y.-C. Ryu, and C. M. Collins, "Radiofrequency field enhancement with high dielectric constant (HDC) pads in a receive array coil at 3.0T," *Journal of Magnetic Resonance Imaging*, vol. 38, no. 2, pp. 435–440, 2013.

[16] K. Haines, N. Smith, and A. Webb, "New high dielectric constant materials for tailoring the B1+ distribution at high magnetic fields," *Journal of Magnetic Resonance*, vol. 203, no. 2, pp. 323–327, 2010.

[17] W. M. Teeuwisse, W. M. Brink, K. N. Haines, and A. G. Webb, "Simulations of high permittivity materials for 7 T neuroimaging and evaluation of a new barium titanate-based dielectric," *Magnetic Resonance in Medicine*, vol. 67, no. 4, pp. 912–918, 2012.

[18] T. O'Reilly, A. Webb, and W. Brink, "Practical improvements in the design of high permittivity pads for dielectric shimming in neuroimaging at 7 T," *Journal of Magnetic Resonance*, vol. 270, pp. 108–114, 2016.

[19] W. M. Brink and A. G. Webb, "High permittivity pads reduce specific absorption rate, improve B 1 homogeneity, and increase contrast-to-noise ratio for functional cardiac MRI at 3 T," *Magnetic Resonance in Medicine*, vol. 71, no. 4, pp. 1632–1640, 2014.

[20] S. A. Winkler and B. K. Rutt, "Practical methods for improving B1+ homogeneity in 3 tesla breast imaging," *Journal of Magnetic Resonance Imaging*, vol. 41, no. 4, pp. 992–999, 2015.

[21] W. M. Brink, A. M. van der Jagt, M. J. Versluis, B. M. Verbist, and A. G. Webb, "High Permittivity Dielectric Pads Improve High Spatial Resolution Magnetic Resonance Imaging of the Inner Ear at 7 T," *Investigative Radiology*, vol. 49, no. 5, pp. 271–277, 2014.

[22] J. H. F. van Gemert, W. M. Brink, A. G. Webb, and R. F. Remis, "High-Permittivity Pad Design for Dielectric Shimming in Magnetic Resonance Imaging Using Projection-Based Model Reduction and a Nonlinear Optimization Scheme," *IEEE Transactions on Medical Imaging*, vol. 37, no. 4, pp. 1035–1044, 2018.

[23] A. Christ, W. Kainz, E. G. Hahn, K. Honegger, M. Zefferer, E. Neufeld, W. Rascher, R. Janka, W. Bautz, J. Chen, B. Kiefer, P. Schmitt, H.-P. Hollenbach, J. Shen, M. Oberle,

D. Szczerba, A. Kam, J. W. Guag, and N. Kuster, "The Virtual Familydevelopment of surface-based anatomical models of two adults and two children for dosimetric simulations," *Physics in Medicine and Biology*, vol. 55, no. 2, pp. N23–N38, 2010.

[24] J. H. F. Van Gemert, W. Brink, A. Webb, and R. Remis, "An Efficient Methodology for the Analysis of Dielectric Shimming Materials in Magnetic Resonance Imaging," *IEEE Transactions on Medical Imaging*, vol. 36, no. 2, pp. 666–673, 2017.

[25] W. M. Brink, R. F. Remis, and A. G. Webb, "A theoretical approach based on electromagnetic scattering for analysing dielectric shimming in high-field MRI," *Magnetic Resonance in Medicine*, vol. 75, no. 5, pp. 2185–2194, 2016.

[26] J. Nocedal and S. J. Wright, *Numerical optimization*, 2nd ed. Springer, 2006.

II

PART TWO
ACCELERATING RECONSTRUCTIONS

5

PRECONDITIONER FOR PI AND CS RECONSTRUCTIONS

In Part I of this thesis we described how to improve the image quality of MR scans by tailoring the B_1^+ field using dielectric pads. In this chapter, we focus on the reconstruction part of MR imaging when parallel imaging (PI) and compressed sensing (CS) techniques are used to accelerate the acquisition times. Processing the data becomes more difficult due to the increased problem complexity which leads to longer reconstruction times. Hence, this chapter describes the design and implementation of an efficient preconditioner for accelerating PI and CS reconstructions in a Split Bregman framework.

This chapter has been published in Magnetic Resonance in Medicine.
(Volume: 81, Issue: 1, 2019)

INTRODUCTION

THE undersampling factor in Parallel Imaging (PI) is in theory limited by the number of coil channels [1–4]. Higher factors can be achieved by using Compressed Sensing (CS) which estimates missing information by adding a priori information [5, 6]. The a priori knowledge relies on the sparsity of the image in a certain transform domain. It is possible to combine PI and CS, e.g. [7] and [8], achieving almost an order of magnitude speed-up factors in cardiac perfusion MRI and enabling free-breathing MRI of the liver [9].

CS allows reconstruction of an estimate of the true image even in the case of considerable undersampling factors, for which the data model generally describes an ill-posed problem without a unique solution. This implies that the true image cannot be found by directly applying Fourier transforms. Instead, regularization is used to solve the ill-posed problem by putting additional constraints on the solution. For CS, such a constraint enforces sparsity of the image in a certain domain, which is promoted by the ℓ_0-norm [6, 10, 11]. However, practically the ℓ_1-norm is used instead as it is the closest representation that is numerically feasible to implement. The wavelet transform and derivative operators, integrated in total variation regularization, are examples of sparsifying transforms that can be used in the spatial direction [8, 12–16] and temporal dimension [9], respectively.

Although CS has led to a considerable reduction in acquisition times either in parallel imaging applications or in single coil acquisitions, the benefit of the ℓ_1-norm regularization constraint comes with the additional burden of increased reconstruction times, because ℓ_1-norm minimization problems are in general difficult to solve. Many methods have been proposed that solve the problem iteratively [12, 14, 17–23]. In this work, we focus on the Split Bregman (SB) approach because of its computational performance, and its well-established track record [14, 24–28]. SB transforms the initial minimization problem, containing both ℓ_1 and ℓ_2-norm terms, into a set of subproblems that either require solving an ℓ_2-norm or an ℓ_1-norm minimization problem, each of which can be approached using standard methods.

The most expensive step in SB, which is also present in many other methods, is to solve an ℓ_2-norm minimization problem, which can be formulated as a linear least squares problem, e.g. [29]. The system matrix of the least squares problem remains constant throughout the SB iterations and this feature has shown to be convenient for finding an approximation of the inverse system matrix as is done in e.g. [30]. This approach eliminates the need for an iterative scheme to solve the ℓ_2-norm minimization problem, but for large problem sizes the initial computational costs are high, making it less profitable in practice. An alternative approach for eliminating the iterative scheme to solve the ℓ_2-norm minimization problem was demonstrated in [31]. In this approach, extra variable splitting is introduced to separate the coil sensitivity matrices from the Fourier transforms, such that all individual subproblems can be solved directly in the case of Cartesian sampling. This can lead to a considerable reduction in reconstruction time, provided that the reconstruction parameters are optimized. Simulations and in vivo experiments showed significant improvements in convergence compared to nonlinear conjugate gradient and a monotone fast iterative shrinkage-thresholding algorithms. The extra variable splitting introduces penalty parameters, however, and unsta-

ble behavior can occur for certain parameter choices due to nontrivial null-spaces of the operators [31–33]. This can be seen as a drawback of this approach. Furthermore, determining the extra parameters is obviously nonunique. Considering the fact that each image slice would be reconstructed optimally with possibly different reconstruction parameters, we prefer the more straightforward SB scheme. Moreover, for non-Cartesian trajectories, direct solutions are no longer possible and iterative schemes are needed.

Alternatively, to keep the number of reconstruction parameters to a minimum and to minimize possible stability issues, preconditioners can be used to reduce the number of iterations required for solving the least squares problem [34]. The incomplete Cholesky factorization and hierarchically-structured matrices are examples of preconditioners that reduce the number of iterations drastically in many applications [35, 36]. The drawback of these type of preconditioners is that the full system matrix needs to be built before the reconstruction starts, which for larger problem sizes can only be done on a very powerful computer due to memory limitations. Although in [37–39] a pentadiagonal matrix was constructed as a preconditioner, solving such a system is still relatively expensive. In addition, before constructing the preconditioner, patient-specific coil sensitivity profiles need to be measured, which often leads to large initialization times. In [31, 40], the extra variable splitting enables building a preconditioner independent of coil sensitivity maps, resulting in a preconditioner for non-Cartesian reconstructions, but one that is not applicable for the more stable SB scheme.

In this work, we design a Fourier transform-based preconditioner for PI-CS reconstructions and Cartesian trajectories in a stable SB framework, that takes the coil sensitivities on a patient-specific basis into account, has negligible initialization time and which is highly scalable to a large number of unknowns, as often encountered in MRI.

THEORY

In this section we first describe the general parallel imaging and compressed sensing problems. Subsequently, the Split Bregman algorithm, which is used to solve these problems, is discussed. Hereafter, we introduce the preconditioner that is used to speed up the PI-CS algorithm and elaborate on its implementation and complexity.

PARALLEL IMAGING RECONSTRUCTION

In parallel imaging with full k-space sampling the data, including noise, is described by the model

$$\mathsf{F}\mathsf{S}_i\mathbf{x} = \mathbf{y}_{\text{full},i} \qquad \text{for } i = 1,...,\mathrm{N_c}$$

where the $\mathbf{y}_{\text{full},i} \in \mathbb{C}^{N\times 1}$ are the fully sampled k-space data sets containing noise for $i \in \{1,..,\mathrm{N_c}\}$, with $\mathrm{N_c}$ the number of coil channels, and $\mathbf{x} \in \mathbb{C}^{N\times 1}$ is the true image [3]. Here, $N = m \cdot n$, where m and n define the image matrix size in the x and y-directions, respectively, for a 2D sampling case. Furthermore, $\mathsf{S}_i \in \mathbb{C}^{N\times N}$ are diagonal matrices representing complex coil sensitivity maps for each channel. Finally, $\mathsf{F} \in \mathbb{C}^{N\times N}$ is the discrete two-dimensional Fourier transform matrix. In the case of undersampling, the data is described by the model

$$\mathsf{R}\mathsf{F}\mathsf{S}_i\mathbf{x} = \mathbf{y}_i \qquad \text{for } i = 1,...,\mathrm{N_c}, \tag{5.1}$$

where $\mathbf{y}_i \in \mathbb{C}^{N\times 1}$ are the undersampled k-space data sets for $i \in \{1,..,\mathrm{N_c}\}$ with zeros at non-measured k-space locations. The undersampling pattern is specified by the binary diagonal sampling matrix $\mathsf{R} \in \mathbb{R}^{N\times N}$, so that the undersampled Fourier transform is given by RF. Here it is important to note that R reduces the rank of RFS_i, which means that solving for $\mathbf{x}$ in Eq. (5.1) is in general an ill-posed problem for each coil and a unique solution does not exist. However, if the individual coil data sets are combined and the undersampling factor does not exceed the number of coil channels, the image $\mathbf{x}$ can in theory be reconstructed by finding the least squares solution, i.e. by minimizing

$$\hat{\mathbf{x}} = \underset{\mathbf{x}}{\operatorname{argmin}} \left\{ \sum_{i=1}^{\mathrm{N_c}} \left\| \mathsf{RFS}_i \mathbf{x} - \mathbf{y}_i \right\|_2^2 \right\}, \tag{5.2}$$

where $\hat{\mathbf{x}} \in \mathbb{C}^{N\times 1}$ is an estimate of the true image.

PARALLEL IMAGING RECONSTRUCTION WITH COMPRESSED SENSING

In the case of higher undersampling factors, the problem of solving Eq. (5.2) becomes ill-posed and additional regularization terms need to be introduced to transform the problem into a well-posed problem. Since MR images are known to be sparse in some domains, adding ℓ_1-norm terms is a suitable choice for regularization. The techniques of parallel imaging and compressed sensing are then combined in the following minimization problem

$$\hat{\mathbf{x}} = \underset{\mathbf{x}}{\operatorname{argmin}} \left\{ \frac{\mu}{2} \sum_{i=1}^{\mathrm{N_c}} \left\| \mathsf{RFS}_i \mathbf{x} - \mathbf{y}_i \right\|_2^2 + \frac{\lambda}{2} \left(\|\mathsf{D}_x \mathbf{x}\|_1 + \left\|\mathsf{D}_y \mathbf{x}\right\|_1 \right) + \frac{\gamma}{2} \|\mathsf{W}\mathbf{x}\|_1 \right\}, \tag{5.3}$$

with μ, λ and γ the regularization parameters for the data fidelity, the total variation, and the wavelet, respectively [8]. A total variation regularization constraint is introduced by the first-order derivative matrices D_x, $\mathsf{D}_y \in \mathbb{R}^{N\times N}$, representing the numerical finite difference scheme

$$\begin{aligned} D_x(x)|_{i,j} &= x_{i,j} - x_{i-1,j} && i = 2,..,m, \quad j = 1,..,n \\ D_y(x)\big|_{i,j} &= x_{i,j} - x_{i,j-1} && i = 1,..,m, \quad j = 2,..,n \end{aligned}$$

with periodic boundary conditions

$$\begin{aligned} D_x(x)|_{1,j} &= x_{1,j} - x_{m,j} && j = 1,..,n \\ D_y(x)\big|_{i,1} &= x_{i,1} - x_{i,n} && i = 1,..,m \end{aligned}$$

so that D_x and D_y are circulant. A unitary wavelet transform $\mathsf{W} \in \mathbb{R}^{N\times N}$ further promotes sparsity of the image in the wavelet domain.

SPLIT BREGMAN ITERATIONS

Solving Eq. (5.3) is not straightforward as the partial derivatives of the ℓ_1-norm terms are not well-defined around 0. Instead, the problem is transformed into one that can be solved easily. In this work, we use Split Bregman to convert Eq. (5.3) into multiple minimization problems in which the ℓ_1-norm terms have been decoupled from the ℓ_2-norm

term, as discussed in detail in [14, 24]. For convenience, the Split Bregman method is shown in Algorithm 5.1. The Bregman parameters $\mathbf{b}_x, \mathbf{b}_y, \mathbf{b}_w$ are introduced by the Bregman scheme and auxiliary variables $\mathbf{d}_x, \mathbf{d}_y, \mathbf{d}_w$ are introduced by writing the constrained problem as an unconstrained problem. The algorithm consists of two loops: an outer loop and an inner loop. In the inner loop (steps 4-11), we first compute the vector $\mathbf{b}$ that serves as a right-hand side in the system of equations of step 5. Subsequently, the ℓ_1-norm subproblems are solved using the shrink function in steps 6-8. Hereafter, the residuals for the regularization terms are computed in steps 9-11 and are subsequently fed back into the system by updating the right hand side vector $\mathbf{b}$ in step 5. Steps 4-11 can be repeated several times, but one or two inner iterations are normally sufficient for convergence. Similarly, the outer loop feeds the residual encountered in the data fidelity term back into the system, after which the inner loop is executed again.

The system of linear equations,

$$\mathsf{A}\hat{\mathbf{x}} = \mathbf{b}, \tag{5.4}$$

in line 5 of the algorithm follows from a standard least squares problem, where the system matrix is given by

$$\mathsf{A} = \mu \sum_{i=1}^{\mathrm{N_c}} (\mathsf{RFS}_i)^H \mathsf{RFS}_i + \lambda \left(\mathsf{D}_x^H \mathsf{D}_x + \mathsf{D}_y^H \mathsf{D}_y \right) + \gamma \mathsf{W}^H \mathsf{W}$$

with right-hand side

$$\mathbf{b} = \mu \sum_{i=1}^{\mathrm{N_c}} (\mathsf{RFS}_i)^H \mathbf{y}_i + \lambda \left[\mathsf{D}_x^H \left(\mathbf{d}_x^k - \mathbf{b}_x^k \right) + \mathsf{D}_y^H \left(\mathbf{d}_y^k - \mathbf{b}_y^k \right) \right] + \gamma \mathsf{W}^H \left(\mathbf{d}_w^k - \mathbf{b}_w^k \right).$$

In this work we focus on solving Eq. (5.4), which is computationally the most expensive part of Algorithm 5.1. It is important to note that the system matrix A remains constant throughout the algorithm and only the right hand side vector $\mathbf{b}$ changes, which allows us to efficiently solve Eq. (5.4) by using preconditioning techniques.

STRUCTURE OF THE SYSTEM MATRIX A

The orthogonal wavelet transform is unitary, so that $\mathsf{W}^H\mathsf{W} = \mathsf{I}$. Furthermore, the derivative operators are constructed such that the matrices $\mathsf{D}_x, \mathsf{D}_y, \mathsf{D}_x^H$ and D_y^H are block circulant with circulant blocks (BCCB). The product and sum of two BCCB matrices is again BCCB, showing that $\mathsf{D}_x^H\mathsf{D}_x + \mathsf{D}_y^H\mathsf{D}_y$ is also BCCB. These type of matrices are diagonalized by the two-dimensional Fourier transformation, i.e.

$$\mathsf{D}_1 = \mathsf{FCF}^H \quad \text{or} \quad \mathsf{D}_2 = \mathsf{F}^H\mathsf{CF}$$

where C is a BCCB matrix and D_1 and D_2 are diagonal matrices. This motivates us to write the system matrix A in Eq. (5.4) in the form

$$\begin{aligned} \mathsf{A} &= \mathsf{F}^H\mathsf{FAF}^H\mathsf{F} \\ &= \mathsf{F}^H\mathsf{KF} \end{aligned}$$

with $\mathsf{K} \in \mathbb{C}^{N \times N}$ given by

$$\mathsf{K} = \underbrace{\mu \sum_{i=1}^{\mathrm{N_c}} \mathsf{F}\mathsf{S}_i^H \mathsf{F}^H \mathsf{R}^H \mathsf{R} \mathsf{F} \mathsf{S}_i \mathsf{F}^H}_{\mathsf{K}_c} + \underbrace{\lambda \mathsf{F} \left(\mathsf{D}_x^H \mathsf{D}_x + \mathsf{D}_y^H \mathsf{D}_y \right) \mathsf{F}^H}_{\mathsf{K}_d} + \underbrace{\gamma \quad \mathsf{I}}_{\mathsf{K}_w} . \tag{5.5}$$

The term $\mathsf{D}_x^H \mathsf{D}_x + \mathsf{D}_y^H \mathsf{D}_y$ is BCCB, so that K_d in K becomes diagonal. If there is no sensitivity encoding, that is $\mathsf{S}_i = \mathsf{I}\ \forall i \in \{1, .., \mathrm{N_c}\}$, the entire K matrix becomes diagonal in which case the solution $\hat{\mathbf{x}}$ can be efficiently found by computing

$$\hat{\mathbf{x}} = \mathsf{A}^{-1}\mathbf{b} = \mathsf{F}^H \mathsf{K}^{-1} \mathsf{F} \mathbf{b}$$

for invertible K. In practice, Fast Fourier Transforms (FFTs) are used for this step. With sensitivity encoding, $\mathsf{S}_i \neq \mathsf{I}$ and $\mathsf{S}_i^H \mathsf{F}^H \mathsf{R}^H \mathsf{R} \mathsf{F} \mathsf{S}_i$ is not BCCB for any i, hence matrix K is not diagonal. In that case we prefer to solve Eq. (5.4) iteratively, since finding K^{-1} is now computationally too expensive. It can be observed that the system matrix A is Hermitian and positive definite, which motivates the choice for the conjugate gradient (CG) method as an iterative solver.

5

PRECONDITIONING

A preconditioner $\mathsf{M} \in \mathbb{C}^{N \times N}$ can be used to reduce the number of iterations required for CG convergence [41]. It should satisfy the conditions

Algorithm 5.1 Split Bregman Iteration

Initialize $\mathbf{y}_i^{[1]} = \mathbf{y}_i$ for $i = 1, ..., \mathrm{N_c}$, $\mathbf{x}^{[1]} =$ Sum of Squares$(\mathsf{F}^H \mathbf{y}_i, i = 1, ..., \mathrm{N_c})$,
Initialize $\mathbf{b}_x^{[1]}, \mathbf{b}_y^{[1]}, \mathbf{b}_w^{[1]}, \mathbf{d}_x^{[1]}, \mathbf{d}_y^{[1]}, \mathbf{d}_w^{[1]} = \mathbf{0}$
for $j = 1$ to nOuter **do**
  for $k = 1$ to nInner **do**
    $\mathbf{b} = \mu \sum_{i=1}^{\mathrm{N_c}} \mathsf{S}_i^H \mathsf{F}^H \mathsf{R}^H \mathbf{y}_i^{[j]} + \lambda \left[\mathsf{D}_x^H (\mathbf{d}_x^{[k]} - \mathbf{b}_x^{[k]}) + \mathsf{D}_y^H (\mathbf{d}_y^{[k]} - \mathbf{b}_y^{[k]}) \right] +$
    $\gamma \mathsf{W}^H (\mathbf{d}_w^{[k]} - \mathbf{b}_w^{[k]})$
    solve $\mathsf{A}\mathbf{x}^{[k+1]} = \mathbf{b}$ with $\mathbf{x}^{[k]}$ as initial guess
    $\mathbf{d}_x^{[k+1]} = \mathrm{shrink}\left(\mathsf{D}_x \mathbf{x}^{[k+1]} + \mathbf{b}_x^{[k]}, \frac{1}{\lambda} \right)$
    $\mathbf{d}_y^{[k+1]} = \mathrm{shrink}\left(\mathsf{D}_y \mathbf{x}^{[k+1]} + \mathbf{b}_y^{[k]}, \frac{1}{\lambda} \right)$
    $\mathbf{d}_w^{[k+1]} = \mathrm{shrink}\left(\mathsf{W} \mathbf{x}^{[k+1]} + \mathbf{b}_w^{[k]}, \frac{1}{\gamma} \right)$
    $\mathbf{b}_x^{[k+1]} = \mathbf{b}_x^{[k]} + \mathsf{D}_x \mathbf{x}^{[k+1]} - \mathbf{d}_x^{[k+1]}$
    $\mathbf{b}_y^{[k+1]} = \mathbf{b}_y^{[k]} + \mathsf{D}_y \mathbf{x}^{[k+1]} - \mathbf{d}_y^{[k+1]}$
    $\mathbf{b}_w^{[k+1]} = \mathbf{b}_w^{[k]} + \mathsf{W} \mathbf{x}^{[k+1]} - \mathbf{d}_w^{[k+1]}$
  end for
  for $i = 1$ to $\mathrm{N_c}$ **do**
    $\mathbf{y}_i^{[j+1]} = \mathbf{y}_i^{[j]} + \mathbf{y}_i^{[1]} - \mathsf{R}\mathsf{F}\mathsf{S}_i \mathbf{x}^{[k+1]}$
  end for
end for

1. $\mathsf{M}^{-1}\mathsf{A} \approx \mathsf{I}$ to cluster the eigenvalues of the matrix pair around 1, and

2. determination of M^{-1} and its evaluation on a vector should be computationally cheap.

Ideally, we would like to use a diagonal matrix as the preconditioner as this is computationally inexpensive. For this reason, the Jacobi preconditioner is used in many applications with the diagonal elements from matrix A as the input. However, for the current application of PI and CS the Jacobi preconditioner is not efficient since it does not provide an accurate approximate inverse of the system matrix A. In this work, we use a different approach and approximate the diagonal from K in Eq. (5.5) instead. The motivation behind this approach is that the Fourier matrices in matrix K center a large part of the information contained in $\mathsf{S}_i^H\mathsf{F}^H\mathsf{R}^H\mathsf{R}\mathsf{F}\mathsf{S}_i$ around the main diagonal of K, so that neglecting off-diagonal elements of K has less effect than neglecting off-diagonal elements of A.

For the preconditioner used in this work we approximate A^{-1} by

$$\mathsf{M}^{-1} = \mathsf{F}^H \text{diag}\{\mathbf{k}\}^{-1}\mathsf{F}, \tag{5.6}$$

where diag{} places the elements of its argument on the diagonal of a matrix. Furthermore, vector $\mathbf{k}$ is the diagonal of matrix K and can be written as

$$\mathbf{k} = \mu\mathbf{k}_c + \lambda\mathbf{k}_d + \gamma\mathbf{k}_w, \tag{5.7}$$

where $\mathbf{k}_c$, $\mathbf{k}_d$ and $\mathbf{k}_w$ are the diagonals of K_c, K_d and K_w, respectively. Note that K_d and K_w are diagonal matrices already, so that only $\mathbf{k}_c$ will result in an approximation of the inverse for the final system matrix A.

EFFICIENT IMPLEMENTATION OF THE PRECONDITIONER

The diagonal elements $\mathbf{k}_{c;i}$ of $\mathsf{K}_{c;i} = \underbrace{\mathsf{F}\mathsf{S}_i^H\mathsf{F}^H}_{\mathsf{C}_i^H}\underbrace{\mathsf{R}^H\mathsf{R}}_{\mathsf{R}}\underbrace{\mathsf{F}\mathsf{S}_i\mathsf{F}^H}_{\mathsf{C}_i}$ for a certain i are found by noting that $\mathsf{C}_i = \mathsf{F}\mathsf{S}_i\mathsf{F}^H$ is in fact a BCCB matrix. The diagonal elements $\mathbf{k}_{c;i}$ of $\mathsf{K}_{c;i}$ can now be found on the diagonal of $\mathsf{C}_i^H\mathsf{R}\mathsf{C}_i$, so that

$$\mathbf{k}_{c;i} = \sum_{j=1}^{N} \mathbf{e}_j \left(\mathbf{c}_{j;i}^H \mathsf{R}\mathbf{c}_{j;i}\right),$$

with $\mathbf{c}_{j;i}^H$ being the j^{th} row of matrix C_i^H and $\mathbf{e}_j$ the j^{th} standard basis vector. Note that the scalar $\left(\mathbf{c}_{j;i}^H \mathsf{R}\mathbf{c}_{j;i}\right)$ is the j^{th} entry of vector $\mathbf{k}_{c;i}$. Since R is a diagonal matrix which can

be written as $\mathsf{R} = \text{diag}\{\mathbf{r}\}$, we can also write

$$\begin{aligned}\mathbf{k}_{c;i} &= \sum_{j=1}^{N} \mathbf{e}_j \left(\mathbf{c}_{j;i}^H \circ \mathbf{c}_{j;i}^T\right)\mathbf{r} \\ &= \begin{bmatrix} \mathbf{c}_{1;i}^H \circ \mathbf{c}_{1;i}^T \\ \mathbf{c}_{2;i}^H \circ \mathbf{c}_{2;i}^T \\ \vdots \\ \mathbf{c}_{N;i}^H \circ \mathbf{c}_{N;i}^T \end{bmatrix} \mathbf{r} \\ &= \left(\mathsf{C}_i^H \circ \mathsf{C}_i^T\right)\mathbf{r}, \end{aligned} \tag{5.8}$$

where $\circ$ denotes the element-wise (Hadamard) product. Since the element-wise product of two BCCB matrices is again a BCCB matrix, the circular convolution theorem tells us [42, 43] that

$$\mathsf{F}\mathbf{k}_{c;i} = \mathsf{F}\left[\left(\mathbf{c}_{1;i}^H \circ \mathbf{c}_{1;i}^T\right)^T * \mathbf{r}\right] = \mathsf{F}\left[\left(\mathbf{c}_{1;i}^H \circ \mathbf{c}_{1;i}^T\right)^T\right] \circ \mathsf{F}\mathbf{r}.$$

5

The resulting matrix vector product in Eq. (5.8) can now be efficiently computed as

$$\mathbf{k}_{c;i} = \mathsf{F}^H \left\{ \left[\mathsf{F}\left(\mathbf{c}_{1;i}^H \circ \mathbf{c}_{1;i}^T\right)^T\right] \circ \mathsf{F}\mathbf{r} \right\}. \tag{5.9}$$

Finally, the diagonal elements $\mathbf{d}$ of the diagonal matrix D with structure $\mathsf{D} = \mathsf{F}\mathsf{C}\mathsf{F}^H$ can be computed efficiently by using $\mathbf{d} = \mathsf{F}\mathbf{c}_1$, where $\mathbf{c}_1$ is the first row of C. Therefore, the first row $\mathbf{c}_{1;i}^H$ of matrix C_i^H is found as $\left(\mathbf{c}_{1;i}^H\right)^T = \mathsf{F}^H\left(\mathbf{s}_i^H\right)^T$, with $\mathbf{s}_i^H$ a row vector containing the diagonal elements of matrix S_i. For multiple coils Eq. (5.9) becomes

$$\mathbf{k}_c = \mathsf{F}^H \left\{ \left[\mathsf{F}\sum_{i=1}^{\mathrm{N_c}} \left(\mathbf{c}_{1;i}^H \circ \mathbf{c}_{1;i}^T\right)^T\right] \circ \mathsf{F}\mathbf{r} \right\}, \tag{5.10}$$

where the action of the Fourier matrix on a vector can be efficiently computed using the FFT. Since $\mathsf{D}_x^H\mathsf{D}_x + \mathsf{D}_y^H\mathsf{D}_y$ is BCCB, the elements of $\mathbf{k}_d$ can be quickly found by evaluating $\mathbf{k}_d = \mathsf{F}\mathbf{t}_1$, where $\mathbf{t}_1$ is the first row of $\mathsf{D}_x^H\mathsf{D}_x + \mathsf{D}_y^H\mathsf{D}_y$. Finally, the elements of $\mathbf{k}_w$ are all equal to one, since K_ω is the identity matrix.

COMPLEXITY

For every inner-iteration of the Split Bregman algorithm we need to solve the linear system given in Eq. (5.4), which is done iteratively using a Preconditioned Conjugate Gradient method (PCG). In this method, the preconditioner constructed above is used as a left preconditioner by solving the following system of equations:

$$\mathsf{M}^{-1}\mathsf{A}\hat{\mathbf{x}} = \mathsf{M}^{-1}\mathbf{b}, \tag{5.11}$$

where $\hat{\mathbf{x}}$ is the approximate solution constructed by the PCG algorithm. In PCG this implies that for every iteration the preconditioner should be applied once on the residual vector $\mathbf{r} = \mathsf{A}\hat{\mathbf{x}} - \mathbf{b}$. The preconditioner M can be constructed beforehand since

Table 5.1: FLOPs required for construction of M^{-1} and for evaluation of A on a vector

	Operation	FLOPs
Construction of M^{-1}	$\left(\mathbf{c}_i^H\right)^T = \mathsf{F}^H\left(\mathbf{s}_i^H\right)^T \ \forall i \in \{1,..,\mathrm{N_c}\}$,	$\mathrm{N_c} N \log N$
	$\sum_i^{\mathrm{N_c}} \left(\mathbf{c}_{1;i}^H \circ \mathbf{c}_{1;i}^T\right)^T$	$2\mathrm{N_c} N - N$
	$\mathsf{F}^H[\mathsf{F}(\ldots) \circ \mathsf{F}(\ldots)]$	$N + 3N \log N$
	$\mathbf{k}_d = \mathsf{F}^H \mathbf{t}_1$	$N \log N$
	$\mathbf{k} = \mathbf{k}_c + \mathbf{k}_d + \mathbf{k}_w$	$2N$
	$\mathbf{k}^{-1}$	N
	Total	$(3 + 2\mathrm{N_c})N + (4 + \mathrm{N_c})N \log N$
Evaluation A on vector	$\sum_{i=1}^{\mathrm{N_c}} (\mathsf{RFS}_i)^H \mathsf{RFS}_i$	$\mathrm{N_c}(3N + 2N \log N) + \mathrm{N_c} N - N$
	$\mathsf{D}_x^H \mathsf{D}_x + \mathsf{D}_y^H \mathsf{D}_y$	$5N$
	$\mathsf{W}^H \mathsf{W}$	0
	Summation of the three terms above	$2N$
	Total	$(6 + 4\mathrm{N_c})N + 2\mathrm{N_c} N \log N$

it remains fixed for the entire Split Bregman algorithm as the regularization parameters μ, λ, and γ are constant. As can be seen in Table 5.1, M^{-1} is constructed in $(3 + 2\mathrm{N_c})N + (4 + \mathrm{N_c})N \log N$ FLOPs. Evaluation of the diagonal preconditioner M^{-1} from Eq. (5.6) on a vector amounts to two Fourier transforms and a single multiplication, and therefore requires $N + 2N \log N$ FLOPs.

To put this into perspective, evaluation of matrix A on a vector requires $(6 + 4\mathrm{N_c})N + 2\mathrm{N_c} N \log N$ FLOPs, as shown in Table 5.1. The upper bound on the additional costs per iteration relative to the costs for evaluating A on a vector is therefore

$$\lim_{N \to \infty} \frac{N + 2N \log N}{(6 + 4\mathrm{N_c})N + 2\mathrm{N_c} N \log N} = \frac{1}{\mathrm{N_c}},$$

showing that the preconditioner evaluation step becomes relatively cheaper for an increasing number of coil elements. The scaling of the complexity with respect to the problem size is depicted in Fig. 5.1 for a fixed number of coils $\mathrm{N_c} = 12$.

METHODS

MR DATA ACQUISITION

Experiments were performed on healthy volunteer after giving informed consent. The Leiden University Medical Center Committee for Medical Ethics approved the experiment. An Ingenia 3T dual transmit MR system (Philips Healthcare) was used to acquire the *in vivo* data. A 12-element posterior receiver array, a 15-channel head coil, a 16-channel knee coil (also used for transmission) and a 16-element anterior receiver array were used for reception in the spine, the brain, the knee and the lower legs, respectively. The body coil was used for RF transmission, except for the knee scan.

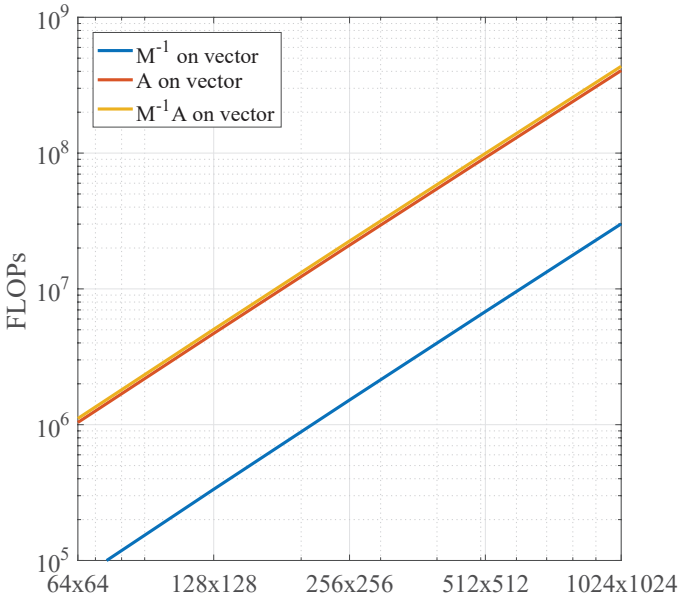

Figure 5.1: The complexity for different problem sizes. The number of FLOPs for the action of the preconditioner M on a vector (black), A on a vector (red), and the combination of the two (yellow) are depicted for $N_c = 12$.

For the spine data set, T_1-weighted images were acquired using a turbo spin-echo (TSE) sequence with the following parameters: field of view (FOV) = 340×340 mm^2; in-plane resolution 0.66×0.66 mm^2; 4 mm slice thickness; 15 slices; echo time (TE)/repetition time (TR)/TSE factor = 8 ms/ 648 ms/8; flip angle (FA) = 90°; refocusing angle = 120°; water-fat shift (WFS) = 1.5 pixels; and scan time = 2:12 min. T_2-weighted TSE scans had parameters: FOV = 340×340 mm^2; in-plane resolution 0.66×0.66 mm^2; 4 mm slice thickness; 15 slices; TE/TR/TSE factor = 113 ms/4008 ms/32; FA = 90°; WFS = 1.1 pixels; and scan time = 3:36 min.

For the brain data set, T_1-weighted images were acquired using an inversion recovery turbo spin-echo (IR TSE) sequence with parameters: FOV = 230×230 mm^2; in-plane resolution 0.90×0.90 mm^2; 4 mm slice thickness; 24 slices; TE/TR/TSE factor = 20 ms/2000 ms/8; refocusing angle = 120°; IR delay: 800 ms; WFS = 2.6 pixels; and scan time = 05:50 min. T_2^*-weighted images were measured using a gradient echo (FFE) sequence with parameters: FOV = 230×230 mm^2; in-plane resolution 0.90×0.90 mm^2; 4 mm slice thickness; 28 slices; TE/TR = 16 ms/817 ms; FA = 18°; WFS = 2 pixels; and scan time = 3:33 min.

For the knee data set, T_1-weighted images were acquired using an FFE sequence with parameters: FOV = 160×160 mm^2; in-plane resolution 1.25×1.25 mm^2; 3mm slice thickness; 32 slices; TE/TR = 10 ms/455 ms; FA = 90°; WFS = 1.4 pixels; and scan time = 1:01 min.

For the calf data set, T_1-weighted images were acquired using an FFE sequence with parameters: FOV = 300×300 mm^2; in-plane resolution 1.17×1.17 mm^2; 7 mm slice thick-

ness; 24 slices; TE/TR = 16 ms/500 ms; FA = 90°; WFS = 1.5 pixels; and scan time = 2:11 min.

The different acquisitions techniques (TSE, FFE) were chosen to address different basic contrasts used in daily clinical practice. Undersampling in the case of non-stationary echo signals, such as during a T_2-decaying TSE train, can result in image quality degradation. This effect can be mitigated, for example, in TSE scans using variable refocusing angle schemes as outlined in [44].

To show the performance of the preconditioner also in the presence of these and similar effects, scans in the brain were acquired directly in undersampled mode employing a simple variable density sampling pattern, with acceleration factors R=2 and R=3. To validate the results, fully sampled data is acquired as well in a separate scan. Data for a T_2-weighted TSE scan (R=2, FOV = 230×230 mm^2; in-plane resolution 0.90×0.90 mm^2; 4 mm slice thickness; 1 slice; TE/TR/TSE factor = 80 ms/3000 ms/16; refocusing angle = 120°; WFS = 2.5 pixels; and scan time = 00:30 min), a FLAIR scan (R=2, FOV = 240×224 mm^2; in-plane resolution 1.0×1.0 mm^2; 4 mm slice thickness; 1 slice; TE/TR/TSE factor = 120 ms/9000 ms/24; IR delay = 2500 ms; refocusing angle = 110°; WFS = 2.7 pixels; and scan time = 01:30 min) and a 3D magnetization prepared T_1-weighted turbo field echo (TFE) scan (R=3, FOV = 250×240×224 mm^2; 1.0 mm^3 isotropic resolution; TE/TR = 4.6 ms/9.9 ms; TFE factor = 112; TFE prepulse delay = 1050 ms; flip angle = 8°; WFS = 0.5 pixels; and scan time = 04:17 min).

COIL SENSITIVITY MAPS

Unprocessed k-space data was stored per channel and used to construct complex coil sensitivity maps for each channel [45]. Note that the coil sensitvity maps are normalized such that

$$\hat{S}_i = \left[\sum_{j=1}^{\mathrm{N_c}} S_j^H S_j \right]^{-\frac{1}{2}} S_i \qquad \text{for } i = 1, ..., \mathrm{N_c}.$$

The normalized coil sensitivity maps were given zero intensity outside the subject, resulting in an improved SNR of the final reconstructed image. For the data model to be consistent, also the individual coil images were normalized according to

$$m_i = \hat{S}_i \sum_{j=1}^{\mathrm{N_c}} \hat{S}_j^H m_j \qquad \text{for } i = 1, ..., \mathrm{N_c}.$$

COIL COMPRESSION

Reconstruction of the spine data set was performed with and without coil compression. A compression matrix was constructed as in [46], and multiplied by the normalized individual coil images and the coil sensitivity maps, to obtain virtual coil images and sensitivity maps. The six least dominant virtual coils were ignored to speed up the reconstruction.

UNDERSAMPLING

Two variable density undersampling schemes were studied: a random line pattern in the foot-head direction, referred to as structured sampling, and a fully random pattern, referred to as random sampling. Different undersampling factors were used for both schemes.

RECONSTRUCTION

The Split Bregman algorithm was implemented in MATLAB (The MathWorks, Inc.). All image reconstructions were performed in 2D on a Windows 64-bit machine with an Intel i3-4160 CPU @ 3.6 GHz and 8 GB internal memory.

Reconstructions were performed for reconstruction matrix sizes of 128 × 128, 256 × 256, and 512 × 512, and the largest reconstruction matrix was interpolated to obtain a simulated data set of size 1024 × 1024 for theoretical comparison. For prospectively undersampled scans, additional matrix sizes of 240 × 224 were acquired. For the 3D scan, an FFT was first performed along the readout direction, after which one slice was selected. To investigate the effect of the regularization parameters on the performance of the preconditioner, three different regularization parameter sets were chosen as:

1. set 1 $\mu = 10^{-3}$, $\lambda = 4 \cdot 10^{-3}$, and $\gamma = 10^{-3}$
2. set 2 $\mu = 10^{-2}$, $\lambda = 4 \cdot 10^{-3}$, and $\gamma = 10^{-3}$
3. set 3 $\mu = 10^{-3}$, $\lambda = 4 \cdot 10^{-3}$, and $\gamma = 4 \cdot 10^{-3}$.

The Daubechies 4 wavelet transform was used for W. Furthermore, the SB algorithm was performed with an inner loop of one iteration and an outer loop of 20 iterations. The tolerance (relative residual norm) in the PCG algorithm was set to $\epsilon = 10^{-3}$.

RESULTS

Figure 5.2 shows the T_1-weighted TSE spine images for a reconstruction matrix size of 512 × 512, reconstructed with the SB implementation for a fully sampled data set and for undersampling factors of four (R=4) and eight (R=8), where structured Cartesian sampling masks were used. The quality of the reconstructed images for R=4 and R=8 demonstrate the performance of the compressed sensing algorithm. The difference between the fully sampled and undersampled reconstructed images are shown (magnified five times) in Fig. 5.2d and Fig. 5.2e for R=4 and R=8, respectively.

The fully built system matrix $\mathsf{A} = \mathsf{F}^H\mathsf{K}\mathsf{F}$ is compared with its circulant approximation $\mathsf{F}^H\text{diag}\{\mathbf{k}\}\mathsf{F}$ in Fig. 5.3 (top-row) for both structured and random Cartesian undersampling in the spine, without regularization to focus on the approximated term containing the coil sensitivities. The elements of A contain many zeros due to the lack of coil sensitivity in a large part of the image domain when using cropped coil sensitivity maps. These zeros are not present in the circulant approximation, since the circulant property is enforced by neglecting all off-diagonal elements in K. The entries introduced into the circulant approximation do not add relevant information to the system, because the image vector on which the system matrix acts contains zero signal in the region corresponding with the newly introduced entries. For the same reason, the absolute difference maps in the bottom row were masked by the coil-sensitive region of A, showing that the magnitude and phase are well approximated by assuming the circulant property. Figure 5.3 (bottom-row) and 5.4 show the same results for the brain, the knee and the calves, demonstrating the generalizability of this approach to different coil set-ups and geometries. The product of the inverse of the preconditioner M^{-1} and the system matrix A is shown for the spine, the brain, the knee and the calves in Fig. 5.5 and 5.6,

respectively. Different regularization parameter sets show that the preconditioner is a good approximate inverse, suggesting efficient convergence.

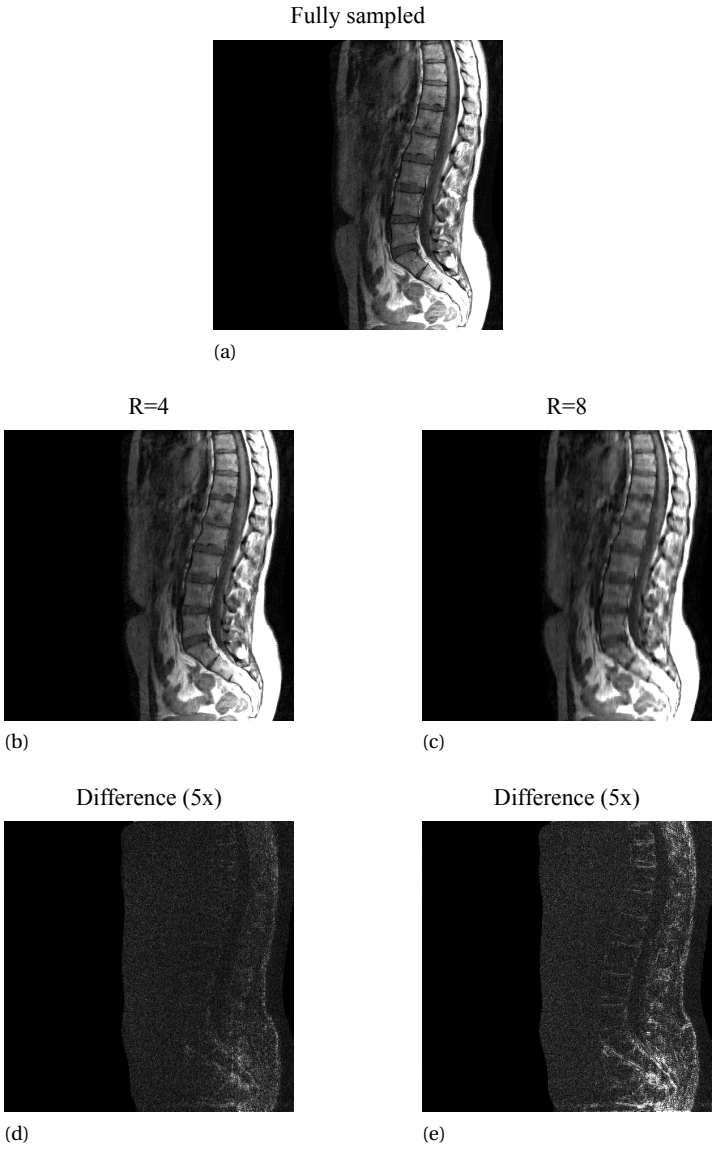

Figure 5.2: Reconstruction results for different structured Cartesian undersampling factors. (a) shows the fully sampled scan as a reference, whereas (b) and (c) depict the reconstruction results for undersampling factors four (R=4) and eight (R=8), respectively. The absolute difference, magnified five times, is shown in (d) and (e) for R=4 and R=8, respectively. The reconstruction matrix has dimensions 512×512. Regularization parameters were set to $\mu = 1 \cdot 10^{-3}$, $\lambda = 4 \cdot 10^{-3}$, and $\gamma = 1 \cdot 10^{-3}$.

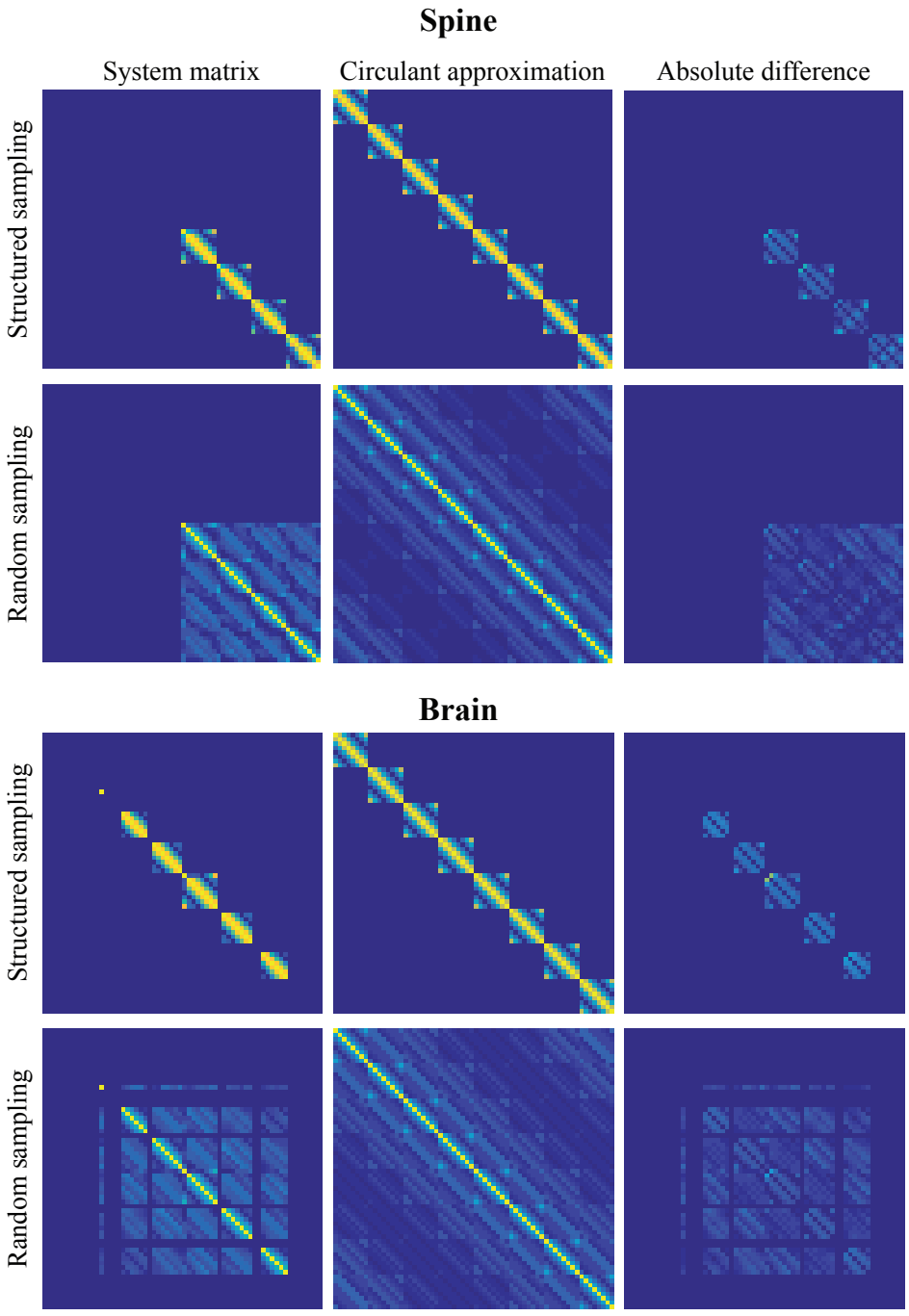

Figure 5.3: System matrix and its circulant approximation. The first and the second columns show the system matrix elements for structured and random undersampling and R=4, respectively, for the spine (a), the brain (b), the knee (c) and the calves (d). The top row depicts the elementwise magnitude for the true system matrix A, the second row depicts the elementwise magnitude for the circulant approximated system matrix and the bottom row shows the absolute difference between the true system matrix and the circulant approximation. The difference maps were masked by the nonzero-region of A, since only elements in the coil-sensitive region of the preconditioner describe the final solution.

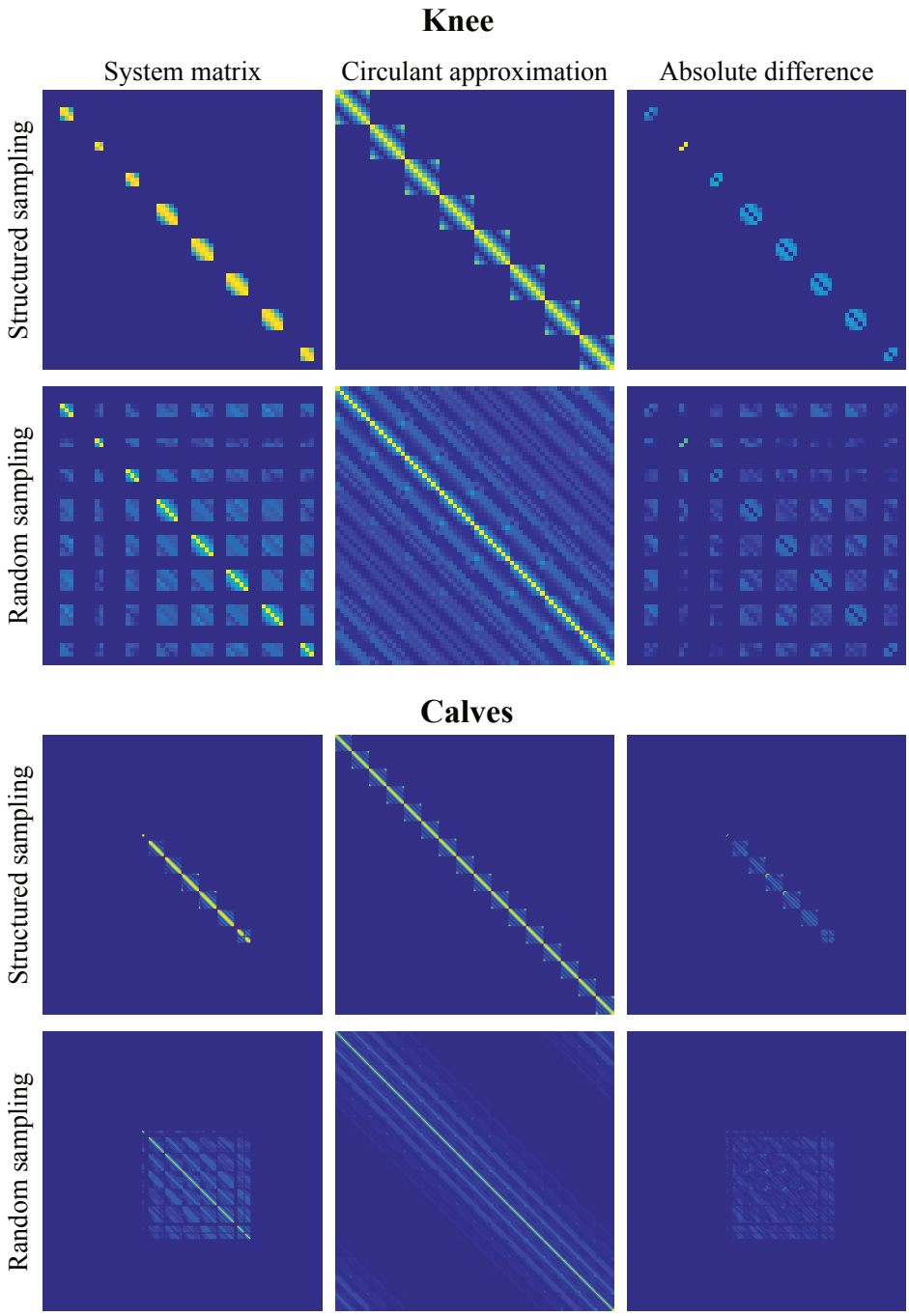

Figure 5.4: System matrix and its circulant approximation. The first and the second columns show the system matrix elements for structured and random undersampling and R=4, respectively, for the spine (a), the brain (b), the knee (c) and the calves (d). The top row depicts the elementwise magnitude for the true system matrix A, the second row depicts the elementwise magnitude for the circulant approximated system matrix and the bottom row shows the absolute difference between the true system matrix and the circulant approximation. The difference maps were masked by the nonzero-region of A, since only elements in the coil-sensitive region of the preconditioner describe the final solution.

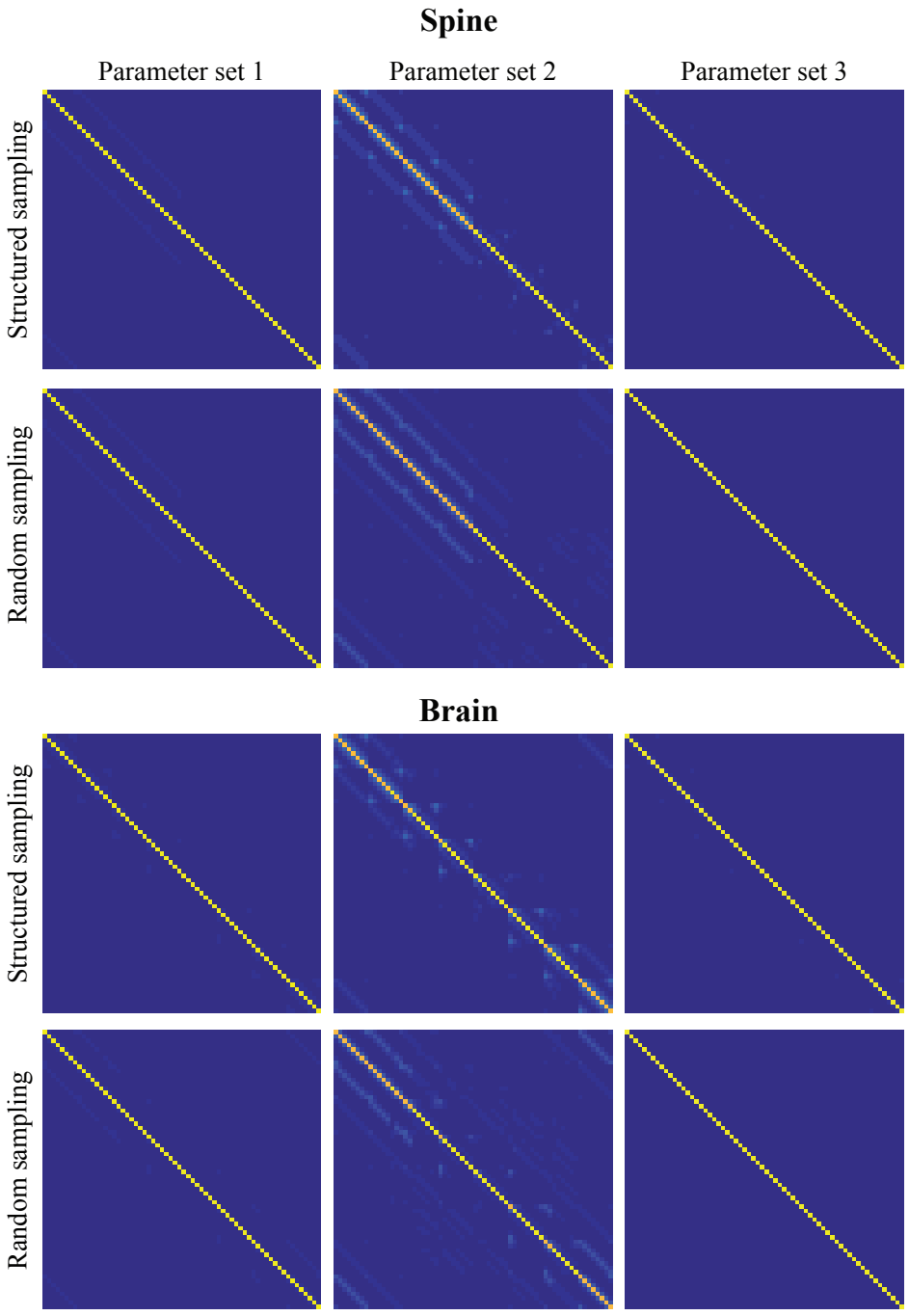

Figure 5.5: The new system matrix. The first and third row and the second and fourth row show the elements of the effective new system matrix $M^{-1}A$ for structured and random undersampling and R=4, respectively, for the the spine and the brain. The columns show this result for the three studied regularization parameter sets.

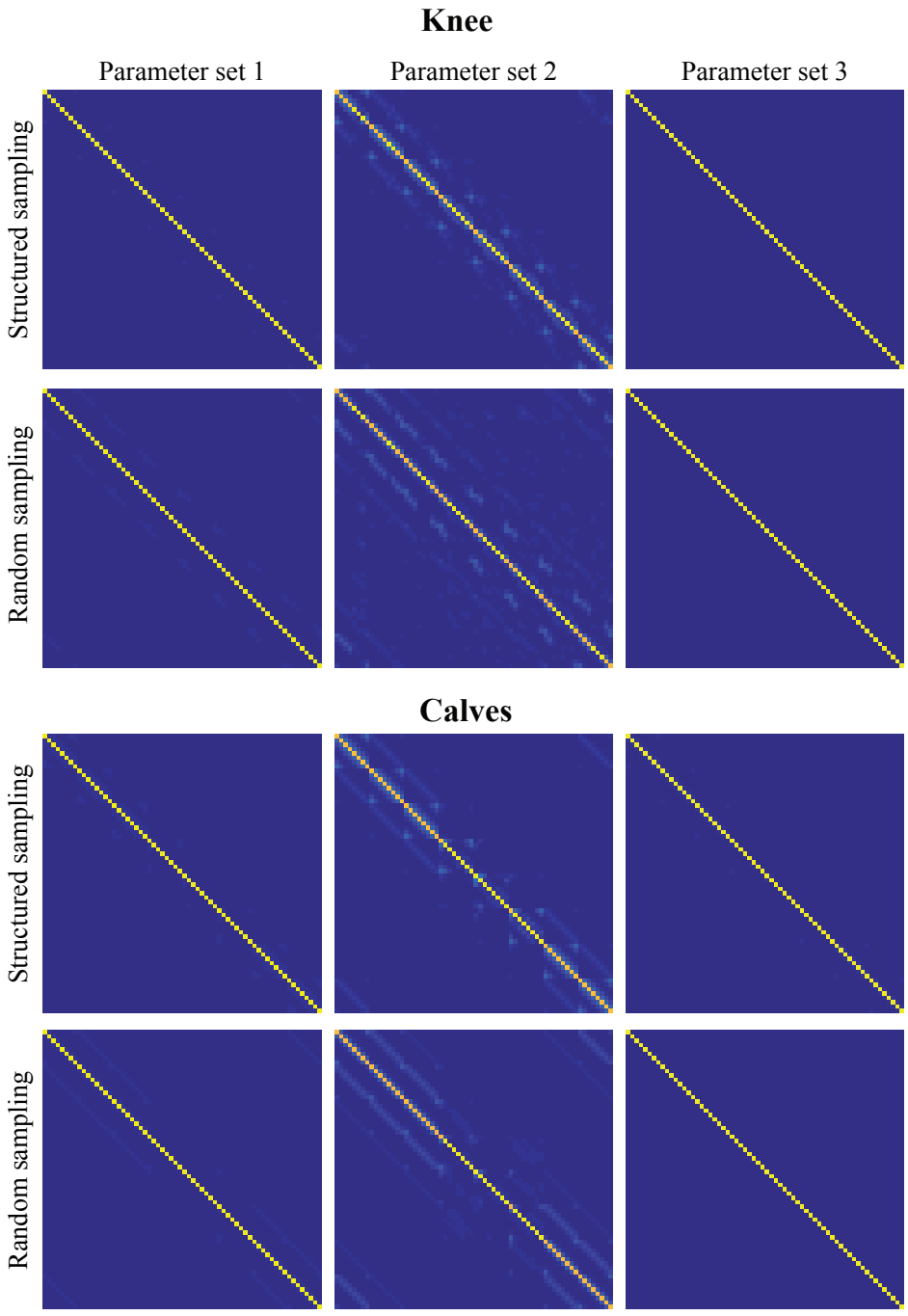

Figure 5.6: The new system matrix. The first and third row and the second and fourth row show the elements of the effective new system matrix $M^{-1}A$ for structured and random undersampling and R=4, respectively, for the the knee and the calves. The columns show this result for the three studied regularization parameter sets.

Table 5.2: Initialization times for constructing the preconditioner for different problem sizes. Even for very large problem sizes the initialization time does not exceed two seconds. Additional costs are given as percentage of the total reconstruction time without preconditioning.

Problem size	128×128	256×256	512×512	1024×1024
Initialization time (s)	0.0395	0.0951	0.3460	1.3371
Additional costs (%)	1.7	0.85	0.52	0.48

Table 5.2 reports the number of seconds needed to build the circulant preconditioner in MATLAB before the reconstruction starts, for different orders of the reconstruction matrix. Note that the actual number of unknowns in the corresponding systems is equal to the number of elements in the reconstruction matrix size, which leads to more than 1 million unknowns for the 1024×1024 case. For all matrix sizes the initialization time is negligible compared with the image reconstruction time.

Figure 5.7a shows the number of iterations required for PCG to converge in each Bregman iteration without preconditioner, with the Jacobi preconditioner and with the circulant preconditioner for regularization parameters $\mu = 10^{-3}, \lambda = 4 \cdot 10^{-3}$ and $\gamma = 10^{-3}$ and a reconstruction matrix size of 256×256. The Jacobi preconditioner does not reduce the number of iterations, which shows that the diagonal of the system matrix A does not contain enough information to result in a good approximation of A^{-1}. Moreover, it shows that the linear system is invariant under scaling. The circulant preconditioner, however, reduces the number of iterations considerably, leading to a total speed-up factor of 4.65 in the PCG part.

The effect of the reduced number of PCG iterations can directly be seen in the computation time for the reconstruction algorithm, plotted in Fig. 5.8 for different problem sizes. Figure 5.8a shows the total PCG computation time when completing the total SB method, whereas Fig. 5.8b shows the total computation time required to complete the entire reconstruction algorithm. A fivefold gain is achieved in the PCG part by reducing the number of PCG iterations, which directly relates to the results shown in Fig. 5.7a. The overall gain of the complete algorithm, however, is a factor 2.5 instead of 5, which can be explained by the computational costs of the update steps outside the PCG iteration loop (see Algorithm 5.1). Figure 5.8c also shows the error, defined as the normalized 2-norm difference with respect to the fully sampled image, as a function of time. The preconditioned SB scheme converges to the same accuracy as the original SB scheme, since the preconditioner only affects the required number of PCG iterations.

The number of iterations required by PCG for each Bregman iteration is shown in Fig. 5.7b for the three parameter sets studied. The preconditioned case always outperforms the non-preconditioned case, but the speed up factor depends on the regularization parameters. Parameter set 1 depicts the same result as shown in Fig. 5.7a and results in the best reconstruction of the fully sampled reference image. In parameter set 2 more weight is given to the data fidelity term by increasing the parameter μ. Since the preconditioner relies on an approximation of the data fidelity term, it performs less optimally than for smaller μ (such as in set 1) for the first few Bregman iterations, but there is still a threefold gain in performance. This behavior was already predicted in Figures 5.5

and 5.6. Finally, there is very little change between parameter set 3 and parameter set 1, because the larger wavelet regularization parameter γ gives more weight to a term that was integrated in the preconditioner in an exact way, as for the total variation term, without any approximations.

Figure 5.7c illustrates the required iterations when half of the coils are taken into account by coil compression. Only a small discrepancy is encountered for the first few iterations, since the global structure and content of the system matrix A remain the same, which demonstrates that coil compression and preconditioning can be combined to optimally reduce the reconstruction time.

The method also works for different coil configurations. In Figures 5.9-5.11 the result is shown when using the 15-channel head coil for the brain scans, the 16-channel knee coil for a knee scan and the 16-channel receive array for the calf scan. The circulant preconditioner clearly reduces the number of iterations, with an overall speed-up factor of about 4.1-4.5 in the PCG part.

Figure 5.12 shows reconstruction results for scans where the data was directly acquired in undersampled mode instead of retrospectively undersampled, for a T_2-weighted TSE scan, a FLAIR scan and a 3D magnetization prepared T_1-weighted TFE scan, leading to PCG acceleration factors of 4.2, 5.1 and 5.4, respectively. The convergence behavior is similar to the one observed for the retrospectively undersampled data, demonstrating the robustness of the preconditioning approach in realistic scan setups.

DISCUSSION AND CONCLUSIONS

In this work we have introduced a preconditioner that reduces the reconstruction times for CS and PI problems, without compromising the stability of the numerical SB schem. Solving an ℓ_2-norm minimization problem is the most time-consuming part of this algorithm. This ℓ_2-norm minimization problem is written as a linear system of equations characterized by the system matrix A. The effectiveness of the introduced preconditioner comes from the fact that the system matrix is approximated as a BCCB matrix. Both the total variation and the wavelet regularization terms are BCCB, which means that only the data fidelity term, which is not BCCB due to the sensitivity profiles of the receive coils and the undersampling of k-space, is approximated by assuming a BCCB structure in the construction of the preconditioner. This approximation has been shown to be accurate for CS-PI problem formulations. The efficiency of this approach comes from the fact that BCCB matrices are diagonalized by Fourier transformations, which means that the inverse of the preconditioner can simply be found by inverting a diagonal matrix and applying two additional FFTs.

With the designed preconditioner the most expensive ℓ_2-norm problem was solved almost 5 times faster than without preconditioning, resulting in an overall speed up factor of about 2.5. The discrepancy between the two speed up factors can be explained by the fact that apart from solving the linear problem, update steps also need to be performed. Step 4 and steps 13-15 of Algorithm 1 are especially time consuming since for each coil a 2D Fourier transform needs to be performed. Furthermore, the wavelet computation in steps 4, 8, and 11 are time consuming factors as well. Therefore, speed up factors higher than 2.5 are expected for an optimized Bregman algorithm. Further acceleration can be obtained through coil compression [46, 47], as the results in this study

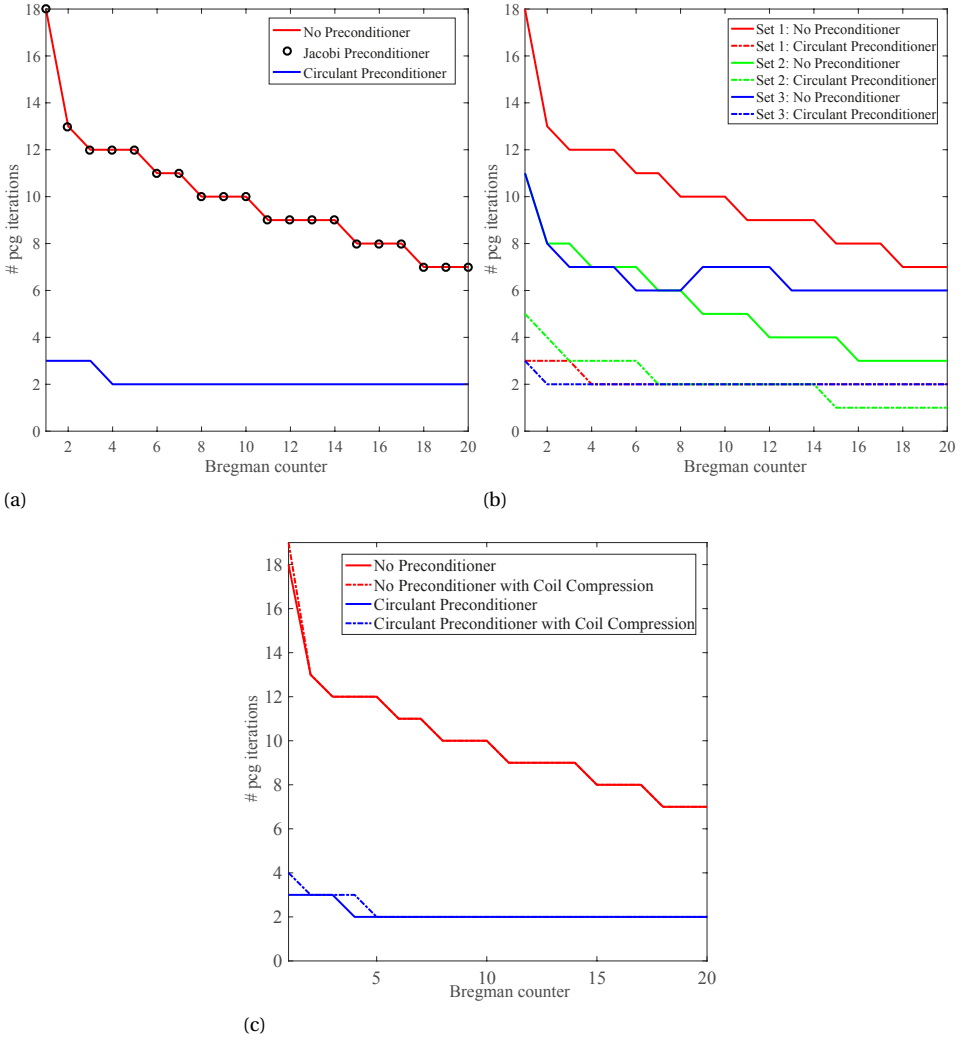

Figure 5.7: Number of iterations needed per Bregman iteration. The circulant preconditioner reduces the number of iterations considerably compared with the non-preconditioned case. The Jacobi preconditioner does not reduce the number of iterations due to the poor approximation of the system matrix' inverse. (a) depicts the iterations for Set 1: $(\mu = 1 \cdot 10^{-3}, \lambda = 4 \cdot 10^{-3}, \gamma = 1 \cdot 10^{-3})$, whereas (b) depicts the iterations for Set 1, Set 2: $(\mu = 1 \cdot 10^{-2}, \lambda = 4 \cdot 10^{-3}, \gamma = 1 \cdot 10^{-3})$, and Set 3: $(\mu = 1 \cdot 10^{-3}, \lambda = 4 \cdot 10^{-3}, \gamma = 4 \cdot 10^{-3})$ The preconditioner shows the largest speed up factor when the regularization parameters are well-balanced. (c) Shown are the number of iterations needed per Bregman iteration with and without coil compression applied. The solid lines and the dashed lines depict the results with and without coil compression, respectively.

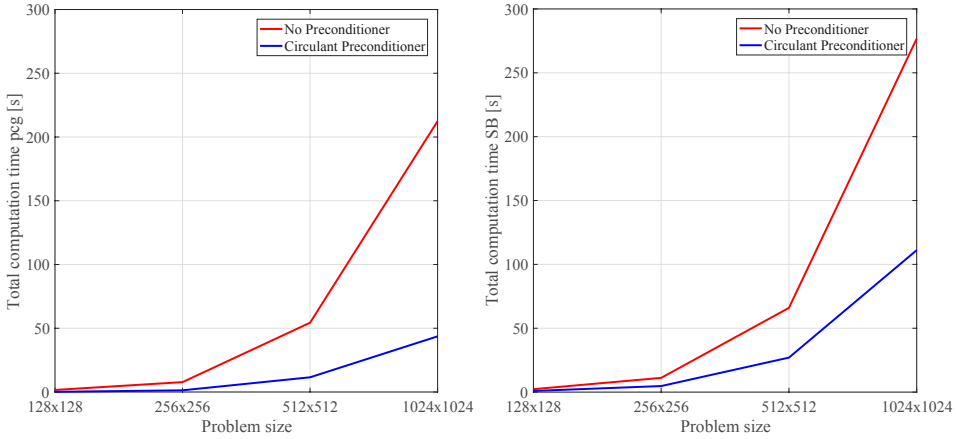

(a)

(b)

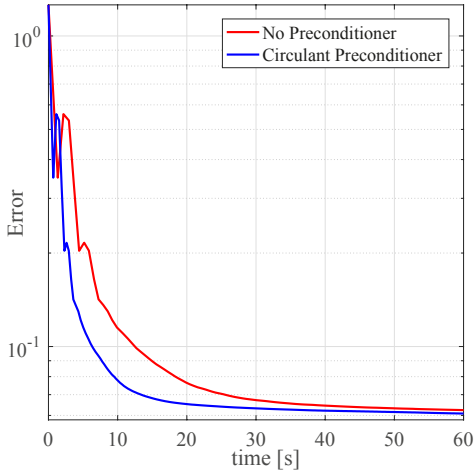

(c)

Figure 5.8: Computation time for 20 Bregman iterations and different problem sizes. (a) Using the preconditioner, the total computation time for the PCG part in 20 Bregman iterations is reduced by more than a factor of 4.5 for all studied problem sizes. (b) The computation time for 20 Bregman iterations of the entire algorithm also includes the Bregman update steps, so that the total speedup factor is approximately 2.5 for the considered problem sizes. (c) The two methods converge to the same solution, plotted here for R=4 and a reconstruction matrix size 256×256.

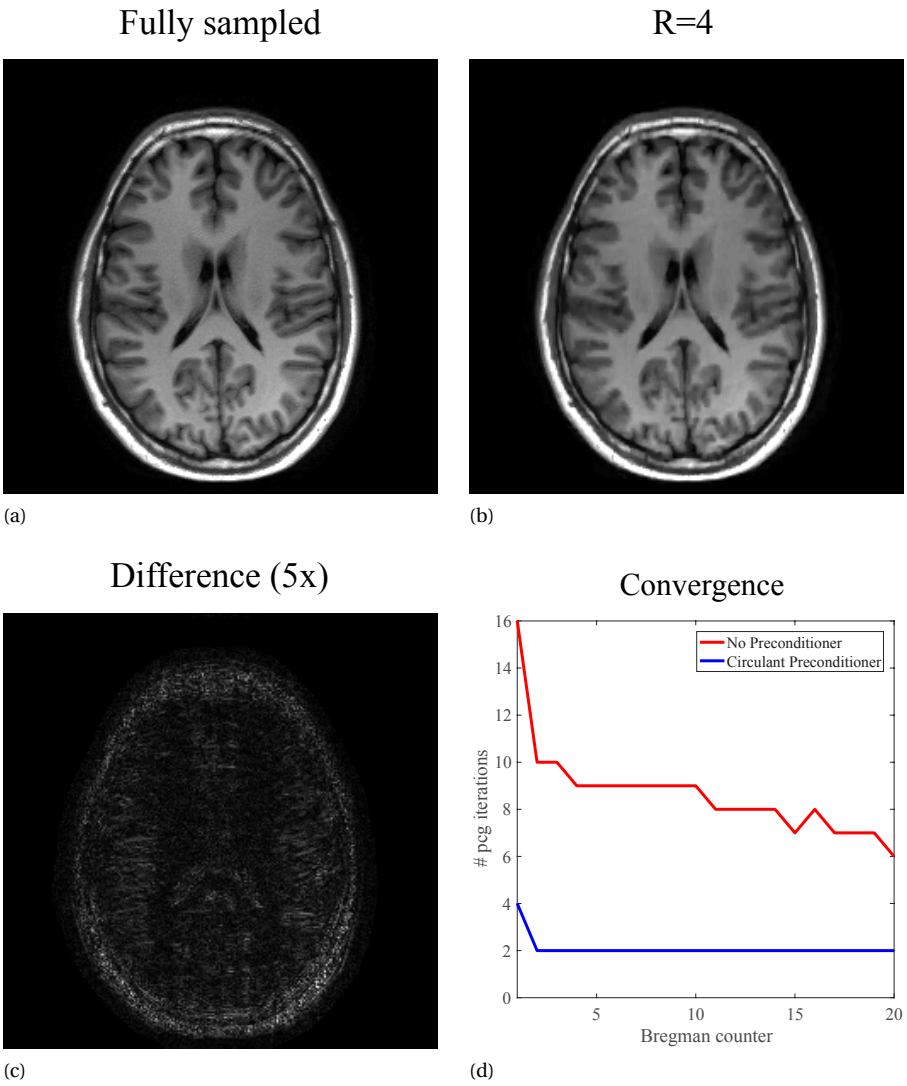

Figure 5.9: Reconstruction results for the brain. (a) shows the fully sampled scan as a reference, whereas (b) depicts the reconstruction results for an undersampling factor of four (R=4). The absolute difference, magnified five times, is shown in (c). The reconstruction matrix has dimensions 256×256 and regularization parameters were chosen as $\mu = 1 \cdot 10^{-3}, \lambda = 4 \cdot 10^{-3}$, and $\gamma = 2 \cdot 10^{-3}$. The convergence results for the PCG part with and without preconditioner are plotted in (d), showing similar reduction factors as with the posterior coil.

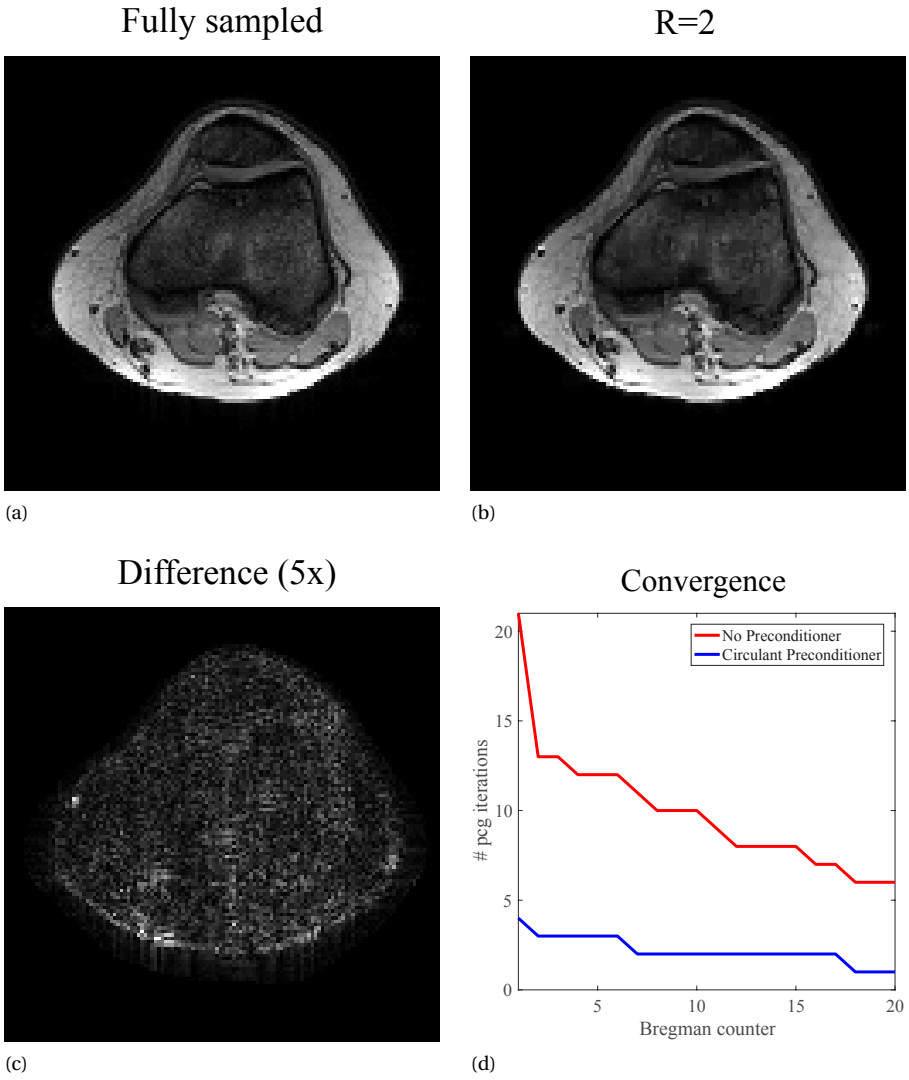

Figure 5.10: Reconstruction results for the knee. (a) shows the fully sampled scan as a reference, whereas (b) depicts the reconstruction results for an undersampling factor of two (R=2). The absolute difference, magnified five times, is shown in (c). The reconstruction matrix has dimensions 128×128 and regularization parameters were chosen as $\mu = 0.1$, $\lambda = 0.4$, and $\gamma = 0.1$.

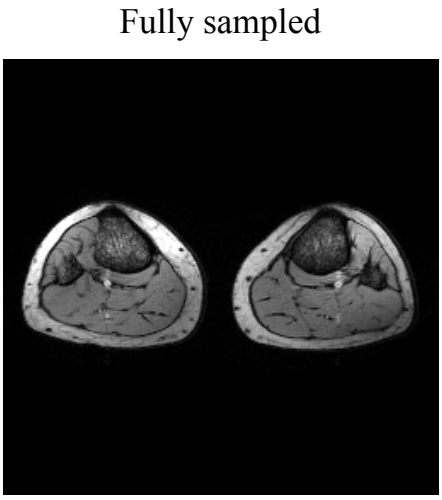

(a)

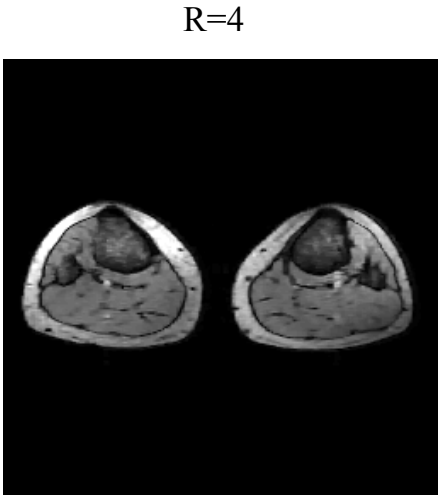

(b)

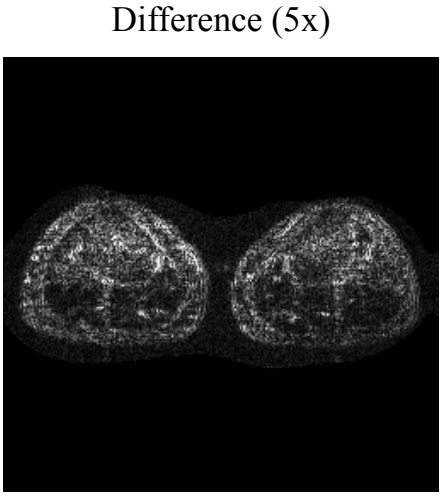

(c)

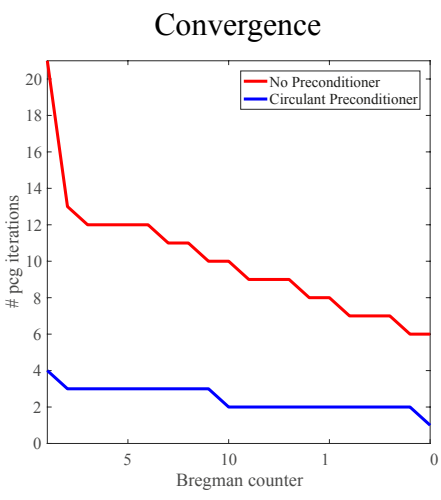

(d)

Figure 5.11: Reconstruction results for the calves. (a) shows the fully sampled scan as a reference, whereas (b) depicts the reconstruction results for an undersampling factor of four (R=4). The absolute difference, magnified five times, is shown in (c). The reconstruction matrix has dimensions 256×256 and R=4. Regularization parameters were chosen as $\mu = 0.1, \lambda = 0.4$, and $\gamma = 0.1$.

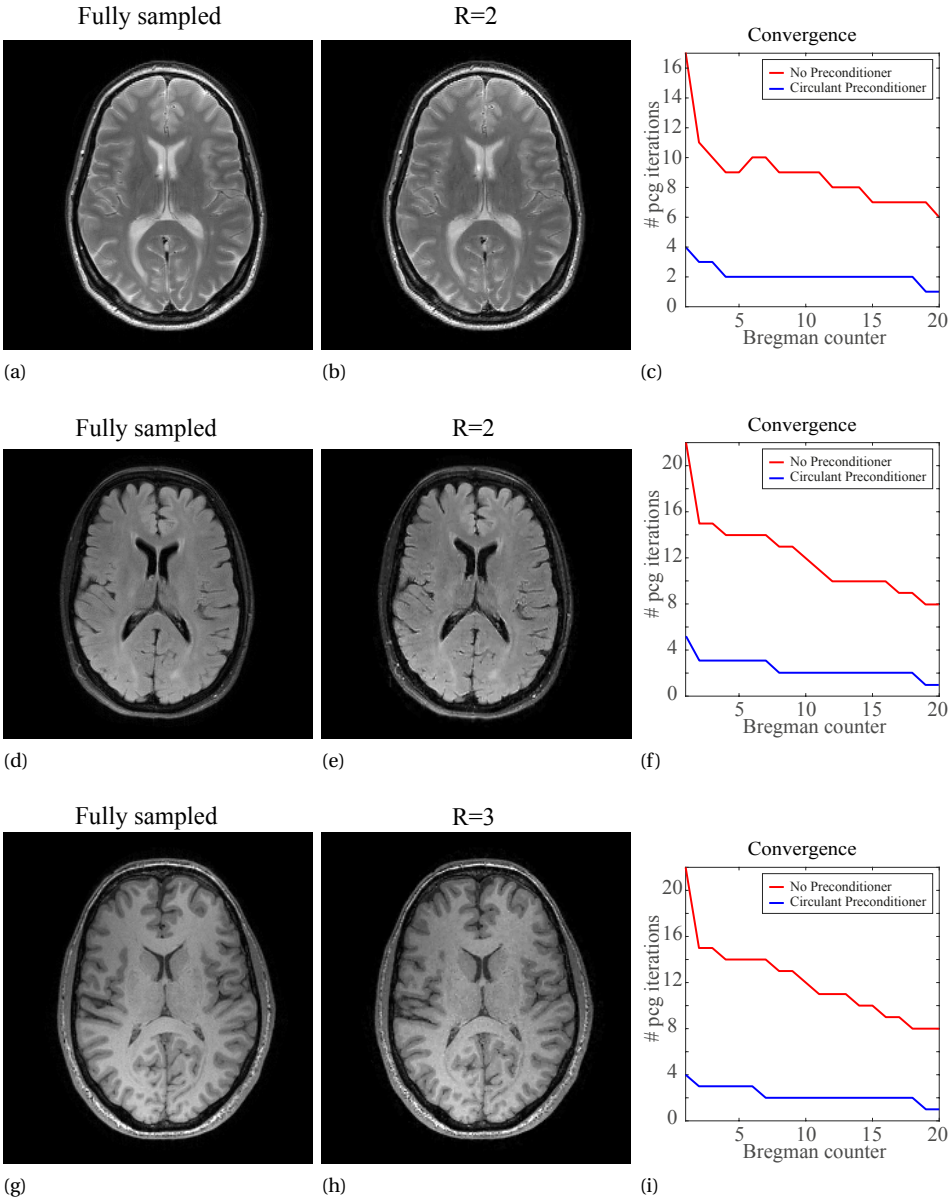

Figure 5.12: Reconstruction results for data acquired in fully and undersampled mode. (a) shows a fully sampled scan as a reference for a T_2-weighted TSE scan in the brain, whereas (b) depicts the reconstruction results for a prospectively undersampled scan with an acceleration factor of two (R=2). The reconstruction matrix has dimensions 256 × 256 and regularization parameters were chosen as $\mu = 1, \lambda = 4$, and $\gamma = 1$. The convergence results for the PCG part with and without preconditioner are plotted in (c). Results for the FLAIR brain scan are shown in (d)-(f) for a reconstruction matrix size 240 × 224 and R=2. Regularization parameters were chosen as $\mu = 1.4 \cdot 10^2, \lambda = 5.7 \cdot 10^2$, and $\gamma = 1.4 \cdot 10^2$. Results for a 3D magnetization prepared T_1-weighted TFE scan in the brain are shown in (g)-(i) for a reconstruction matrix size 240 × 224 and R=3. Regularization parameters were chosen as $\mu = 0.5, \lambda = 2$, and $\gamma = 0.5$. Note that the data in the left column stem from a different measurement as the data in the middle column.

showed that it has negligible effect on the performance of the preconditioner.

The time required to construct the preconditioner is negligible compared with the reconstruction times as it involves only a few FFTs. The additional costs of applying the preconditioner on a vector is negligible as well, because it involves only two Fourier transformations and an inexpensive multiplication with a diagonal matrix. Therefore, the method is highly scalable and can handle large problem sizes.

The preconditioner works optimally when the regularization terms in the minimization problem are BCCB matrices in the final system matrix. This implies that the total variation operators should be chosen such that the final total variation matrix is BCCB, and that the wavelet transform should be unitary. Both the system matrix and the preconditioner can be easily adjusted to support single regularization instead of the combination of two regularization approaches.

The BCCB approximation for the data fidelity term supports both structured and random Cartesian undersampling patterns and works well for different undersampling factors. The performance of the preconditioner was experimentally validated using a variable density sampling scheme to prospectively undersample the data. The convergence behavior shows similar results as the retrospectively undersampled case.

The regularization parameters were shown to influence the performance of the preconditioner. Since the only approximation in the preconditioner comes from the approximation of the data fidelity term, the preconditioner results in poorer performance if the data fidelity term is very large compared with the regularization terms. In practice, such a situation is not likely to occur if the regularization parameters are chosen such that an optimal image quality is obtained in the reconstructed image. In this work, the regularization parameters were chosen empirically and were kept constant throughout the algorithm. For SB-type methods, however, updating the regularization parameters during the algorithm makes the performance of the algorithm less dependent on the initial choice of the parameters [48]. Moreover, it might result in improved convergence, from which our work can benefit.

This work focussed on the linear part of the SB method, in which only the right-hand side vector changes in each iteration and not the system matrix. Other ℓ_1-norm minimization algorithms exist that require a linear solver [49], such as IRLS or Second-Order Cone Programming. For those type of algorithms linear preconditioning techniques can be applied as well. Although the actual choice for the preconditioner depends on the system matrix of the linear problem, which is in general different for different minimization algorithms, similar techniques as used in the current work can be exploited to construct a preconditioner for other minimization algorithms.

As outlined earlier in the introduction, there are alternative approaches to eliminating the iterative scheme to solve the ℓ_2-norm minimization problem. Although a detailed comparison of techniques is difficult due to the required choice of reconstruction parameters, it is worth noting that in [31] a comparison was made between the non-preconditioned SB scheme that we also use as comparison in our work, and the authors' extra variable splitting method. Their results suggest that the preconditioned SB scheme with an acceleration factor of 2.5 is very similar to the performance of the method adopting extra variable splitting. Moreover, variable splitting is not possible for non-Cartesian data acquisition, but is easily incorporated into the preconditioned SB

approach. In this extension, the block circulant matrix with circulant blocks is replaced by the block Toeplitz matrix with Toeplitz blocks [40]. Given the promising results for Cartesian trajectories, future work will therefore focus on including non-Cartesian data trajectories into a single unified preconditioned SB framework.

Another large group of reconstruction algorithms involve gradient update steps; examples in this group are the Iterative Shrinkage-Thresholding Algorithm (ISTA), FISTA, MFISTA, and BARISTA [21, 50–52]. In [52] it was discussed that the performance of FISTA, for which convergence depends on the maximum sum of squared absolute coil sensitivity value, can be poor due to large variations in coil sensitivities. In our work, however, the coil sensitivity maps were normalized such that the corresponding sum-of-squares map is constant and equal to one in each spatial location within the object region. The normalization of these coil sensitivities might therefore lead to acceleration of FISTA-type algorithms. Thus, it would be interesting to compare the performance of the preconditioned SB algorithm with the performance of FISTA when incorporating normalized coil sensitivities into both algorithms.

In conclusion, the designed FFT-based preconditioner reduces the number of iterations required for solving the linear problem in the SB algorithm considerably, resulting in an overall acceleration factor of 2.5 for PI-CS reconstructions. The approach works for different coil-array configurations, MR sequences, and non-power of two acquisition matrices, and the time to construct the preconditioner is negligible. Therefore, it can be easily used and implemented, allowing for efficient computations.

REFERENCES

[1] A. Deshmane, V. Gulani, M. A. Griswold, and N. Seiberlich, "Parallel MR imaging," *Journal of Magnetic Resonance Imaging*, vol. 36, no. 1, pp. 55–72, 2012.

[2] M. Blaimer, F. Breuer, M. Mueller, R. M. Heidemann, M. A. Griswold, and P. M. Jakob, "SMASH, SENSE, PILS, GRAPPA: how to choose the optimal method." *Topics in magnetic resonance imaging : TMRI*, vol. 15, no. 4, pp. 223–36, 2004.

[3] K. P. Pruessmann, M. Weiger, M. B. Scheidegger, and P. Boesiger, "SENSE: sensitivity encoding for fast MRI." *Magnetic resonance in medicine*, vol. 42, no. 5, pp. 952–62, 1999.

[4] M. A. Griswold, P. M. Jakob, R. M. Heidemann, M. Nittka, V. Jellus, J. Wang, B. Kiefer, and A. Haase, "Generalized autocalibrating partially parallel acquisitions (GRAPPA)," *Magnetic Resonance in Medicine*, vol. 47, no. 6, pp. 1202–1210, 2002.

[5] D. Donoho, M. Elad, and V. Temlyakov, "Stable recovery of sparse overcomplete representations in the presence of noise," *IEEE Transactions on Information Theory*, vol. 52, no. 1, pp. 6–18, 2006.

[6] M. Lustig, D. Donoho, and J. M. Pauly, "Sparse MRI: The application of compressed sensing for rapid MR imaging," *Magnetic Resonance in Medicine*, vol. 58, no. 6, pp. 1182–1195, 2007.

[7] R. Otazo, D. Kim, L. Axel, and D. K. Sodickson, "Combination of compressed sensing and parallel imaging for highly accelerated first-pass cardiac perfusion MRI," *Magnetic Resonance in Medicine*, vol. 64, no. 3, pp. 767–776, 2010.

[8] D. Liang, B. Liu, J. Wang, and L. Ying, "Accelerating SENSE using compressed sensing," *Magnetic Resonance in Medicine*, vol. 62, no. 6, pp. 1574–1584, 2009.

[9] H. Chandarana, L. Feng, T. K. Block, A. B. Rosenkrantz, R. P. Lim, J. S. Babb, D. K. Sodickson, and R. Otazo, "Free-breathing contrast-enhanced multiphase MRI of the liver using a combination of compressed sensing, parallel imaging, and golden-angle radial sampling." *Investigative radiology*, vol. 48, no. 1, pp. 10–6, 2013.

[10] S. P. Boyd and L. Vandenberghe, "Convex optimization," in *Convex optimization*. Cambridge: Cambridge University Press, 2004, ch. 9, p. 716.

[11] E. J. Candès, M. B. Wakin, and S. P. Boyd, "Enhancing Sparsity by Reweighted 1 Minimization," *Journal of Fourier Analysis and Applications*, vol. 14, no. 5-6, pp. 877–905, 2008.

[12] K. T. Block, M. Uecker, and J. Frahm, "Undersampled radial MRI with multiple coils. Iterative image reconstruction using a total variation constraint," *Magnetic Resonance in Medicine*, vol. 57, no. 6, pp. 1086–1098, 2007.

[13] S. Vasanawala, M. Murphy, M. Alley, P. Lai, K. Keutzer, J. Pauly, and M. Lustig, "Practical parallel imaging compressed sensing MRI: Summary of two years of experience in accelerating body MRI of pediatric patients," in *IEEE International Symposium on*

Biomedical Imaging: From Nano to Macro. IEEE, 2011, pp. 1039–1043.

[14] T. Goldstein and S. Osher, "The Split Bregman Method for L1-Regularized Problems," *SIAM Journal on Imaging Sciences*, vol. 2, no. 2, pp. 323–343, 2009.

[15] M. Murphy, M. Alley, J. Demmel, K. Keutzer, S. Vasanawala, and M. Lustig, "Fast L1-SPIRiT Compressed Sensing Parallel Imaging MRI: Scalable Parallel Implementation and Clinically Feasible Runtime," *IEEE Transactions on Medical Imaging*, vol. 31, no. 6, pp. 1250–1262, 2012.

[16] Shiqian Ma, Wotao Yin, Yin Zhang, and A. Chakraborty, "An efficient algorithm for compressed MR imaging using total variation and wavelets," in *IEEE Conference on Computer Vision and Pattern Recognition*. IEEE, 2008, pp. 1–8.

[17] S. Ramani and J. A. Fessler, "An accelerated iterative reweighted least squares algorithm for compressed sensing MRI," in *IEEE International Symposium on Biomedical Imaging: From Nano to Macro*. IEEE, 2010, pp. 257–260.

[18] B. Liu, K. King, M. Steckner, J. Xie, J. Sheng, and L. Ying, "Regularized sensitivity encoding (SENSE) reconstruction using bregman iterations," *Magnetic Resonance in Medicine*, vol. 61, no. 1, pp. 145–152, 2009.

[19] S.-J. Kim, K. Koh, M. Lustig, and S. Boyd, "An Efficient Method for Compressed Sensing," in *IEEE International Conference on Image Processing*. IEEE, 2007, pp. III – 117–III – 120.

[20] E. J. Candes and J. K. Romberg, "Signal recovery from random projections," in *SPIE Proceedings on Electronic Imaging*, C. A. Bouman and E. L. Miller, Eds., vol. 5674. International Society for Optics and Photonics, 2005, p. 76.

[21] I. Daubechies, M. Defrise, and C. De Mol, "An iterative thresholding algorithm for linear inverse problems with a sparsity constraint," *Communications on Pure and Applied Mathematics*, vol. 57, no. 11, pp. 1413–1457, 2004.

[22] S. G. Lingala, Y. Hu, E. DiBella, and M. Jacob, "Accelerated Dynamic MRI Exploiting Sparsity and Low-Rank Structure: k-t SLR," *IEEE Transactions on Medical Imaging*, vol. 30, no. 5, pp. 1042–1054, 2011.

[23] D. Donoho, "Compressed sensing," *IEEE Transactions on Information Theory*, vol. 52, no. 4, pp. 1289–1306, 2006.

[24] L. Bregman, "The relaxation method of finding the common point of convex sets and its application to the solution of problems in convex programming," *USSR Computational Mathematics and Mathematical Physics*, vol. 7, no. 3, pp. 200–217, 1967.

[25] R.-Q. Jia, H. Zhao, and W. Zhao, "Convergence analysis of the Bregman method for the variational model of image denoising," *Applied and Computational Harmonic Analysis*, vol. 27, no. 3, pp. 367–379, 2009.

[26] S. Setzer, "Operator Splittings, Bregman Methods and Frame Shrinkage in Image Processing," *International*

Journal of Computer Vision, vol. 92, no. 3, pp. 265–280, 2011.

[27] J.-F. Cai, S. Osher, and Z. Shen, "Split Bregman Methods and Frame Based Image Restoration," *Multiscale Modeling & Simulation*, vol. 8, no. 2, pp. 337–369, 2010.

[28] O. L. Elvetun and B. F. Nielsen, "The split Bregman algorithm applied to PDE-constrained optimization problems with total variation regularization," *Computational Optimization and Applications*, vol. 64, no. 3, pp. 699–724, 2016.

[29] Jinpeng Zhou, Jianwu Li, and J. C. Gombaniro, "Combining SENSE and compressed sensing MRI With a fast iterative contourlet thresholding algorithm," in *2015 12th International Conference on Fuzzy Systems and Knowledge Discovery (FSKD)*. IEEE, 2015, pp. 1123–1127.

[30] S. F. Cauley, Y. Xi, B. Bilgic, J. Xia, E. Adalsteinsson, V. Balakrishnan, L. L. Wald, and K. Setsompop, "Fast reconstruction for multichannel compressed sensing using a hierarchically semiseparable solver," *Magnetic Resonance in Medicine*, vol. 73, no. 3, pp. 1034–1040, 2015.

[31] S. Ramani and J. A. Fessler, "Parallel MR Image Reconstruction Using Augmented Lagrangian Methods," *IEEE Transactions on Medical Imaging*, vol. 30, no. 3, pp. 694–706, 2011.

[32] N. Cai, W. Xie, Z. Su, S. Wang, and D. Liang, "Sparse Parallel MRI Based on Accelerated Operator Splitting Schemes," *Computational and Mathematical Methods in Medicine*, vol. 2016, pp. 1–14, 2016.

[33] M. V. Afonso, J. M. Bioucas-Dias, and M. A. T. Figueiredo, "Fast Image Recovery Using Variable Splitting and Constrained Optimization," *IEEE Transactions on Image Processing*, vol. 19, no. 9, pp. 2345–2356, 2010.

[34] M. Benzi, "Preconditioning Techniques for Large Linear Systems: A Survey," *Journal of Computational Physics*, vol. 182, no. 2, pp. 418–477, 2002.

[35] J. Scott and M. Tma, "On Signed Incomplete Cholesky Factorization Preconditioners for Saddle-Point Systems," *SIAM Journal on Scientific Computing*, vol. 36, no. 6, pp. A2984–A3010, 2014.

[36] M. Baumann, R. Astudillo, Y. Qiu, E. Y. M. Ang, M. B. van Gijzen, and R.-É. Plessix, "An MSSS-preconditioned matrix equation approach for the time-harmonic elastic wave equation at multiple frequencies," *Computational Geosciences*, vol. 22, no. 1, pp. 43–61, 2018.

[37] C. Chen, Y. Li, L. Axel, and J. Huang, "Real Time Dynamic MRI with Dynamic Total Variation," in *Proceedings of International Conference on MICCAI*. Boston, MA, USA: Springer, Cham, 2014, pp. 138–145.

[38] R. Li, Y. Li, R. Fang, S. Zhang, H. Pan, and J. Huang, "Fast Preconditioning for Accelerated Multi-contrast MRI Reconstruction," in *Proceedings of the International Conference on MICCAI*. Munich, Germany: Springer, Cham, 2015, pp. 700–707.

[39] Z. Xu, Y. Li, L. Axel, and J. Huang, "Efficient Preconditioning in Joint Total Variation Regularized Parallel MRI

Reconstruction," in *Proceedings of the International Conference on MICCAI*. Munich, Germany: Springer, Cham, 2015, pp. 563–570.

[40] D. S. Weller, S. Ramani, and J. A. Fessler, "Augmented Lagrangian with variable splitting for faster non-Cartesian L1-SPIRiT MR image reconstruction." *IEEE Transactions on Medical Imaging*, vol. 33, no. 2, pp. 351–361, 2014.

[41] Y. Saad, *Iterative methods for sparse linear systems*. Society for Industrial and Applied Mathematics (SIAM, 3600 Market Street, Floor 6, Philadelphia, PA 19104), 2003.

[42] R. N. R. N. Bracewell, *The Fourier transform and its applications*. McGraw Hill, 2000.

[43] R. M. Gray, "Toeplitz and Circulant Matrices: A Review," *Foundations and Trends® in Communications and Information Theory*, vol. 2, no. 3, pp. 155–239, 2005.

[44] J. P. Mugler, "Optimized three-dimensional fast-spin-echo MRI," *Journal of Magnetic Resonance Imaging*, vol. 39, no. 4, pp. 745–767, 2014.

[45] M. Uecker, P. Lai, M. J. Murphy, P. Virtue, M. Elad, J. M. Pauly, S. S. Vasanawala, and M. Lustig, "ESPIRiT-an eigenvalue approach to autocalibrating parallel MRI: Where SENSE meets GRAPPA," *Magnetic Resonance in Medicine*, vol. 71, no. 3, pp. 990–1001, 2014.

[46] F. Huang, S. Vijayakumar, Y. Li, S. Hertel, and G. R. Duensing, "A software channel compression technique for faster reconstruction with many channels," *Magnetic Resonance Imaging*, vol. 26, no. 1, pp. 133–141, 2008.

[47] T. Zhang, J. M. Pauly, S. S. Vasanawala, and M. Lustig, "Coil compression for accelerated imaging with Cartesian sampling," *Magnetic Resonance in Medicine*, vol. 69, no. 2, pp. 571–582, 2013.

[48] S. Boyd, N. Parikh, E. Chu, B. Peleato, and J. Eckstein, "Distributed Optimization and Statistical Learning via the Alternating Direction Method of Multipliers," *Foundations and Trends® in Machine Learning*, vol. 3, no. 1, pp. 1–122, 2010.

[49] P. Rodriguez and B. Wohlberg, "Efficient Minimization Method for a Generalized Total Variation Functional," *IEEE Transactions on Image Processing*, vol. 18, no. 2, pp. 322–332, 2009.

[50] A. Beck and M. Teboulle, "A Fast Iterative Shrinkage-Thresholding Algorithm for Linear Inverse Problems," *SIAM Journal on Imaging Sciences*, vol. 2, no. 1, pp. 183–202, 2009.

[51] ——, "Fast Gradient-Based Algorithms for Constrained Total Variation Image Denoising and Deblurring Problems," *IEEE Transactions on Image Processing*, vol. 18, no. 11, pp. 2419–2434, 2009.

[52] M. J. Muckley, D. C. Noll, and J. A. Fessler, "Fast parallel MR image reconstruction via B1-based, adaptive restart, iterative soft thresholding algorithms (BARISTA)." *IEEE transactions on medical imaging*, vol. 34, no. 2, pp. 578–88, 2015.

6

General discussion and conclusions

IMAGING in MR knows many facets that are all of great importance in order to acquire diagnostic valuable scans. Two of these facets have been addressed in this dissertation: improving the transmit magnetic field in an ROI using a well-designed dielectric pad in Part I, and reducing image reconstruction times using a preconditioner in Part II. This has led to the following key contributions:

1. A forward model that can be used to evaluate the pad induced electromagnetic fields by considering the dielectric pad as a small perturbation of a large computational static background model.

2. Reduction of the complexity of the forward model by parameterizing the model in the pad's characteristics and by using a projection-based model order reduction technique.

3. A pad design tool for finding an effective and practical dielectric pad for an arbitrary ROI in 3T body imaging and 7T neuroimaging applications.

4. Accelerating parallel imaging and compressed sensing reconstruction times in a Split Bregman framework using a circulant preconditioner.

PART I: DIELECTRIC PAD DESIGN

One of the main challenges of today in high-field MRI is to obtain an effective B_1^+ field in an ROI; such a field is characterized by a high transmit efficiency and a homogeneous distribution throughout the region to obtain an equally weighted contrast in the MR image. For strong background fields of 3T and higher, this condition cannot be taken for granted anymore, as it could for MR systems with a static field strength up to 1.5 T. Due to the increase in the RF resonance frequency for higher field strengths, wavelength effects occur that perturb this previously assumed homogeneous RF field. Dielectric pads can be used to overcome these interference effects, although their design needs to be determined carefully beforehand. Because designing a pad was previously a cumbersome and time consuming trial-and-error procedure, we have created an intuitive design tool that finds the optimum dielectric pad within minutes.

The backbone of the tool is a fast forward model for evaluating dielectric pads in a typical MR configuration: a heterogeneous body model, an RF coil and RF shield, and a pad. Such a configuration can be modeled in FDTD solvers, leading to very large discretized systems with 10^{6-7} unknowns when discretized with 20 points per wavelength in free space. For every pad we need to solve this entire system. A significant part of the computational domain is fixed, however, i.e. the body model, the RF coil, and the shield do not change when optimizing dielectric pads. Furthermore, the pad itself is relatively small compared to the full computational domain. We exploited these two properties by dividing the full computational domain into one domain that is static and one domain that is dynamic. This was achieved by defining a pad design domain that covers the body like a shell; every pad should be confined to this domain. To separate the static configuration part from the dynamic pad part, we set up a scattering formalism

using the Sherman-Morrison-Woodbury formula. The prerequisite for using this formalism is that the Green's tensor for an inhomogeneous background medium is computed first. Explicitly, we placed a Hertzian dipole on every grid-edge in the pad design domain and computed the field response for each of them. The responses were then stored in a configuration-dependent library. Although this is a time-consuming task and might take a week on a computer with two dedicated GPU's, it only has to be carried out once as it is pad independent. With the developed model, we can prescribe a permittivity and a conductivity to every edge in the design domain, after which only a small system needs to be solved. We tested the method for 7T head imaging for which the head coil is used for transmission, which let to significant speed up factors as the order was reduced from 10^{6-7} to 10^4. For a normal sized pad of about $18 \times 18 \times 1$ cm^3 computation times are decreased by a factor 30 and field solutions are obtained in about 10 seconds. The accuracy of the solution is not compromised, however, and relative errors were observed of at most 1% for regions where the B_1^+ is low.

The dielectric materials might couple to the birdcage coil when the pad's dimensions are large or if it is placed closely to the transmit coil. We have taken this coupling into account by having a resonant coil in the background configuration, i.e. capacitors are placed in the FDTD grid. In case the coil is detuned by the pad and it requires retuning, it will require a new library. Circuit-co-simulation can be used to overcome this problem. Explicitly, field responses are computed for the sources and the capacitors in the birdcage coil individually and subsequently the total field can be found by solving a subproblem coupling these separate responses [1, 2]. The current forward model can be easily incorporated, by computing the perturbation for each of these source/ capacitor field responses individually. The complexity of the method increases from $\mathcal{O}\left(N^3\right)$ to $\mathcal{O}\left(mN^3\right)$, where m is equal to the number of sources plus capacitors [3].

We applied reduced order modeling techniques to decrease the complexity of our forward model further for the reason that, in its current form, the model is not suitable for optimization. For optimization it is required to evaluate the entire pad design, i.e. computing the sensitivity for each grid-edge in the design domain. Whereas FDTD is very memory efficient and computational cheap, a direct solver from e.g. Matlab is not. As the direct solver's complexity scales as $\mathcal{O}\left(N^3\right)$ the forward model will defeat its purpose for large pads. Consequently, we reduced the model in a number of steps. First, the pad design domain was divided into subdomains. Every subdomain contains an accumulated set of grid edges over a volume of about 3500 mm^3 in contrast with the original 125 mm^3 resolution, hence reducing the resolution artificially. Second, the model was parameterized in terms of the pad's dimensions, location, and constitution. With these parameters we set material properties to the subdomains by using Heaviside unit step-functions instead of specifying the material properties at each grid edge separately. With these functions we restrict all modeled pads to be practically feasible, i.e. only rectangular and homogeneous pads are considered in our model order reduction approach. Finally, as the solution space is now decreased, we applied projection-based reduced order modeling to eliminate redundant data from the forward model. To this end, we simulated a large number of random dielectric pads with the parameterized model, and computed a singular value decomposition of the resulting currents in the pad design domain. The 25% most significant components were selected as projection matrix for

reducing the forward model. This led to a model of order 500 and computation times of 50 ms per dielectric pad evaluation, which decreases computation times by a factor 6000 compared with standard methods. The accuracy of the B_1^+ solutions decreases slightly, but can partly be controlled by the number of random pad simulations and the percentage of significant components that is taken into account. We found however that the B_1^+ results are sufficiently accurate to be applied in practice.

For optimal pad design, we defined a cost function that is to be minimized for the pad's parameters: namely its dimensions, location, and constitution. Using a least squares formalism where a target B_1^+ field can be defined for a given ROI, the residual between the modeled and targeted B_1^+ field can be minimized. We initially applied the Gauss-Newton algorithm to solve our non-linear least squares problem, in which the second order derivatives are approximated using first order information only. Explicitly, the Hessian matrix is computed using the Jacobian matrix, which in our case resulted in a rank deficient matrix and hence needed to be regularized. To this end we applied standard Tikhonov regularization with a regularization parameter that is determined experimentally. We found that the regularization parameter is generally dependent on the selected ROI. Hence, exploiting approximated second order information is not beneficial for a design tool that should work for any ROI. Consequently, we applied the gradient descent algorithm because of its simplicity and a proper step size could be found using a line-search, since our forward solver is very efficient.

Finally, a design tool was developed in Matlab that is supported by an intuitive graphical user interface. The tool offers the possibility to find a pad that either enhances the B_1^+ efficiency, its homogeneity, or a combination of both. This was achieved by carrying out a sweep over different target fields in a user-selected 3D volume of interest inside the head or the body. The result shows a clear overview of the efficiency-homogeneity combination, such that a desired pad can be selected within minutes due to fast forward modeling. In addition, as some imaging applications require two dielectric pads instead of one, we added this design option in the tool as well.

As the input of the design tool is a reduced order library, it can be easily replaced by other libraries to allow for other body models and other applications. When libraries are created for subjects with different dimensions and gender, the pad design solutions for each of these subjects can be easily and quickly compared. Such extensions will result in an even more flexible design tool. Possible library extensions that can be incorporated are libraries for 7T female neuroimaging, 3T body imaging using the female body model, and the male body model with a high body mass index. We have extended the library to pregnant body models in Appendix A, where a dielectric pad can be efficiently used to improve the B_1^+ field.

In addition, we like to point out that during library creation and testing, we found that the same reduced order library can be used for more applications than the one it was designed for. For example, the library that was designed for a birdcage excitation and a single dielectric pad can also be used to optimize the B_1^+ fields for two pads within the same configuration. This implies that the interactions between the two dielectric pads, the body, and the coils are taken into account in this library. Moreover, a given library can sometimes also be used for different body landmark positions in the birdcage coil, that is, the patient can be moved backwards and forwards in the coil to center a

specific landmark. The same model can be used, except that now the background field from the initial position needs to be replaced by a new background field as generated by the repositioned coil. Finally, we found that the birdcage excitation can be replaced afterwards by e.g. a local non-resonant coil element. Although the accuracy decreases slightly, the result is remarkable as the reduced order library is not created using a local coil element. Apparently, for all these applications, when finding the most significant current distributions in the pad design domain for random pad evaluations, we actually find the most significant modes that can occur within the pad.

The developed methods and the design tool can also be used for design problems that are more complex than the one from this dissertation. Non-rectangular multi-element pads can be included for example [4]. Furthermore, modeling electric fields to obtain safety information for patients with an implant or a deep brain stimulation requires complex RF simulations due to the required fine spatial resolution [5, 6]. As these devices are positioned slightly different in the body for each patient, different patient-specific electric field distributions are obtained and using the method outlined in Chapter 2, we can create a library for which the design domain is defined inside the body instead of outside the body as is the case for dielectric pads [7]. This will allow for the efficient modeling of these devices when combined with the reduced order modeling technique presented in this thesis. Finally, as parallel transmit and receive systems are used more frequently, we can optimize for multi-element dielectric pads, either incorporated in the antenna design or as an addition to existing antennas [8–11]. As the library is flexible towards other geometries and excitation fields, we can include non-resonant coil elements and find the resulting transmit B_1^+ or receiver B_1^- fields to evaluate transmit and receive sensitivity. Alternatively, as described above, we can model resonant coil elements in the configuration by using circuit-co-simulation.

In conclusion, we developed a tool that allows for optimal pad design within minutes for 3T body imaging and 7T neuroimaging applications. Furthermore, the described methods can also be fruitfully applied to many other design and field evaluation problems.

PART II: ACCELERATING RECONSTRUCTIONS

MR scan times can be strongly reduced using parallel imaging and compressed sensing techniques, which reduce the number of measurements such that part of k-space is not acquired. Consequently, the Nyquist criterion is violated and an image of the anatomy cannot be reconstructed anymore because aliasing or noise-like behavior occurs when a standard Fourier transformation is applied. Missing information from k-space can be restored by adding additional information to the system by exploiting the spatial sensitivity of the receiver coils and by the a priori knowledge that the anatomic image is sparse in some transform domain. Incorporating this information in a design problem can be easily done, but solving this problem requires more advanced techniques since ℓ_0 or ℓ_1-norm minimization problems need to be solved. The reconstruction times increase, since standard efficient Fourier transformation techniques can no longer be applied for undersampled data. Although undersampling is beneficial for the patient's comfort and it reduces motion artifacts, long reconstruction times are a drawback. We designed and implemented a preconditioner that can be used to speed up this reconstruction in a Split

Bregman framework.

The minimization problem that is to be solved can be addressed by a multitude of reconstruction algorithms. We chose the Split Bregman framework for its simplicity, stability, computational performance, and because of its frequent use. This method converts a single minimization problem into two subproblems. The first subproblem relaxes the ℓ_1-norm part of the minimization procedure and replaces it with a standard ℓ_2-norm minimization problem that can be solved by standard least-squares minimization techniques. The second subproblem contains the ℓ_1-norms that were relaxed before and these subproblems need to be solved subsequently to correct for the relaxation. Using an iterative scheme for the two combined subproblems, the initial minimization problem can be solved.

The ℓ_2-norm minimization problem was formulated as a linear least squares problem and was subsequently written as a system of linear equations $\mathsf{A}\mathbf{x} = \mathbf{b}$. The system matrix A contained three terms: the data fidelity term comprising the undersampling scheme and coil sensitivities, the total variation operator, and the wavelet operator. The latter two terms are known to have a sparse result when applied to the image. Iterative solvers are typically used to solve the system for the unknown image $\mathbf{x}$, since matrix-vector products with matrix A can be computed very efficiently. Long reconstruction times may result, however, especially when the number of unknowns is large (10^5 or higher). Fortunately, it is possible to significantly reduce these reconstruction times, since matrix A is not altered in the Split Bregman procedure and therefore may be preconditioned to accelerate convergence.

We designed such a preconditioner by exploiting the block circulant with circulant blocks structure (BCCB) of the total variation and the wavelet transform parts of the system matrix. This structure can be used efficiently as it can be diagonalized using two-dimensional Fourier transformations. The inverse of such a matrix can be easily computed as only a diagonal matrix is to be inverted. However, the data fidelity term, containing the measurements, sampling patterns, and coil sensitivities, does not possess this property. Hence, in the construction of our preconditioner we approximated only this non-BCCB part with a BCCB matrix. Explicitly, by multiplying the data fidelity term from the left and the right by the discrete Fourier matrix we try to diagonalize this term; the technique that is used to diagonalize a BCCB matrix. We found a closed-form expression that prescribes the diagonal of the resulting matrix and use this diagonal to create a BCCB matrix, i.e. we discarded all off-diagonal information. The closed-form solution contained only three FFTs and therefore could be efficiently computed. Because the preconditioner could be used throughout the entire Split Bregman framework, we only had to compute the approximation once for each reconstruction.

The required iterations to solve the system of linear equations decreased by a factor 5 without compromising the solution of SB, as preconditioners do not affect the solution, but solely enhance the convergence of the iterative solver used in the Split Bregman procedure. The total framework of SB was accelerated by a factor 2.5, which is caused by the additional ℓ_1-norm problems that need be minimized for every least squares solution. This factor can be increased, however, as we did not optimize these subproblems and we could have used more efficient wavelet transformations. The complexity of the Split Bregman algorithm was not increased much due to the preconditioner, as it only

requires two additional FFTs compared with the $2N_c$ FFTs that are already used when no preconditioning is applied, where N_c is the number of coil channels (typically larger than 8).

The preconditioner performs well for arbitrary k-space sampling patterns on a Cartesian grid and for different coil geometries and anatomies. For sampling on a non-Cartesian grid the current preconditioner can be used when gridding methods are used to map the non-uniform samples to a uniform grid [12, 13]. The preconditioner can be adapted for non-Cartesian trajectories as well by replacing the circulant structure of the matrix with a Toeplitz structure, i.e. with a block Toeplitz matrix with Toeplitz blocks [14]. We expect that this Toeplitz preconditioner will lead to a significant reduction in computation time given the encouraging results for the Cartesian case.

For all reconstruction methods, there are some regularization and reconstruction parameters that need to be tuned for fast convergence and accurate image reconstruction results. In the Split Bregman method the number of parameters is kept to a minimum to minimize this tuning problem. The parameters in our method were found manually by tuning them based on image quality and we found that the relative ratio between the parameters can be kept more or less the same. The order of magnitude of the parameters depends on the noise level of the data [15], however, as it serves as a threshold in the ℓ_1-norm minimization problems. Ideally, other methods could be used to find these parameters in a less heuristic manner [16–20].

In conclusion, the preconditioner leads to a 5-fold acceleration in solving the least squares problem in a Split Bregman reconstruction framework and results in a 2.5-fold acceleration in the total reconstruction time. As the preconditioner can be easily and effectively built because of its circulant structure, it is a suitable tool to accelerate the time-consuming PI and CS reconstruction times.

REFERENCES

[1] J. Paska, J. Fröhlich, D. O. Brunner, K. P. Pruessmann, and R. Vahldieck, "Field Superposition Method for RF Coil Design," in *Proceedings of the 17th Annual Scientific Meeting of the International Society for Magnetic Resonance in Medicine (ISMRM)*, Honolulu, HI, USA, 2009.

[2] R. A. Lemdiasov, A. A. Obi, and R. Ludwig, "A numerical postprocessing procedure for analyzing radio frequency MRI coils," *Concepts in Magnetic Resonance Part A*, vol. 38A, no. 4, pp. 133–147, 2011.

[3] W. M. Brink, J. Paska, J. Dai, J. H. F. van Gemert, G. Chen, G. C. Wiggins, R. F. Remis, C. M. Collins, and A. G. Webb, "Efficient Analysis of Dielectric Materials in Coupled RF Coil Configurations," in *Proceedings of the 25th Annual Scientific Meeting of the International Society for Magnetic Resonance in Medicine (ISMRM)*, Honolulu, HI, USA, 2017.

[4] R. Schmidt and A. G. Webb, "Improvements in RF Shimming in High Field MRI Using High Permittivity Materials With Low Order Pre-Fractal Geometries," *IEEE Transactions on Medical Imaging*, vol. 35, no. 8, pp. 1837–1844, 2016.

[5] C. Schmidt and U. van Rienen, "Modeling the Field Distribution in Deep Brain Stimulation: The Influence of Anisotropy of Brain Tissue," *IEEE Transactions on Biomedical Engineering*, vol. 59, no. 6, pp. 1583–1592, 2012.

[6] L. Angelone, J. Ahveninen, J. Belliveau, and G. Bonmassar, "Analysis of the Role of Lead Resistivity in Specific Absorption Rate for Deep Brain Stimulator Leads at 3T MRI," *IEEE Transactions on Medical Imaging*, vol. 29, no. 4, pp. 1029–1038, 2010.

[7] P. Stijnman, J. Tokaya, J. van Gemert, P. Luijten, J. Pluim, W. Brink, R. Remis, C. van den Berg, and A. Raaijmakers, "Calculation of the scattered RF field around implants within seconds using a low-rank inverse updating method," in *Submitted to: the 27th Annual Scientific Meeting of the International Society for Magnetic Resonance in Medicine (ISMRM)*, Montreal, QC, Canada, 2019.

[8] Q. X. Yang, S. Rupprecht, W. Luo, C. Sica, Z. Herse, J. Wang, Z. Cao, J. Vesek, M. T. Lanagan, G. Carluccio, Y.-C. Ryu, and C. M. Collins, "Radiofrequency field enhancement with high dielectric constant (HDC) pads in a receive array coil at 3.0T," *Journal of Magnetic Resonance Imaging*, vol. 38, no. 2, pp. 435–440, 2013.

[9] G. Haemer, M. Vaidya, C. Collins, D. Sodickson, and G. Wiggins, "Evaluation of a High Permittivity Helmet for Use as a Coil Former for an 8ch Transmit/Receive Array with Dodecahedral Symmetry," in *Proceedings of the 25th Annual Scientific Meeting of the International Society for Magnetic Resonance in Medicine (ISMRM)*, Honolulu, HI, USA, 2017.

[10] T. P. A. O'Reilly, T. Ruytenberg, and A. G. Webb, "Modular transmit/receive arrays using very-high permittivity dielectric resonator antennas." *Magnetic resonance in medicine*, vol. 79, no. 3, pp. 1781–1788, 2018.

[11] G. Carluccio, G. Haemer, V. Manushka, S. Rupprecht, Q. Yang,

and C. Collins, "SNR Evaluation for a high-permittivity dielectric helmet-shaped coil former for a 28 channel receive array," in *Proceedings of the 26th Annual Scientific Meeting of the International Society for Magnetic Resonance in Medicine (ISMRM)*, Paris, France, 2018.

[12] J. Jackson, C. Meyer, D. Nishimura, and A. Macovski, "Selection of a convolution function for Fourier inversion using gridding (computerised tomography application)," *IEEE Transactions on Medical Imaging*, vol. 10, no. 3, pp. 473–478, 1991.

[13] J. A. Fessler, "On NUFFT-based gridding for non-Cartesian MRI," *Journal of Magnetic Resonance*, vol. 188, no. 2, pp. 191–195, 2007.

[14] D. S. Weller, S. Ramani, and J. A. Fessler, "Augmented Lagrangian with variable splitting for faster non-Cartesian L1-SPIRiT MR image reconstruction." *IEEE Transactions on Medical Imaging*, vol. 33, no. 2, pp. 351–361, 2014.

[15] N. Galatsanos and A. Katsaggelos, "Methods for choosing the regularization parameter and estimating the noise variance in image restoration and their relation," *IEEE Transactions on Image Processing*, vol. 1, no. 3, pp. 322–336, 1992.

[16] J. P. Oliveira, J. M. Bioucas-Dias, and M. A. Figueiredo, "Adaptive total variation image deblurring: A majorizationminimization approach," *Signal Processing*, vol. 89, no. 9, pp. 1683–1693, 2009.

[17] S. Boyd, N. Parikh, E. Chu, B. Peleato, and J. Eckstein, "Distributed Optimization and Statistical Learning via the Alternating Direction Method of Multipliers," *Foundations and Trends® in Machine Learning*, vol. 3, no. 1, pp. 1–122, 2010.

[18] S. Ramani, Zhihao Liu, J. Rosen, J. Nielsen, and J. A. Fessler, "Regularization Parameter Selection for Nonlinear Iterative Image Restoration and MRI Reconstruction Using GCV and SURE-Based Methods," *IEEE Transactions on Image Processing*, vol. 21, no. 8, pp. 3659–3672, 2012.

[19] E. Ghadimi, A. Teixeira, I. Shames, and M. Johansson, "Optimal Parameter Selection for the Alternating Direction Method of Multipliers (ADMM): Quadratic Problems," *IEEE Transactions on Automatic Control*, vol. 60, no. 3, pp. 644–658, 2015.

[20] J. Chung and M. I. Español, "Learning regularization parameters for general-form Tikhonov," *Inverse Problems*, vol. 33, no. 7, p. 074004, 2017.

A

FETAL IMAGING USING DIELECTRIC PADS

The methods and the design tool from Part I of the thesis have been used to design dielectric pads for fetal MRI at 3T. One of the main concerns in fetal MRI is the amount of power that is deposited both in the fetus and the mother, which can expressed by the Specific Absorption Rate (SAR). In this chapter we show that well-designed pads can increase the homogeneity of the field while substantially reducing the SAR in both the mother and the fetus for models of the third, seventh, and ninth months of gestation.

This chapter is submitted to Magnetic Resonance in Medicine (under review).
(December, 2018)

A

A.1. INTRODUCTION

ALTHOUGH ultrasound (US) remains the predominant diagnostic imaging for evaluating disorders related to pregnancy, fetal MRI is increasingly being used. In contrast to ultrasound, MRI visualization of the fetus is not significantly limited by maternal obesity, fetal position, or oligohydramnios; in addition, visualization of the brain is not restricted by the ossified skull. Due to its superior soft tissue contrast, MRI is able to distinguish individual fetal structures such as lung, liver, kidney and bowel [1]. The extended field-of-view and ability to acquire oblique parallel slices aids examination of fetuses with large or complex anomalies, and visualization of any lesions within the context of the entire fetal body [2]. In particular, studies of the fetal brain and general central nervous systems (CNS) disorders are increasing in number and diagnostic quality [3].

Fetal MRI is mainly performed at 1.5T, but there is a growing interest in 3T [4–6]. The increase in field strength results in an increase in signal-to-noise ratio (SNR), which is beneficial as the spatial resolution can be increased and the acquisition times can be reduced. Acquiring high quality images is more challenging, however, as for higher field strength the wavelength of the RF field is reduced. Consequently, interference effects occur that decrease the uniformity and efficiency of the RF transmit field (B_1^+) and hence the image quality is degraded [7–9].

Another concern in fetal MR is the amount of power deposited in the fetus, as well as the mother, particularly with respect to the presence of very high conductivity amniotic fluid. As discussed in Murbach et al. [10] the allowed specific absorption rate (SAR) is defined by the International Electrotechnical Commission (IEC) standards in terms of whole-body SAR (SAR_{wb}), and head-averaged SAR. IEC 60601-2-33 suggests that pregnant women should undergo only scans which are performed in normal operating mode which limits the SAR_{wb} to 2 W/kg. For this operating mode, the local SAR_{10g} (the SAR averaged over any 10 g of tissue) is limited to 10 W/kg when local transmit coils or RF shimmed body coils are used.

A number of previous studies have investigated via electromagnetic (EM) simulations the SAR experienced both by the mother and the fetus at 1.5T and 3T [10–15]. Hand et al. [11, 12] and Pediaditis et al. [13] used a finite integration technique (FIT): the former considered a truncated model of a 28-week pregnant woman at 1.5T and 3T, while the latter looked at a whole-body 30-week pregnant female model at fields between 0.3T and 4T. Both studies showed that local SAR_{10g} in the mother exceeded 10 W/kg before the maternal whole-body averaged SAR reached 2 W/kg. Other studies have used finite difference time domain (FDTD) methods for their simulations at 1.5T and 3T. Wu et al. [14] considered pregnant female models from 1 to 9 months gestation and determined that the local SAR_{10g} within the mother exceeded the limit of 10 W/kg at both field strengths. Other researchers have studied the effects of small changes in position of the fetus with respect to the center of the transmitting RF coil, and found relatively small (<10%) differences in SAR.

Some studies have extended the SAR analysis to also estimate temperature increases within the mother and fetus [10, 12]. These two studies used the Pennes Bioheat equation [16] and the thermoregulation model presented by Laakso et al. [17], respectively. In the most recent simulation study, Murbach et al. investigated the effect of using RF-shimming on a dual-transmit 3T system in terms of the SAR and temperature rise both in

the mother and fetus at different gestational stages [10]. They used models in the third, seventh and ninth month of gestation [15, 18] with appropriate dielectric properties derived from Gabriel et al. [19]. Their general conclusions were that RF shimming can reduce the local RF exposure for the mother, but conversely can increase the whole-body exposure and peak temperature in the fetus.

Another method to tailor the transmit field and SAR distribution is passive RF shimming using high permittivity materials. For 3T applications, these materials typically have a relative permittivity on the order of 300-1000, and function by inducing a strong secondary magnetic field in their vicinity. Several studies performed in adults at 3T have reported a higher B_1^+ efficiency and/or homogeneity, as well as reduced SAR values [20–27]. The potential benefits of using high permittivity materials in fetal MRI have been indicated previously [28, 29] but these pads were not optimized and the different gestational stages were not taken into account. In general, for passive RF shimming the dimensions, location, and constitution of the high permittivity material need be optimized in an application-specific manner. A common approach is to perform a parametric optimization study using electromagnetic field solvers, based on a systematic trial-and-error approach. As each of these simulations involve a heterogeneous body model and a detailed model of the RF coil, such procedures typically take multiple days for a single application. In previous work, we have developed an advanced reduced order modeling technique to accelerate pad evaluations by characterizing stationary components such as the RF coil and body model in an offline-stage, and compressing the resulting model. This yielded up to four orders of magnitude of acceleration compared to commercial software, and enabled the automated design of dielectric pads in under a minute [30].

In this paper we use the design approach described above to investigate the utility of using high permittivity materials in fetal imaging. Following the general procedures and guidelines of previous simulation studies, we assess the B_1^+ efficiency, B_1^+ homogeneity and the SAR in different areas of the mother and fetus for different gestational stages as well as positions/orientations within the RF coil. We also performed a sensitivity analysis to estimate the effects of slight position changes of the pads.

A.2. METHODS

CONFIGURATION

For the EM simulations a wide-bore high-pass birdcage body coil was used with a diameter of 750 mm, and a shield diameter of 800 mm. The shielded coil was tuned to operate in quadrature mode at a frequency of 128 MHz using 33.25 pF capacitators in the end rings. Female body models from the Virtual Family dataset [18] in the third, seventh, and ninth month of gestation (with the fetus positioned head-down) were incorporated either on a 7.5 mm or a 3.75 mm discretized uniform grid for B_1^+ field simulations and SAR evaluations, respectively. A resolution of 7.5 mm was sufficient to accurately model the B_1^+ fields. For the SAR simulations we used the higher spatial resolution grid in order to incorporate the isolating material around the dielectric pad. The region in which high permittivity materials can be placed, referred to as the “pad design domain”, was defined as a 1.5 cm thick layer enclosing the body model from groin to breast as illustrated in Figure A.1. The pregnant body models can be shifted in the body coil such that differ-

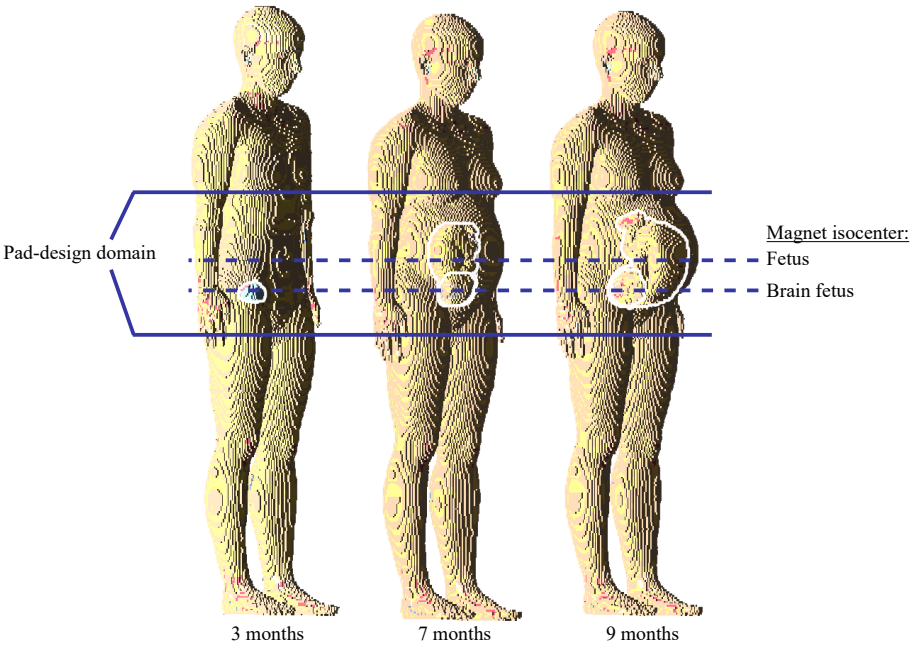

Figure A.1: Pregnant body models in the third, seventh, and ninth month of gestation. The pad design domain is the region to which every dielectric pad is confined. The imaging landmarks are shown on the right-hand side: the center and the brain of the fetus.

ent ROIs can be positioned in the magnet isocenter. All field quantities were computed using XFdtd software (v.7.4.0.3, Remcom State College, PA, USA) and were normalized to 1 W input power.

DESIGNING DIELECTRIC PADS

An efficient forward model was used to evaluate the electromagnetic fields with a dielectric pad in place as described in [27, 31]. (A dielectric pad design tool encompassing the methods summarized below is freely available at https://paddesigntool.sourceforge.io). To this end, the computational domain was divided into a domain that is stationary, i.e. containing the heterogeneous body model and RF transmit coil, and a domain that is dynamic, i.e. the pad design domain. The design domain allows defining dielectric pads with any location, geometry, and constitution, provided that the pad is confined within this domain. For every pad simulation, the stationary components remain unaffected and hence they can be characterized in advance by computing the pad-independent background fields and by constructing the so-called field response library. Subsequently, only the perturbation due to the dielectric pad on the stationary electromagnetic fields needs to be computed. As the pad design domain is small with respect to the original full computational domain, only a small problem needs to be solved and hence the computational times for dielectric pad evaluations are accelerated.

The computational times were accelerated further by applying a reduced order mod-

eling technique [30]. In this method, the degrees-of-freedom for the dielectric pad are restricted to reduce the solution space and the complexity of the model. For that reason, the forward model was parameterized in terms of the pad's width, height, location, and constitution by the parameter vector $\mathsf{p} = [\varepsilon; \text{width}, \text{height}, \text{location}]$. The parameter vector also allows for the definition of two dielectric pads. Furthermore, the pad design domain was divided into small dielectric subdomains by assigning the same material properties to grid edges that belong to a given non-overlapping homogeneous subdomain. To exploit the reduced solution space due to the subdomains and the parameterization, we subsequently created a reduced order basis by simulating a large variety of dielectric pads using the parameterized model (i.e. snapshots) after which the most dominant current modes in the pad design domain were extracted to serve as a basis. Finally, the forward model was compressed by projecting the field library onto this reduced order basis. This allows for field computations that are up to four orders of magnitude faster than conventional EM solvers such as XFdtd.

The dielectric pads were designed by optimizing the B_1^+ field in a given region-of-interest (ROI) for a certain dielectric pad parameter vector p. This was achieved by minimizing a cost functional $C(\mathsf{p})$ that measures the discrepancy between the desired B_1^+ magnitude and the modeled B_1^+ magnitude within the ROI, defined as

$$C(\mathsf{p}) = \frac{1}{2} \frac{\|\mathsf{B}_1^+(\mathsf{p}) - \mathsf{B}_1^{+;\text{desired}}\|_{2;\text{ROI}}^2}{\|\mathsf{B}_1^{+;\text{desired}}\|_{2;\text{ROI}}^2}, \tag{A.1}$$

where $\mathsf{B}_1^{+;\text{desired}}$ is the desired B_1^+ magnitude, $\mathsf{B}_1^+(\mathsf{p})$ is the B_1^+ magnitude due to a pad with model parameters p, and $\|\cdot\|_{2;\text{ROI}}^2$ denotes the ℓ_2 norm over the ROI. The B_1^+ efficiency is measured in units of $\mu\text{T}/\sqrt{\text{W}}$ input power, and the B_1^+ homogeneity as the coefficient of variation C_v over the ROI. The cost functional was minimized for a range of desired B_1^+ magnitudes, each of which yields a different solution in terms of transmit efficiency and C_v. With these solutions, a trade-off between homogeneity and efficiency can be made, depending upon the particular imaging sequences to be used.

All pad optimizations in this study were performed while fixing the pad thickness to 1.5 cm, electrical conductivity to 0.2 S/m, maximum relative permittivity to 300, and constraining the width and length of the pad to 30 cm in order to limit the weight of the pad.

B_1^+ AND SAR EVALUATION SCENARIOS

The B_1^+ and SAR effects were evaluated for two ROIs: (i) the entire 3D volume of the fetus and (ii) the fetal brain only. For each evaluation the midpoint of the ROI was positioned at the magnet isocenter. The cost functional of Eq. (A.1) was minimized for a range of desired B_1^+ magnitudes, first for one pad and subsequently for two pads. The pad designs that provided the optimum transmit efficiency and the optimum field homogeneity were then analyzed in terms of SAR after normalizing the input power to 1 W. The SAR distribution was evaluated in terms of the SAR_wb, average SAR in the fetus and amniotic fluid (SAR_avg), and maximum 10g-averaged SAR ($\text{SAR}_{10\text{g,max}}$) in the mother, fetus and amniotic fluid. Furthermore, we evaluated the SAR effects after normalizing to the B_1^+ magnitude achieved in the ROI when no dielectric pad is being used.

Finally, for the optimized pads a sensitivity analysis was performed to determine how the transmit efficiency and homogeneity would be affected by a shift in the location of the pad from its calculated optimum, as this might occur in practice. To this end, the optimized pad was shifted by ~3 cm in each direction (horizontally, vertically as well as diagonally), after which the performance metrics were compared.

A.3. RESULTS

The pad design results in the three pregnant body models are shown in Figure A.2. The range of desired B_1^+ magnitudes considered in each of the optimizations was based on the B_1^+ magnitude without a dielectric pad, defining its lower limit, and the maximum achievable magnitude, found by running one optimization with a very high desired B_1^+ magnitude. In all cases a dielectric pad was obtained which improved the transmit efficiency in the ROI. Transmit efficiency gains measured 45% in the 3 months model, 50% in the 7 months model, and 26% in the 9 months model for both the fetal brain alone and the entire fetal volume. The C_v improved in all cases except for the 9 months model (ROI: entire fetus). In this case, the C_v was found to be relatively invariant to the target B_1^+ magnitude, while the transmit efficiency was improved by 27%.

SAR effects were evaluated for the dielectric pads that provided the minimum C_v and the maximum transmit efficiency, as indicated by the green and orange circles in Figure A.2, respectively. Note that for the 9 months (ROI: fetus) pad design number 2 was selected as the optimum solution as opposed to number 1, for the reason that a higher transmit efficiency was obtained with respect to a negligible increase in C_v. Specifications on the optimized pads can be found in Table A.2, where the number of pads (one or two) and the pads geometry and relative permittivity are also listed. In the majority of cases a single dielectric pad was suggested, positioned on the anterior side of the mother. A second pad on the posterior side improved the result only in the 9 months (ROI: brain) and 3 months cases.

The B_1^+ fields and the SAR distributions for the optimized pads are shown in Figures A.3 and A.4, and maximum SAR values are summarized in Table A.2 (including the results for the pads that provided the minimum C_v). The spatial distribution of the $SAR_{10g}$was very similar to that without dielectric pads, which is consistent with previous studies [21, 24, 26]. In the third and sixth column of Figure 3, the B_1^+ normalized SAR_{10g}distribution is shown for the case with dielectric pads.

For all SAR evaluations we observe a decrease in $SAR_{wb}$when optimized pads are in place. Specifically, the $SAR_{wb}$was reduced by more than 53%, 55%, and 31% for the third, seventh, and ninth months of gestation, respectively. For the pads that minimized C_v the reductions in SAR_{wb}were slightly lower, i.e. 53%, 51% and 23%. The $SAR_{avg}$and $SAR_{10g,max}$were reduced in almost all cases, except for the 9 months case where the pad was optimized to achieve a minimum C_v. Here, we observed an increased $SAR_{10g,max}$in the fetus of 6%-14%, but these values are still below 10 W/kg limit. The largest reductions in SAR are generally observed in the mother. For the 9 months model the amniotic fluid showed intermediate reductions and only small variations were observed in the fetus. In the other models, similar gains were observed in the fetus and the amniotic fluid.

The results from the sensitivity analysis showed that the performance metrics of the optimized dielectric pads are quite robust to small changes in the optimum location of

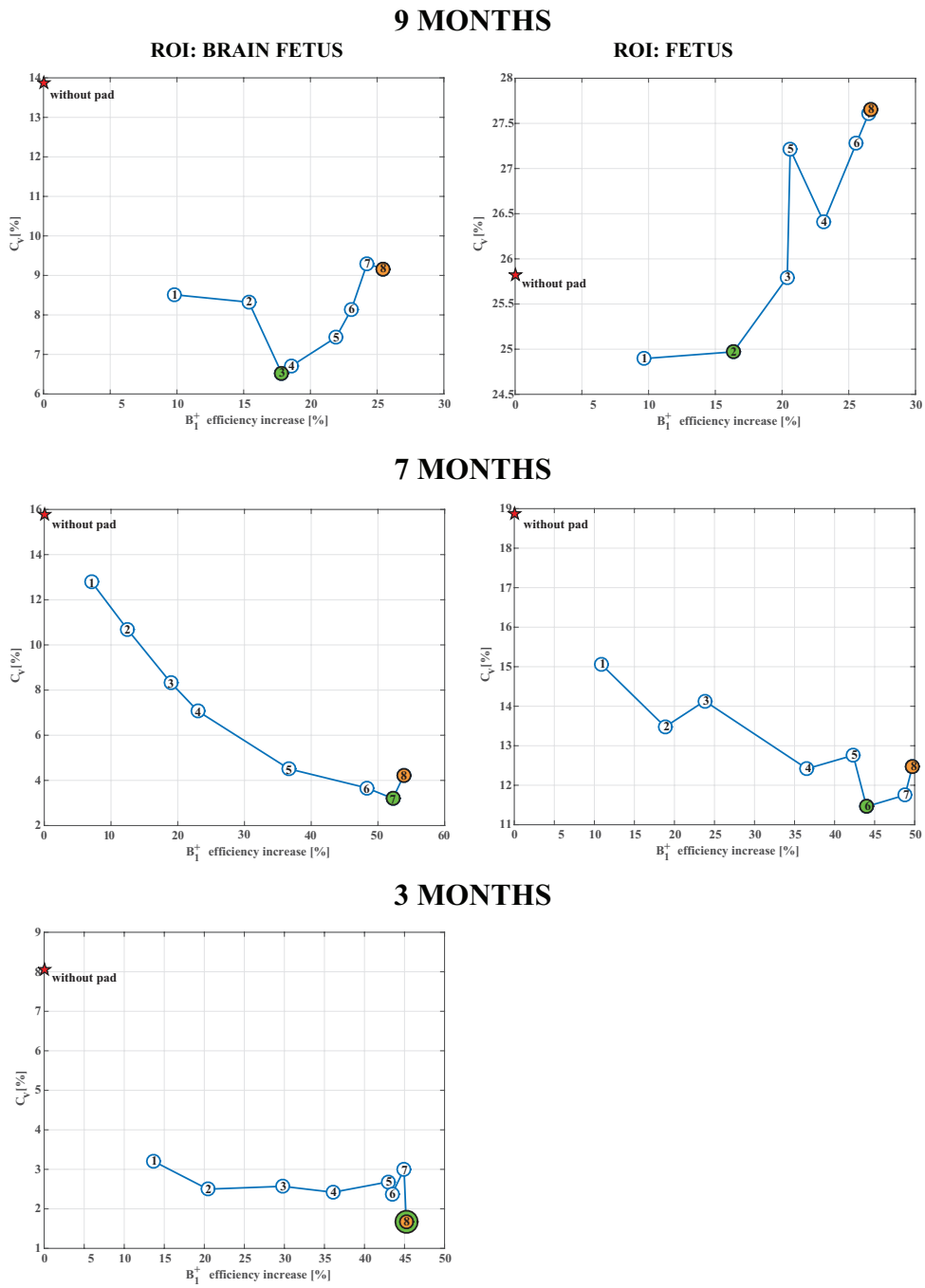

Figure A.2: Sweep results for the three, seven, and nine months of gestation. The ROI is set to the brain of the fetus (left column) and the fetus (right column). For each sweep the optimization algorithm was run several times using different desired B_1^+ fields. The green and orange circles indicate the cases that gave the minimum C_V and maximum transmit efficiency, respectively.

Table A.1: Summary of the B_1^+ transmit efficiency gains and the C_v with respect to the case without a dielectric pad. Results are compared for the dielectric pad that optimizes the efficiency of the field and the homogeneity of the field

Configuration	Transmit efficiency ($\mu T/\sqrt{W}$)	C_v (%)	Anterior pad	Posterior pad
9 months				
Fetal brain				
No dielectric pads	0.143	13.9		
Pad best B_1^+ efficiency	0.179 **(+25.4%)**	9.16	ε_r = 300, 18.2 x 27.9 x 1.5 cm^3	ε_r = 281, 29.4 x 26.6 x 1.5 cm^3
Pad best C_v	0.168 **(+17.8%)**	6.53	ε_r = 300, 18.1 x 25.6 x 1.5 cm^3	ε_r = 300, 18.0 x 27.9 x 1.5 cm^3
Fetal average				
No dielectric pads	0.109	25.8		
Pad best B_1^+ efficiency	0.138 **(+26.6%)**	27.7	ε_r = 300, 29.2 x 29.2 x 1.5 cm^3	
Pad best C_v	0.127 **(+16.4%)**	25.0	ε_r = 248, 24.7 x 29.2 x 1.5 cm^3	
7 months				
Fetal brain				
No dielectric pads	0.161	15.8		
Pad best B_1^+ efficiency	0.248 **(+53.9%)**	4.23	ε_r = 300, 29.3 x 28.3 x 1.5 cm^3	
Pad best C_v	0.245 **(+52.2%)**	3.20	ε_r = 300, 29.3 x 28.3 x 1.5 cm^3	
Fetal average				
No dielectric pads	0.131	18.9		
Pad best B_1^+ efficiency	0.196 **(+49.7%)**	12.5	ε_r = 300, 29.2 x 29.9 x 1.5 cm^3	
Pad best C_v	0.189 **(+44.0%)**	11.5	ε_r = 270, 29.2 x 29.9 x 1.5 cm^3	
3 months				
Fetal brain				
No dielectric pads	0.209	8.05		
Pad best B_1^+ eff. and C_v	0.303 **(+45.2%)**	1.67	ε_r = 257, 24.9 x 15.6 x 1.5 cm^3	ε_r = 300, 29.4 x 29.3 x 1.5 cm^3

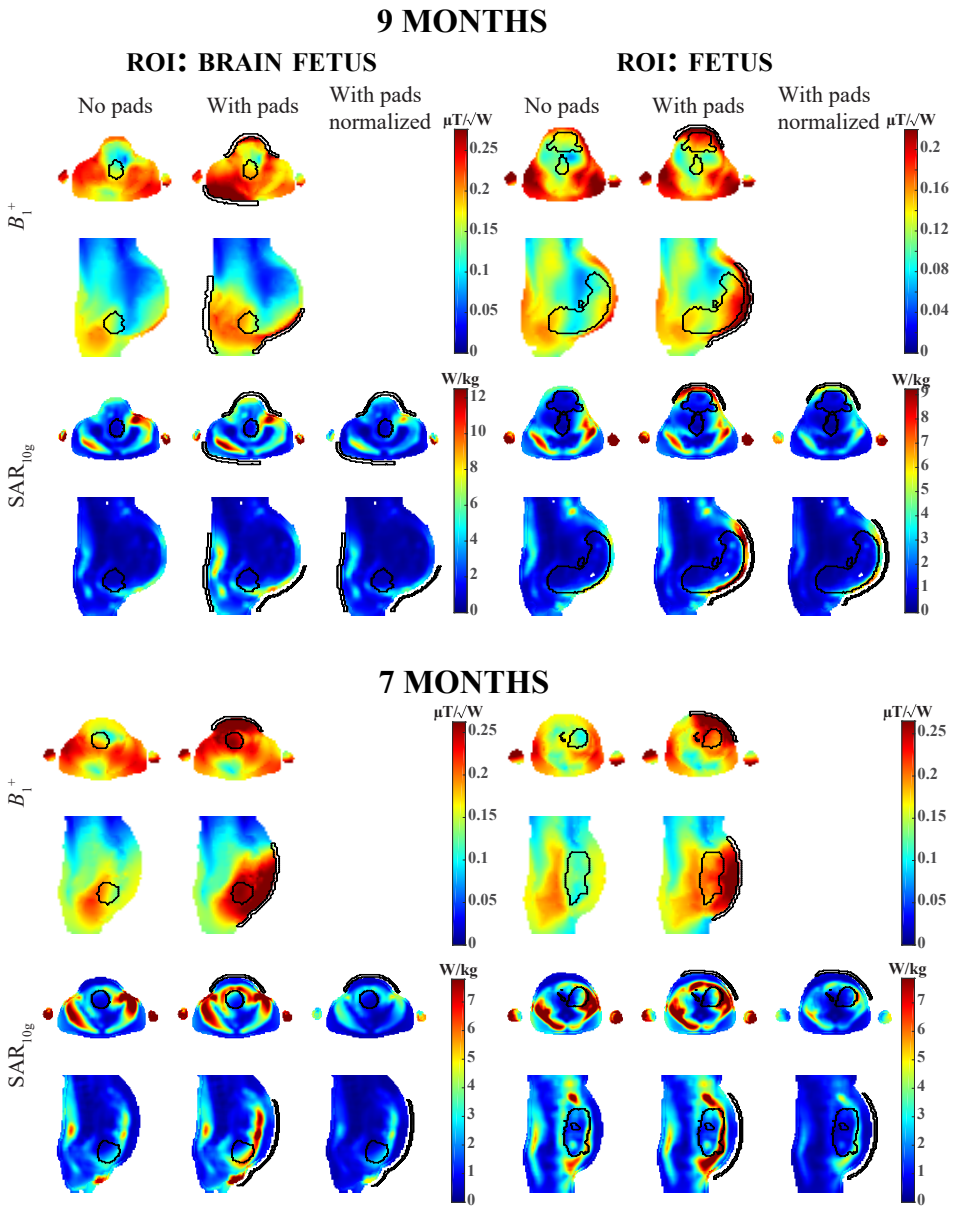

Figure A.3: B_1^+ fields and SAR evaluations the for the seven, and nine months of gestation. The first and fourth column are the results without any dielectric pad for the ROI set to the brain of the fetus and the fetus, respectively. The second and fifth column depict the results with dielectric pad, and the third and sixth column the results when normalized for the B_1^+ , i.e. the same transmit efficiency in the ROI is achieved as in the case without dielectric pads.

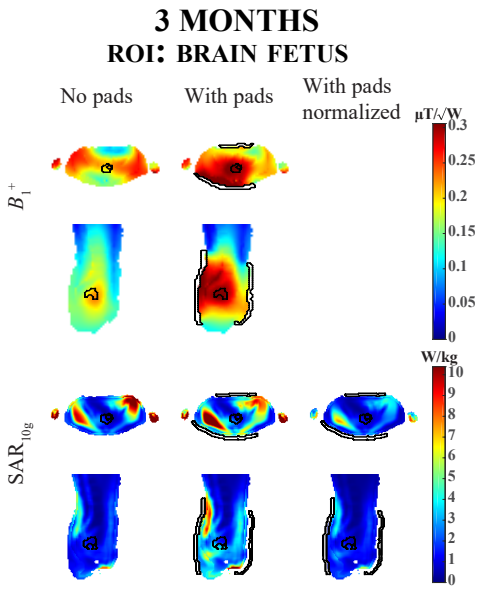

Figure A.4: B_1^+ fields and SAR evaluations the for the three months of gestation. The first column is the results without any dielectric pad for the ROI set to the brain of the fetus. The second column depicts the results with dielectric pad, and the third the results when normalized for the B_1^+ , i.e. the same transmit efficiency in the ROI is achieved as in the case without dielectric pads.

the pad, consistent with previous findings [24]. For the transmit efficiency we found a maximum degradation of 6.7%, 6.0% and 7.4% with respect to the optimum, for the three, seven, and nine months gestational age, respectively. By averaging the metrics over all directional shifts, we found that the efficiency is degraded by 2.5%, 1.9%, and 1.7%. The C_v is increased by a maximum of 1.7%, 3.7%, and 2.3% for the three, seven, and nine months gestational age, respectively. On average these values are 0.4%, 1.3%, and 0.7%.

A.4. DISCUSSION AND CONCLUSIONS

In this study we have simulated the effects of optimized dielectric pads on the transmit field and SAR distribution in fetal imaging at 3T. Our results show that, in general, considerable increases in both transmit efficiency and homogeneity as well as reductions in SAR can be obtained using this approach.

IEC 60601-2-33 suggests that pregnant women should only undergo scans which are performed in normal operating mode which limits the $SAR_{wb}$to 2 W/kg. In our study, we stay within this limit for all scenarios while improving the quality of the B_1^+ field at the same time. Although we are not bound to a $SAR_{10g,max}$limit of 10 W/kg, which only applies to local transmit coils or RF-shimmed body coils, we see that in the fetus we do not exceed 8.3 W/kg when using the dielectric pads. The local SAR is also reduced for the amniotic fluid when the pads are used. This is beneficial, as a higher SAR in this

Table A.2: Summary of the SAR evaluations. All percentages in the avgSAR and psSAR$_{10g}$ columns are with respect to the original configuration, i.e. where no dielectric pads are being used.

Configuration	SAR$_{wb}$ (W/kg)	SAR$_{avg}$ (W/kg)		SAR$_{10g,max}$ (W/kg)		
		Fetus	Amniotic	Mother	Fetus	Amniotic
9 months						
Fetal brain						
No dielectric pads	2.00	1.04	2.65	25.4	7.11	15.3
Pad best B_1^+ efficiency	1.39 **(-31%)**	0.88 **(-15%)**	1.90 **(-28%)**	15.6 **(-38%)**	6.49 **(-9%)**	10.1 **(-34%)**
Pad best C_v	1.55 **(-23%)**	1.03 **(-1%)**	2.22 **(-16%)**	18.4 **(-27%)**	8.13**(+14%)**	10.8 **(-30%)**
Fetal average						
No dielectric pads	2.00	1.01	2.80	29.3	7.48	15.1
Pad best B_1^+ efficiency	1.15 **(-42%)**	0.92 **(-9%)**	2.08 **(-26%)**	15.6 **(-47%)**	6.75 **(-10%)**	8.08 **(-47%)**
Pad best C_v	1.47 **(-27%)**	1.04 **(+3%)**	2.52 **(-10%)**	19.4 **(-34%)**	7.91 **(+6%)**	12.0 **(-20%)**
7 months						
Fetal brain						
No dielectric pads	2.00	2.00	4.35	19.8	12.8	13.7
Pad best B_1^+ efficiency	0.86 **(-57%)**	1.18 **(-41%)**	2.66 **(-39%)**	7.47 **(-62%)**	5.54 **(-57%)**	6.01 **(-56%)**
Pad best C_v	0.88 **(-56%)**	1.24 **(-38%)**	2.80 **(-36%)**	7.73 **(-61%)**	5.93 **(-54%)**	6.41 **(-53%)**
Fetal average						
No dielectric pads	2.00	2.32	5.02	24.4	14.9	16.1
Pad best B_1^+ efficiency	0.91 **(-55%)**	1.48 **(-36%)**	3.50 **(-30%)**	8.88 **(-64%)**	7.79 **(-48%)**	8.52 **(-47%)**
Pad best C_v	0.98 **(-51%)**	1.57 **(-32%)**	3.64 **(-28%)**	9.73 **(-60%)**	8.30 **(-44%)**	9.09 **(-44%)**
3 months						
Fetal brain						
No dielectric pads	2.00	1.6	1.32	22.1	2.68	2.91
Pad best B_1^+ eff. and C_v	0.94 **(-53%)**	1.33 **(-17%)**	1.13 **(-14%)**	9.66 **(-56%)**	2.03 **(-24%)**	2.04 **(-30%)**

non-perfused fluid may indirectly lead to an increased temperature in the fetus [10]. In all cases, however, we see that the SAR_{10g},max in the mother exceeds 10 W/kg before the SAR_{wb}limit is reached, as has also been found in other studies in pregnant models [13, 14] as well as non-pregnant models [15].

In the current design study, for practical reasons, we have restricted both the dimensions as well as the relative permittivity of the pad. Higher transmit efficiency gains are attainable when we relax these constraints. For example, the transmit efficiency can be increased by up to 36% for the 9 months (ROI: fetus) model instead of the 27% reported here, however, this would require a dielectric pad of size $30 \times 30 \times 1.5$ cm^3 with a relative permittivity of 453. Such a pad would exceed 15 kg in weight, which is impractical. Our constraints ensure that the weight of the dielectric pad stays below 4 kg, which is considered a suitable limit in order to preserve subject comfort based on previous experience at our institute.

The results shown here suggest that the use of dielectric pads could complement RF shimming as studied by Murbach et al. [10]. In some cases, the dielectric pads may in fact provide a larger improvement in B_1^+ efficiency and homogeneity than conventional RF shimming, which was also observed in other applications [24]. For example, in the seven months model RF shimming yielded a 15% increase in transmit efficiency (optimum B_1^+ efficiency shim settings) and a small improvement in C_v from 18% to 16% (optimum C_v shim settings). In our current study, using the same model, an increase in transmit efficiency of 50% (optimum B_1^+ efficiency) was obtained with an improvement in C_v from 19% to 12% (optimum C_v).

We note that compared to the Murbach study we observe slightly different SAR results for the 7 months configuration where no shimming is applied and where no dielectric pads are used. These differences may be caused by differences in either the coil model or the subject meshing; our pregnant models were limited to a uniform and isotropic spatial resolution of 5 mm, whereas the model from Murbach et al. supported a higher spatial resolution. These differences should however not change the conclusions with respect to the relative effects of the dielectric materials, which are relatively independent from the reference model.

In conclusion, we have shown that optimized high permittivity pads can reduce SAR in the third, seventh, and ninth month of gestation, while improving the transmit field homogeneity in the fetus. This offers a practical solution to improve image quality and RF safety in fetal MRI examinations at 3T.

REFERENCES

[1] M. C. Frates, A. J. Kumar, C. B. Benson, V. L. Ward, and C. M. Tempany, "Fetal Anomalies: Comparison of MR Imaging and US for Diagnosis," *Radiology*, vol. 232, no. 2, pp. 398–404, aug 2004.

[2] S. N. Saleem, "Fetal MRI: An approach to practice: A review," *Journal of Advanced Research*, vol. 5, no. 5, pp. 507–523, sep 2014.

[3] L. Manganaro, S. Bernardo, A. Antonelli, V. Vinci, M. Saldari, and C. Catalano, "Fetal MRI of the central nervous system: State-of-the-art," *European Journal of Radiology*, vol. 93, pp. 273–283, aug 2017.

[4] U. Krishnamurthy, J. Neelavalli, S. Mody, L. Yeo, P. K. Jella, S. Saleem, S. J. Korzeniewski, M. D. Cabrera, S. Ehterami, R. O. Bahado-Singh, Y. Katkuri, E. M. Haacke, E. Hernandez-Andrade, S. S. Hassan, and R. Romero, "MR imaging of the fetal brain at 1.5T and 3.0T field strengths: comparing specific absorption rate (SAR) and image quality," *Journal of Perinatal Medicine*, vol. 43, no. 2, pp. 209–20, jan 2015.

[5] T. Victoria, A. M. Johnson, J. C. Edgar, D. M. Zarnow, A. Vossough, and D. Jaramillo, "Comparison Between 1.5-T and 3-T MRI for Fetal Imaging: Is There an Advantage to Imaging With a Higher Field Strength?" *American Journal of Roentgenology*, vol. 206, no. 1, pp. 195–201, jan 2016.

[6] C. Weisstanner, G. M. Gruber, P. C. Brugger, C. Mitter, M. C. Diogo, G. Kasprian, and D. Prayer, "Fetal MRI at 3Tready for routine use?" *The British Journal of Radiology*, vol. 90, no. 1069, p. 20160362, jan 2017.

[7] M. Bernstein, J. Huston, and H. Ward, "Imaging artifacts at 3.0 T," *Journal of Magnetic Resonance Imaging*, vol. 24, no. 4, pp. 735–746, 2006.

[8] K. Chang and I. Kamel, "Abdominal imaging at 3T: Challenges and solutions," *Applied Radiology*, vol. 39, no. 10, p. 22, 2010.

[9] O. Dietrich, M. Reiser, and S. Schoenberg, "Artifacts in 3-T MRI: physical background and reduction strategies." *European Journal of Radiology*, vol. 65, no. 1, pp. 29–35, 2008.

[10] M. Murbach, E. Neufeld, T. Samaras, J. Córcoles, F. J. Robb, W. Kainz, and N. Kuster, "Pregnant women models analyzed for RF exposure and temperature increase in 3T RF shimmed birdcages," *Magnetic Resonance in Medicine*, vol. 77, no. 5, pp. 2048–2056, 2017.

[11] J. Hand, Y. Li, E. Thomas, M. Rutherford, and J. Hajnal, "Prediction of specific absorption rate in mother and fetus associated with MRI examinations during pregnancy," *Magnetic Resonance in Medicine*, vol. 55, no. 4, pp. 883–893, apr 2006.

[12] J. W. Hand, Y. Li, and J. V. Hajnal, "Numerical study of RF exposure and the resulting temperature rise in the foetus during a magnetic resonance procedure," *Physics in Medicine and Biology*, vol. 55, no. 4, pp. 913–930, 2010.

[13] M. Pediaditis, N. Leitgeb, and R. Cech, "RF-EMF exposure of fetus and mother during magnetic resonance imaging." *Physics in medicine and biology*, vol. 53, no. 24, pp. 7187–95, 2008.

A

[14] D. Wu, S. Shamsi, J. Chen, and W. Kainz, "Evaluations of Specific Absorption Rate and Temperature Increase Within Pregnant Female Models in Magnetic Resonance Imaging Birdcage Coils," *IEEE Transactions on Microwave Theory and Techniques*, vol. 54, no. 12, pp. 4472–4478, dec 2006.

[15] M. Murbach, E. Cabot, E. Neufeld, M.-C. Gosselin, A. Christ, K. P. Pruessmann, and N. Kuster, "Local SAR enhancements in anatomically correct children and adult models as a function of position within 1.5 T MR body coil," *Progress in Biophysics and Molecular Biology*, vol. 107, no. 3, pp. 428–433, dec 2011.

[16] H. H. Pennes, "Analysis of Tissue and Arterial Blood Temperatures in the Resting Human Forearm," *Journal of Applied Physiology*, vol. 1, no. 2, pp. 93–122, aug 1948.

[17] I. Laakso and A. Hirata, "Dominant factors affecting temperature rise in simulations of human thermoregulation during RF exposure," *Physics in Medicine and Biology*, vol. 56, no. 23, pp. 7449–7471, dec 2011.

[18] A. Christ, W. Kainz, E. G. Hahn, K. Honegger, M. Zefferer, E. Neufeld, W. Rascher, R. Janka, W. Bautz, J. Chen, B. Kiefer, P. Schmitt, H.-P. Hollenbach, J. Shen, M. Oberle, D. Szczerba, A. Kam, J. W. Guag, and N. Kuster, "The Virtual Familydevelopment of surface-based anatomical models of two adults and two children for dosimetric simulations," *Physics in Medicine and Biology*, vol. 55, no. 2, pp. N23–N38, 2010.

[19] S. Gabriel, R. W. Lau, and C. Gabriel, "The dielectric properties of biological tissues: II. Measurements in the frequency range 10 Hz to 20 GHz," *Physics in Medicine and Biology*, vol. 41, no. 11, pp. 2251–2269, nov 1996.

[20] Q. X. Yang, J. Wang, J. Wang, C. M. Collins, C. Wang, and M. B. Smith, "Reducing SAR and enhancing cerebral signal-to-noise ratio with high permittivity padding at 3 T," *Magnetic Resonance in Medicine*, vol. 65, no. 2, pp. 358–362, 2011.

[21] P. de Heer, W. M. Brink, B. J. Kooij, and A. G. Webb, "Increasing signal homogeneity and image quality in abdominal imaging at 3 T with very high permittivity materials," *Magnetic Resonance in Medicine*, vol. 68, no. 4, pp. 1317–1324, 2012.

[22] W. Luo, M. T. Lanagan, C. T. Sica, Y. Ryu, S. Oh, M. Ketterman, Q. X. Yang, and C. M. Collins, "Permittivity and performance of dielectric pads with sintered ceramic beads in MRI: early experiments and simulations at 3 T," *Magnetic Resonance in Medicine*, vol. 70, no. 1, pp. 269–275, jul 2013.

[23] Q. X. Yang, S. Rupprecht, W. Luo, C. Sica, Z. Herse, J. Wang, Z. Cao, J. Vesek, M. T. Lanagan, G. Carluccio, Y.-C. Ryu, and C. M. Collins, "Radiofrequency field enhancement with high dielectric constant (HDC) pads in a receive array coil at 3.0T," *Journal of Magnetic Resonance Imaging*, vol. 38, no. 2, pp. 435–440, 2013.

[24] W. M. Brink and A. G. Webb, "High permittivity pads reduce specific absorption rate, improve B 1 homogeneity, and increase contrast-to-noise ratio for functional cardiac MRI at 3 T," *Magnetic Resonance in Medicine*, vol. 71, no. 4, pp. 1632–1640, 2014.

[25] W. M. Brink, J. S. van den Brink, and A. G. Webb, "The effect of high-permittivity pads on specific absorption rate in radiofrequency-shimmed dual-transmit cardiovascular magnetic resonance at 3T." *Journal of cardiovascular magnetic resonance : official journal of the Society for Cardiovascular Magnetic Resonance*, vol. 17, no. 1, p. 82, sep 2015.

[26] S. A. Winkler and B. K. Rutt, "Practical methods for improving B1+ homogeneity in 3 tesla breast imaging," *Journal of Magnetic Resonance Imaging*, vol. 41, no. 4, pp. 992–999, 2015.

[27] W. M. Brink, R. F. Remis, and A. G. Webb, "A theoretical approach based on electromagnetic scattering for analysing dielectric shimming in high-field MRI," *Magnetic Resonance in Medicine*, vol. 75, no. 5, pp. 2185–2194, 2016.

[28] M. Luo, C. Hu, Y. Zhuang, W. Chen, F. Liu, and S. X. Xin, "Numerical assessment of the reduction of specific absorption rate by adding high dielectric materials for fetus MRI at 3 T," *Biomedical Engineering / Biomedizinische Technik*, vol. 61, no. 4, pp. 455–461, 2016.

[29] C. Luo, N. Li, G. Xie, X. Zhang, X. Liu, and Y. Li, "Assessment of high dielectric material in different sizes for fetal MRI at 3T," in *Proceedings of the 26th Annual Scientific Meeting of the International Society for Magnetic Resonance in Medicine (ISMRM)*, Paris, France, 2018.

[30] J. H. F. van Gemert, W. M. Brink, A. G. Webb, and R. F. Remis, "High-Permittivity Pad Design for Dielectric Shimming in Magnetic Resonance Imaging Using Projection-Based Model Reduction and a Nonlinear Optimization Scheme," *IEEE Transactions on Medical Imaging*, vol. 37, no. 4, pp. 1035–1044, 2018.

[31] J. H. F. Van Gemert, W. Brink, A. Webb, and R. Remis, "An Efficient Methodology for the Analysis of Dielectric Shimming Materials in Magnetic Resonance Imaging," *IEEE Transactions on Medical Imaging*, vol. 36, no. 2, pp. 666–673, 2017.

SUMMARY

This dissertation describes how to design dielectric pads that can be used to increase image quality in Magnetic Resonance Imaging, and how to accelerate image reconstruction times using a preconditioner. Image quality is limited by the signal to noise ratio of a scan. This ratio is increased for higher static magnetic field strengths and therefore there is great interest in high-field MRI. The wavelength of the transmitted magnetic RF field (B_1^+ field) decreases for higher field strengths, and it becomes comparable to the dimensions of the human body. Consequently, RF interference patterns are encountered which can severely degrade image quality because of a low transmit efficiency or because of inhomogeneities in the B_1^+ field distribution. Dielectric pads can be used to improve this distribution as the pads tailor the B_1^+ field by inducing a secondary magnetic field due to its high permittivity. Typically, the pads are placed tangential to the body and in the vicinity of the region of interest. The exact location, dimensions, and constitution of the pad need to be carefully determined, however, and depend on the application and the MR configuration. Normally, parametric design studies are carried out using electromagnetic field solvers to find a suitable pad, but this is a very time consuming process which can last hours to days. Therefore, in the first part of this thesis, we present methods to efficiently model and design the dielectric pads.

To obtain a solution methodology for evaluating the pad induced B_1^+ fields, we use the fact that the dielectric pads form a low rank perturbation of a large scale computational background model. This property is exploited by the Sherman-Morrison-Woodbury formula to define a forward model that divides the computational domain into a large static domain, i.e. the heterogeneous body model and RF coils, and a relatively small dynamic pad design domain to account for the wide range of different pad realizations. As a consequence, only a small problem needs to be solved for a pad, and significant speed up factors can therefore be achieved compared with traditional field simulation approaches. For example, the fields for a typically sized dielectric pad is computed 30 times faster than using conventional methods. We validated our approach against measurements and have observed that measured and simulated field responses are in good agreement with each other.

The methods developed thus far become computationally complex for large pads as the perturbation becomes large, and hence they cannot be used efficiently in an optimization approach for pad design. Therefore, the dimension of the design problem is significantly reduced using a projection based model order reduction technique. To this end, the forward model is first parameterized in terms of the pad's characteristics, i.e. its location, dimension, and constitution. To find a projection basis, we evaluate a large number of random pads with the parameterized model, which is then used to extract recurring current patterns in the dynamic pad design domain. The dominant current patterns are used to eliminate redundant data from the forward model to obtain a reduced order model, which allows for acceleration factors of about 6000 compared to

conventional methods. Subsequently, the resulting reduced order model is incorporated in an optimization method in which a desired field in a region of interest can be set. The method is validated by designing a pad for imaging the cerebellum at 7T, a region that is difficult to scan because of its low transmit efficiency. The optimal pad is used in an MR measurement to demonstrate its effectiveness in improving the transmit efficiency and subsequently the image quality.

The reduced order model is very efficient to effectively and systematically design a pad, but it cannot be used easily by the MR community in its current form due to lack of software, resources, or expertise in this specific field. Therefore, we have created a design tool that allows for efficient and effortless pad design for any 7T neuroimaging and 3T body imaging application within minutes. The performance of the tool is demonstrated by designing a dielectric pad for cardiac imaging at 3T, and two dielectric pads for imaging the inner ear at 7T. Both designs improve the transmit efficiency as well as the homogeneity of the B_1^+ field.

In the second part of the thesis a preconditioner is designed for parallel imaging (PI) and compressed sensing (CS) reconstructions. MRI acquisition times can be strongly reduced by using PI and CS techniques by acquiring less data than prescribed by the Nyquist criterion to fully reconstruct the anatomic image; this is beneficial for patient's comfort and for minimizing the risk of patient's movement. Although acquisition times are reduced, the reconstruction times are increased significantly, especially for a large number of coils or a large number of unknowns in the image. In the reconstruction, PI uses the spatial selectivity of the receiver coils to fill in the data blanks in post-processing, whereas CS fills in the blanks by exploiting a priori information that the anatomic image is sparse in some transformation domain. These two methods can be easily combined in ℓ_1 and ℓ_2-norm based reconstruction algorithms, but solving them is much more difficult than standard reconstructions where no PI and CS is used. The equations can be solved more efficiently, however, when a preconditioner is used, such that not only acquisition times, but also reconstruction times are accelerated.

In this thesis, we construct such a preconditioner for the frequently used iterative Split Bregman framework. For every iteration, a linear system of equations is to be solved which is the most time consuming part of the reconstruction procedure. The system matrix of the linear system remains fixed throughout the iterations, however, and hence we only have to construct a preconditioner once to accelerate this part. The designed preconditioner approximates the system matrix of the linear system by a matrix that is block circulant with circulant blocks. Because of this matrix structure, we can quickly build and apply the preconditioner using fast Fourier transformations only. We have tested the performance in a conjugate gradient framework, and show that for different coil configurations, undersampling patterns, and anatomies, a five-fold acceleration can be obtained for solving the linear system part of Split Bregman.

SAMENVATTING

Dit proefschrift beschrijft hoe diëlektrische pads ontworpen kunnen worden om de beeldkwaliteit van MRI te verbeteren, evenals hoe de beeld-reconstructietijden kan worden verkort door middel van voor-conditionering. In MRI wordt de kwaliteit van de scans bepaald door de signaal ruisverhouding welke verbetert naarmate het statische magnetische veld van de MRI sterker wordt. Dit is de reden dat er veel interesse is in high-field MRI. Een nadeel van high-field MRI is dat de golflengte van het radiofrequente veld (het B_1^+ veld) verkleint. De lengte wordt vergelijkbaar met de afmetingen van het menselijk lichaam waardoor er interferentie-patronen ontstaan in het lichaam. Dit zorgt ervoor dat het B_1^+ veld op sommige plekken extra sterk zal worden en op andere plekken juist extra zwak. Deze inhomogeniteiten en zwakke velden verslechteren de beeldkwaliteit. Een praktische oplossing om deze velden te verbeteren is het gebruik van diëlektrische pads. Deze pads hebben een erg hoge permittiviteit waardoor ze een sterk secundair magnetisch veld opwekken. Vaak worden deze op het lichaam geplaatst vlakbij het interessegebied zodat ze het magnetische veld plaatselijk kunnen sturen. Om het gewenste effect te bereiken dient de pad zorgvuldig ontworpen te worden. De afmetingen, locatie en materiaaleigenschappen van de pad hangen sterk af van de toepassing en de MRI-configuratie. Normaal gesproken worden deze eigenschappen bepaald aan de hand van parametrische ontwerpstudies in elektromagnetische veldsimulatie programma's, maar dit is erg tijdrovend en kan uren tot dagen duren. In het eerste gedeelte van dit proefschrift wordt een alternatieve methode beschreven welke een stuk sneller is.

Om tot een efficiënt rekenmodel te komen hebben we de eigenschap gebruikt dat de pads altijd een kleine verstoring veroorzaken op een grootschalig achtergrondmodel. Dit achtergrondmodel bevat het menselijk lichaam en de zend-spoelen en is statisch, wat betekent dat deze configuratie hetzelfde blijft ongeacht de locatie en grootte van een geplaatste pad. Deze eigenschap kan benut worden via de Sherman-Morrison-Woodbury formule, welke ervoor zorgt dat ons rekenmodel opgedeeld kan worden in een groot statisch domein en een klein pad-ontwerp domein. Om het B_1^+ veld te berekenen voor een willekeurige pad hoeft er nu enkel een klein probleem opgelost te worden. Dit leidt tot rekentijden die tot 30 keer sneller zijn dan de conventionele methodes.

De methoden die tot dusver ontwikkeld zijn worden rekenkundig complex voor grote pads omdat de verstoring groot wordt. Dit zorgt ervoor dat ze niet efficiënt gebruikt kunnen worden voor optimalisatiedoeleinden bij het ontwerp van de pads. Om die reden wordt de complexiteit verkleind door gebruik te maken van een projectie-gebaseerd gereduceerd model. Om hier gebruik van te kunnen maken wordt het model eerst geparametriseerd in termen van de locatie, afmetingen en materiaaleigenschappen van de pads. Vervolgens worden de elektromagnetisch velden berekend voor een groot aantal pads met ieder willekeurige eigenschappen. Vanuit de verkregen resultaten worden de terugkerende stroompatronen gehaald om op deze manier redundante en overbodige

informatie uit ons oorspronkelijke model te verwijderen. Dit leidt tot een gereduceerd model dat 6000 keer sneller opgelost kan worden dan conventionele methoden. Het model wordt vervolgens gecombineerd met een optimalisatietechniek waarmee het mogelijk wordt de juiste pad-eigenschappen te vinden voor een willekeurig interessegebied. Met deze techniek is er een pad ontworpen om het cerebellum te scannen bij een veldsterkte van 7 Tesla, wat een erg lastig gebied is door het zwakke magnetische veld. De ontworpen pad verbetert het B_1^+ veld en daardoor ook de kwaliteit van de cerebellum scan.

Het gereduceerde model is erg effectief om pads te ontwerpen, maar het kan in de huidige vorm niet gemakkelijk gebruikt worden door de MRI-gemeenschap wegens gebrek aan software, middelen of kennis in dit specifieke gebied. Vandaar dat we een ontwerptool hebben gemaakt die het mogelijk maakt om binnen een paar minuten de pads moeiteloos te ontwerpen voor iedere 7T brein-applicatie en 3T lichaam-applicatie. De doeltreffendheid in het verbeteren van het B_1^+ veld wordt getoond door een pad te ontwerpen voor de hart-scan bij 3T en het binnenoor bij 7T.

In het tweede deel van het proefschrift is een voor-conditioneringsmatrix gemaakt om de reconstructies te versnellen van metingen die gebruik maken van de technieken parallelle beeldverwerking (Engels: Parallel Imaging, PI) en gecomprimeerd meten (Engels: Compressed Sensing, CS). De meettijden van MRI kunnen sterk gereduceerd worden door deze PI en CS technieken. Dit komt ten goede aan het comfort van de patiënt en verkleint tevens het risico van beweging tijdens een scan. De technieken meten minder data dan voorgeschreven wordt door het Nyquist criterium om een volledige reconstructie uit te kunnen voeren. De hiaten in de data kunnen namelijk achteraf opgevuld worden door de extra informatie die beschikbaar is uit PI in de vorm van de ruimtelijke sensitiviteit van meerdere meetspoelen, en door CS welke de voorkennis gebruikt dat de anatomische beelden in een bepaald transformatie domein erg weinig informatie bevatten. De twee methoden kunnen makkelijk gecombineerd worden in zogenaamde ℓ_1- en ℓ_2-norm gebaseerde reconstructie algoritmes, maar het oplossen van deze problemen is veel ingewikkelder dan de standaard reconstructies zonder de PI- en CS-technieken. Hoewel de meettijden dus verkort zijn, worden de reconstructietijden juist groter, vooral wanneer een groot aantal meetspoelen gebruikt wordt of wanneer het aantal onbekende pixels in een plaatje groot is. De nieuwe reconstructieproblemen kunnen echter wel efficiënter en sneller opgelost worden wanneer gebruik wordt gemaakt van een voor-conditioneringsmatrix, waardoor zowel de meting als de reconstructie snel wordt.

In dit proefschrift is een voor-conditioneringsmatrix ontworpen voor het veelgebruikte iteratieve Split Bregman algoritme. Binnen iedere iteratie in dit algoritme wordt een lineair systeem van vergelijkingen opgelost welke het meest tijdrovende gedeelte van het algoritme is. De systeemmatrix van het lineaire systeem blijft tijdens het itereren constant en daarom hoeven we maar een enkele keer een voor-conditioneringsmatrix te ontwerpen om dit gedeelte te versnellen. Het ontwerp benadert de systeemmatrix door een matrix die blok circulant is met circulante blokken. Een matrix met deze structuur kan met behulp van Fourier transformaties snel gebouwd en toegepast worden. We demonstreren de effectiviteit in een geconjugeerd gradiënt raamwerk en demonstreren dat voor verschillende interessegebieden en meetspoel-configuraties een vijfvoud versnelling te behalen is in het oplossen van het lineaire gedeelte van Split Bregman.

LIST OF PUBLICATIONS

LIST PEER REVIEWED PUBLICATIONS

Note: Shared first-author work is indicated by the symbol †.

[A] **J.H.F. van Gemert**, W.M. Brink, A.G. Webb, and R.F. Remis, "An Efficient Methodology for the Analysis of Dielectric Shimming Materials in Magnetic Resonance Imaging," *IEEE Transactions in Medical Imaging*, vol. 36, no. 2, pp. 666 – 673, 2017.

[B] **J.H.F. van Gemert**, W.M. Brink, A.G. Webb, and R.F. Remis, "High-Permittivity Pad Design for Dielectric Shimming in Magnetic Resonance Imaging using Projection Based Model Reduction and a Nonlinear Optimization Scheme," *IEEE Transactions in Medical Imaging*, vol. 37, no. 4, pp. 1035 – 1044, 2018.

[C] **J.H.F. van Gemert**, W.M. Brink, A.G. Webb, and R.F. Remis, "High-Permittivity Pad Design Tool for 7T Neuroimaging and 3T Body Imaging," *Magnetic Resonance in Medicine*, DOI: 10.1002/mrm.27629, Nov. 2018.

[D] **J.H.F. van Gemert**, W.M. Brink, R.F. Remis, and A.G. Webb "A Simulation Study on the Effect of Optimized High Permittivity Materials on Fetal Imaging at 3T," under review in *Magnetic Resonance in Medicine* , December 2018.

[E] K. Koolstra†, **J.H.F. van Gemert**†, P. Börnert, A.G. Webb, and R.F. Remis, "Accelerating Compressed Sensing in Parallel Imaging Reconstructions Using an Efficient Circulant Preconditioner for Cartesian Trajectories," *Magnetic Resonance in Medicine*, vol. 81, no. 1, pp. 670 – 685, 2019.

LIST OF CONFERENCE PROCEEDINGS AND TALKS

Note: Shared first-author work is indicated by the symbol †.

[a] **J.H.F. van Gemert**, W.M. Brink, A.G. Webb, and R.F. Remis, "A Fast and Easy-to-Use Tool for designing High-Permittivity Pads for 3T Body and 7T Neuroimaging Applications," submitted to *the 27th Annual Scientific Meeting of the International Society for Magnetic Resonance in Medicine (ISMRM)*, Montreal, QC, Canada, 2019.

[b] **J.H.F. van Gemert**, W.M. Brink, R.F. Remis, and A.G. Webb "Optimized High-Permittivity Pads Can Reduce SAR and Increase Transmit Field Homogeneity in Fetal Imaging at 3T," submitted to *the 27th Annual Scientific Meeting of the International Society for Magnetic Resonance in Medicine (ISMRM)*, Montreal, QC, Canada, 2019.

[c] W.M. Brink, **J.H.F. van Gemert**, P. Börnert, R.F. Remis, and A.G. Webb "Massively Accelerated Simulations of High-Permittivity Materials in Multi-Channel Receive Arrays," submitted to *the 27th Annual Scientific Meeting of the International Society for Magnetic Resonance in Medicine (ISMRM)*, Montreal, QC, Canada, 2019.

[d] W.M. Brink, **J.H.F. van Gemert**, R.F. Remis, and A.G. Webb "Accelerated SAR Computations by Exploiting Sparsity in the Anatomical Domain," submitted to *the 27th Annual Scientific Meeting of the International Society for Magnetic Resonance in Medicine (ISMRM)*, Montreal, QC, Canada, 2019.

[e] P.R.S. Stijnman, J.P. Tokaya, **J.H.F. van Gemert**, P.R. Luijten, J.P.W. Pluim, W.M. Brink, R.F. Remis, C.A.T. van den Berg, and A.J.E. Raaijmakers "Calculation of the scattered RF field around implants within seconds using a low-rank inverse updating method," submitted to *the 27th Annual Scientific Meeting of the International Society for Magnetic Resonance in Medicine (ISMRM)*, Montreal, QC, Canada, 2019.

[f] **J.H.F. van Gemert**, W.M. Brink, A.G. Webb, and R.F. Remis, "A Fast and Easy-to-Use Tool for designing High-Permittivity Pads for 3T Body and 7T Neuroimaging Applications," in *Proceedings of the 11th Annual Scientific Meeting of the International Society for Magnetic Resonance in Medicine (ISMRM) - Benelux Chapter*, Leiden, The Netherlands, 2019.

[g] **J.H.F. van Gemert**, W.M. Brink, R.F. Remis, and A.G. Webb "Optimized High-Permittivity Pads Can Reduce SAR and Increase Transmit Field Homogeneity in Fetal Imaging at 3T," in *Proceedings of the 11th Annual Scientific Meeting of the International Society for Magnetic Resonance in Medicine (ISMRM) - Benelux Chapter*, Leiden, The Netherlands, 2019.

[h] W.M. Brink, **J.H.F. van Gemert**, P. Börnert, R.F. Remis, and A.G. Webb "Massively Accelerated Simulations of High-Permittivity Materials in Multi-Channel Receive Arrays," in *Proceedings of the 11th Annual Scientific Meeting of the International Society for Magnetic Resonance in Medicine (ISMRM) - Benelux Chapter*, Leiden, The Netherlands, 2019.

[i] W.M. Brink, **J.H.F. van Gemert**, R.F. Remis, and A.G. Webb "Accelerated SAR Computations by Exploiting Sparsity in the Anatomical Domain," in *Proceedings of the 11th Annual Scientific Meeting of the International Society for Magnetic Resonance in Medicine (ISMRM) - Benelux Chapter*, Leiden, The Netherlands, 2019.

[j] P.R.S. Stijnman, J.P. Tokaya, **J.H.F. van Gemert**, P.R. Luijten, J.P.W. Pluim, W.M. Brink, R.F. Remis, C.A.T. van den Berg, and A.J.E. Raaijmakers "Calculation of the scattered RF field around implants within seconds using a low-rank inverse updating method," in *Proceedings of the 11th Annual Scientific Meeting of the International Society for Magnetic Resonance in Medicine (ISMRM) - Benelux Chapter*, Leiden, The Netherlands, 2019.

[k] **J.H.F. van Gemert**†, K. Koolstra†, P. Börnert, A.G. Webb, and R.F. Remis, "Accelerating Compressed Sensing in Cartesian Parallel Imaging Reconstructions using an Efficient and Effective Circulant Preconditioner," in *Proceedings of the 26th Annual Scientific Meeting of the International Society for Magnetic Resonance in Medicine (ISMRM)*, Paris, France, 2018.

[l] **J.H.F. van Gemert**†, K. Koolstra†, P. Börnert, A.G. Webb, and R.F. Remis, "Accelerating Compressed Sensing in Cartesian Parallel Imaging Reconstructions using an Efficient and Effective Circulant Preconditioner," in *Proceedings of the 10th Annual Scientific Meeting of the International Society for Magnetic Resonance in Medicine (ISMRM) - Benelux Chapter*, Antwerp, Belgium, 2018.

[m] W.M. Brink, J. Paska, J. Dai, **J.H.F. van Gemert**, G. Chen, G.C. Wiggins, R.F. Remis, C.M. Collins, and A.G. Webb "Dielectric enhanced dipoles for MRI Approaching the ideal current pattern," in *Proceedings of the International Conference on Electromagnetics in Advanced Applications (ICEAA)*, Verona, Italy, 2017.

[n] **J.H.F. van Gemert**, W.M. Brink, A.G. Webb, and R.F. Remis, "Designing High-Permittivity Pads for Dielectric Shimming in MRI using Model Order Reduction and Gauss-Newton Optimization," in *Proceedings of the International Conference on Electromagnetics in Advanced Applications (ICEAA)*, Verona, Italy, 2017, *invited talk*.

[o] W.M. Brink, J. Paska, J. Dai, **J.H.F. van Gemert**, G. Chen, G.C. Wiggins, R.F. Remis, C.M. Collins, and A.G. Webb "Efficient Analysis of Dielectric Materials in Coupled RF Coil Configurations," in *Proceedings of the 25th Annual Scientific Meeting of the International Society for Magnetic Resonance in Medicine (ISMRM)*, Honolulu, Hawaii, USA, 2017.

[p] **J.H.F. van Gemert**, W.M. Brink, A.G. Webb, and R.F. Remis, "Fast 3D Design of High-Permittivity Pads for Dielectric Shimming using Model Order Reduction and Nonlinear Optimization," in *Proceedings of the 25th Annual Scientific Meeting of the International Society for Magnetic Resonance in Medicine (ISMRM)*, Honolulu, Hawaii, USA, 2017.

[q] **J.H.F. van Gemert** and K. Koolstra, "Modeling and Designing High Permittivity Pads for MRI," *SIAM Student Chapter*, Delft, The Netherlands, 2017, *invited talk*.

[r] W.M. Brink, J. Paska, J. Dai, **J.H.F. van Gemert**, G. Chen, G. Wiggins, R.F. Remis, C. Collins, and A.G. Webb "Efficient Analysis of Dielectric Materials in Coupled RF Coil Configurations," *Proceedings of the 9th Annual Scientific Meeting of the International Society for Magnetic Resonance in Medicine (ISMRM) - Benelux Chapter*, Tilburg, The Netherlands, 2017.

[s] **J.H.F. van Gemert**, W.M. Brink, A.G. Webb, and R.F. Remis, "Fast 3D Design of High-Permittivity Pads for Dielectric Shimming using Model Order Reduction and Nonlinear Optimization," *Proceedings of the 9th Annual Scientific Meeting of the International Society for Magnetic Resonance in Medicine (ISMRM) - Benelux Chapter*, Tilburg, The Netherlands, 2017.

[t] W.M. Brink, **J.H.F. van Gemert**, R.F. Remis, and A.G. Webb, "Inverse design of dielectric pads based on contrast source inversion," *Proceedings of the 24th Annual Scientific Meeting of the International Society for Magnetic Resonance in Medicine (ISMRM)*, Singapore, Singapore, 2016.

[u] **J.H.F. van Gemert**, W.M. Brink, A.G. Webb, and R.F. Remis, "An efficient 3D RF simulation tool for dielectric shimming optimization," *Proceedings of the 24th Annual Scientific Meeting of the International Society for Magnetic Resonance in Medicine (ISMRM)*, Singapore, Singapore, 2016.

[v] W.M. Brink, **J.H.F. van Gemert**, R.F. Remis, and A.G. Webb, "Automated Design Approach for Dielectric Shimming in High Field MRI," *ISMRM Workshop on Ultra High Field MRI*, Heidelberg, Germany, 2015.

[w] W.M. Brink, **J.H.F. van Gemert**, R.F. Remis, and A.G. Webb, "Inverse design of dielectric pads based on contrast source inversion," *Proceedings of the 8th Annual Scientific Meeting of the International Society for Magnetic Resonance in Medicine (ISMRM) - Benelux Chapter*, Eindhoven, The Netherlands, 2016.

[x] **J.H.F. van Gemert**, W.M. Brink, A.G. Webb, and R.F. Remis, "An efficient 3D RF simulation tool for dielectric shimming optimization',' *Proceedings of the 8th Annual Scientific Meeting of the International Society for Magnetic Resonance in Medicine (ISMRM) - Benelux Chapter*, Eindhoven, The Netherlands, 2016.

PROPOSITIONS

1. Using the solution and optimization methods proposed in this thesis, optimal dielectric pads can easily be designed within minutes by any MR researcher (this proposition pertains to this dissertation).

2. The reduced order library that is created using birdcage excited snapshots can effectively be used for field computations in a configuration that is not excited by a birdcage coil (this proposition pertains to this dissertation).

3. Potential discomfort caused by a dielectric pad is only a minor side effect compared with the increase in image quality of an MR scan.

4. The number of regularization parameters in MR reconstruction should be kept to a minimum (this proposition pertains to this dissertation).

5. For Cartesian undersampling patterns, the data fidelity term can be well approximated by a block circulant matrix with circulant blocks (this proposition pertains to this dissertation).

6. Deep learning in MR reconstruction for undersampled data should only be adopted by the clinic once it is combined and supported by physical principles.

7. One cannot say “I have nothing to hide” as the believe of doing nothing wrong is subjective and dynamic over time.

8. The fight against fake news paves the way to censure.

9. MRI and CT scans should only be performed when it is recommended by a clinical specialist.

10. Swimming enriches and relaxes the mind and should be learned at any elementary school in the Netherlands especially in these mobile phone induced stressful times.

ACKNOWLEDGMENTS

The last four years have been a wonderful journey where I have gotten to know many great people. Without them, I wouldn't have succeeded in getting my PhD. I look back at a great time of which I have enjoyed (almost) every moment.

Gelukkig zijn we na mijn afstuderen in contact gebleven, Rob. Jij hebt mij de mogelijkheid gegeven om te gaan promoveren en mij tevens het zetje gegeven dat ik destijds nodig had. De afgelopen vier jaar waren erg leuk en ik heb heel veel van je geleerd. We hebben vele gesprekken gehad, welke ik altijd gewaardeerd heb omdat het zelden enkel over het onderzoek gegaan is. We hebben veel kunnen sparren en hebben zo samen iets moois neer kunnen zetten. Ik word altijd erg vrolijk van je vriendelijkheid en je enthousiasme over de ideeën en de resultaten die we onderweg opgedaan hebben. We hebben natuurlijk al veel samengewerkt en redelijk wat biertjes gedronken en ik hoop dat we dat in de toekomst kunnen blijven doorzetten. Ontzettend bedankt voor alles!

Andrew, thank you for the past four years. I remember my first visit to the Gorter Center, the moment I realized how great it would be to join such a nice research group led by you. It amazes me that, in spite of your busy schedule and the large group, you always have the time for a chat which often allows me to put my thoughts in order. I admire your broad knowledge, your approachability, your encouragement to pursue one's own ideas, and your eagerness to stay active in doing research yourself.

I would also like to express my gratitude to my PhD committee for their time and interest to join my defense ceremony. When I started my PhD I did not expect to have such nice and highly respected members. Alexander, thank you for the discussions and the welcome remarks which have helped me throughout the process. Peter, thank you for your enthusiasm and help, I have always liked your sense of humor.

Heel veel dank gaat uit naar al mijn collega's van het LUMC, te veel mensen om op te noemen. Het is een heerlijke werkomgeving geweest met veel leuke activiteiten waar collega's vrienden zijn geworden. Veel dank aan al mijn kantoorgenoten, de drukte is altijd goed bevallen. Luc, je bent er nu klaar voor, ik draag graag het 'nestor-stokje' aan jou over. Altijd vrolijke Merlijn en Lydiane, bedankt voor alle vrolijkheid. Melissa en Mathijs, wat fijn en leuk dat jullie zoveel borrels georganiseerd hebben, hierdoor ben ik mij snel thuis gaan voelen. Sanneke, Sophie en Annemarieke, bedankt voor de leuke momenten en fijn dat jullie er van begin tot eind zijn geweest! Marjolein, enorm bedankt voor alle hilarische momenten en de vele gesprekken, praten en werken hebben we (soms) goed weten te combineren. Paul en Leon, bedankt voor de leuke trip naar Hawaii en alle pre and after Hawaii borrels!

Many thanks to the CAS group. Special thanks to my first colleagues Jorge and Raj for the good times in our office. My German friends Patrick and Jorn, we managed to claim an EM office in the building, I liked our discussions and EM outings! Andreas, Thom, Shahrzad, and Elvin, we started together and we leave together, thanks for the shared adventure. Alle-Jan, thank you for providing a pleasant work environment in the group.

Finally, I would like to thank Minaksie, Minke, and Irma for arranging all the nice events and the secretarial business.

Wyger, ik heb onze samenwerking erg leuk gevonden. We hebben altijd goed met elkaar kunnen praten, lachen en brainstormen om zo het onderste uit de kan te halen. Ik heb veel van je geleerd over de pads en MRI, en ik vind het jammer dat het hier eindigt. Succes met je Veni, ik ben er van overtuigd dat je iets moois gaat neerzetten. Bedankt, en wie weet wat de toekomst brengt!

Paranimf Kirsten, het was mooi dat we buiten ons eigen project samen hebben kunnen werken aan een totaal ander onderwerp. De samenwerking was altijd erg plezierig en we hebben veel van elkaar kunnen leren. Het is altijd een leuke afwisseling geweest tussen werk, lachen, en tetris. Bedankt dat je naast me wilt staan tijdens mijn verdediging! Veel succes met je laatste jaar en we werken sowieso weer samen bij je volgende baan!

Ook veel dank gaat uit naar mijn vrienden die altijd voor goede afleiding hebben gezorgd. Specifiek wil ik Hens en Jurjen bedanken voor hun aanmoediging en de mooie vakanties. Ondanks dat we al 9 jaar niet meer samen wonen, zien we elkaar gelukkig nog steeds zeer regelmatig. Jurjen, de creativiteit die ik van jou opgestoken heb tijdens onze vele hobbyprojecten zijn goed van pas gekomen. Hens, ik ben heel blij dat je naast me staat als paranimf, ik had niemand anders kunnen wensen! Natuurlijk ook veel dank aan jou en Janneke voor de tijd die jullie in de cover gestoken hebben.

Lieve familie en lieve aanhang, veel dank voor alle interesse afgelopen jaren en het toejuichen van ieder succes en het medeleven voor iedere tegenvaller. De weekjes weg zijn altijd erg goed bevallen en hebben voor veel rust in mijn hoofd gezorgd. Extra veel dank aan mijn moeder, omdat je zo hard hebt gevochten om mij op het hoger onderwijs te krijgen, zonder jou had ik dit punt niet bereikt. Ook dank aan mijn vader, dankzij jou is de interesse in elektrotechniek ontstaan. Mijn lieve schoonfamilie wil ik bedanken voor hun aanmoediging, gezelligheid en oprechte interesse!

Lieve Bonny, ik kan jou natuurlijk niet vergeten! Je bent er de afgelopen jaren veel voor mij geweest en je hebt voor veel afleiding gezorgd. Als ik me zorgen maakte dan lukte het jou vaak om die weer weg te nemen. Wat ik erg leuk vind, en waar ik ook versteld van sta, is dat je tot in detail wilt weten wat ik allemaal aan het doen ben en hoe alles werkt, soms tot vervelends aan toe. Dit zorgde er ook voor dat je vaak kon meedenken en met erg leuke oplossingen bent gekomen. Dankjewel voor al je interesse en liefde!

Jeroen
Delft, December, 2018

Curriculum Vitae

On Tuesday the 14th of January 1986, on a heavily clouded and cold day, Jeroen Hendrikus Fransiscus van Gemert was born in Nijmegen, The Netherlands. In 2011 and 2013 he received his Bachelor's degree and Master's degree (*cum laude*) in Electrical Engineering from the Delft University of Technology. During his MSc. research Jeroen worked with Rob Remis and the company Lismar Engineering B.V. on crack detection for plate rolls used for pressing steel, which led to the master thesis entitled: "Imaging of Cracks and Weak Spots in Steel and Aluminium Plate Rolls." After graduation he started to work as a software engineer for the company Imtech Traffic & Infra where he worked on the ventilation system of the Maastricht tunnel Avenue2 and the power management systems of the trams in The Hague and Amsterdam. After a year he returned to Delft for his STW supported PhD project at the Circuits & Systems group of the EEMCS faculty, headed by Prof. Alle-Jan van der Veen. In 2015, he started his PhD research and closely collaborated with the C.J. Gorter Center for High-field MRI of the Leiden University Medical Center, headed by Prof. Andrew Webb, and the Microwave Sensing, Signals and Systems department of the TU Delft, headed by Prof. Alexander Yarovoy. Jeroen likes to spend his spare time in the swimming pool or in a lake, is fond of board games and "klaverjassen," and is trying to strum the guitar.